Near-Surface Structure and Velocities of the Northeastern Santa Cruz Mountains and the Western Santa Clara Valley, California, From Seismic Imaging

By R.D. Catchings[1], G. Gandhok[1], M.R. Goldman[1], and Clare Steedman[1]

Open-File Report 2007-1039

2007

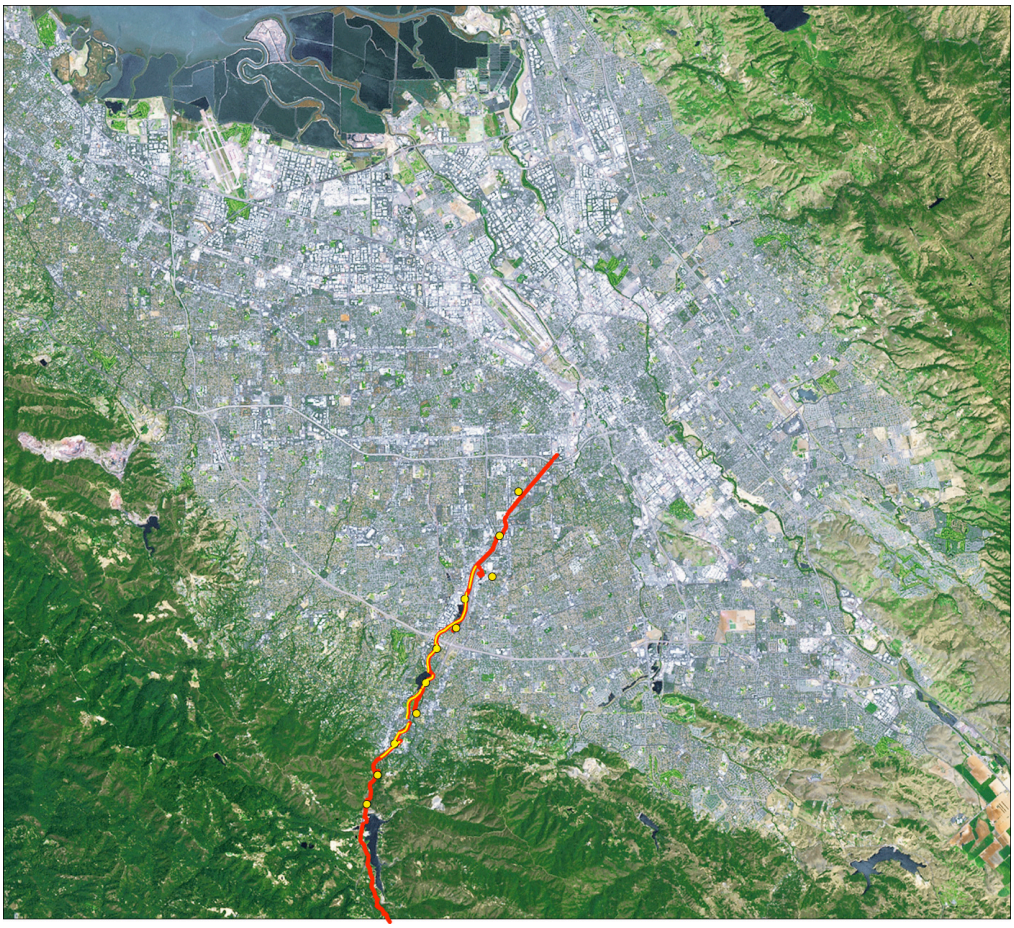

U.S. DEPARTMENT OF THE INTERIOR
U.S. GEOLOGICAL SURVEY

[1] Menlo Park, Calif.

Contents

Introduction

The Santa Clara Valley (SCV) is located in the southern San Francisco Bay area of California and is bounded by the Santa Cruz Mountains to the southwest, the Diablo Ranges to the northeast, and the San Francisco Bay to the north (Fig. 1). The SCV, which includes the City of San Jose, numerous smaller cities, and much of the high-technology manufacturing and research area commonly referred to as the Silicon Valley, has a population in excess of 1.7 million people (2000 U. S. Census; http://quickfacts.census.gov/qfd/states/06/06085.html). The SCV is situated between major active faults of the San Andreas Fault system, including the San Andreas Fault to the southwest and the Hayward and Calaveras faults to the northeast, and other faults inferred to lie beneath the alluvium of the SCV (CWDR, 1967; Bortugno et al., 1991). The importance of the SCV as a major industrial center, its large population, and its proximity to major earthquake faults are important considerations with respect to earthquake hazards and water-resource management. The fault-bounded alluvial aquifer system beneath the valley is the source of about one-third of the water supply for the metropolitan area (Hanson et al., 2004).

To better address the earthquake hazards of the SCV, the U.S. Geological Survey (USGS) has undertaken a program to evaluate potential seismic sources, the effects of strong ground shaking, and stratigraphy associated with the regional aquifer system. As part of that program and to better understand water resources of the valley, the USGS and the Santa Clara Valley Water District (SCVWD) began joint studies to characterize the faults, stratigraphy, and structures beneath the SCV in the year 2000. Such features are important to both agencies because they directly influence the availability and management of groundwater resources in the valley, and they affect the severity and distribution of strong shaking from local and regional earthquakes sources that may affect reservoirs, pipelines, and flood-protection facilities maintained by SCVWD. As one component of these joint studies, the USGS acquired an approximately 10-km-long, high-resolution, combined seismic reflection/refraction transect from the Santa Cruz Mountains to the central SCV in December 2000 (Figs. 1 and 2a,b). The overall seismic investigation of the western Santa Clara Valley also included an ~18-km-long, lower-resolution (~50-m sensor) seismic imaging survey from the central Santa Cruz Mountains to the central part of the valley (Fig. 1). Collectively, we refer to these seismic investigations as the 2000 western Santa Clara Seismic Investigations (SCSI). Results of the high-resolution investigation, referred to as SCSI-HR, are presented in this report, and Catchings et al. (2006) present results of the low-resolution investigation (SCSI-LR) in a separate report. In this report, we present data acquisition parameters, unprocessed and processed seismic data, and interpretations of the SCSI-HR seismic transect.

Local Geology, Tectonics, and Hydrogeology

The SCV is part of the topographic depression between the Santa Cruz Mountains and the Diablo Ranges that forms the San Francisco Bay (Fig. 1). Surficial and near-surface sediments within the SCV consist largely of Pleistocene to Holocene clastic deposits (clay, silt, sand, and gravel) from the adjacent mountain ranges and marine sediments (CDWR, 1967; Wagner, 1990; Helley et al., 1994; Wentworth et al., 1997; McLaughlin et al., 2001; Stanley et al., 2002). The composition of basement rocks beneath the SCV is not well known but is assumed to be similar to those in the adjacent mountain ranges (Fig. 3a,b) and to those sampled at selected deep monitoring-well sites (Newhouse et al., 2004). Rocks within the mountains include the Jurassic to Cretaceous Franciscan Complex (marine sediments, largely melanges, including serpentine, volcanic, and metamorphic rocks), the Coast Ranges Ophiolite (ultramafic to intermediate igneous rocks), and the Great Valley Sequence of sedimentary rocks (McLaughlin et al., 2001). At least one recently drilled borehole (Willow well) near the center

of the valley near Los Gatos Creek (Fig. 3a) encountered serpentinite at 250 m depth (Newhouse et al., 2004), which is likely part of the Coast Ranges Ophiolite. Another recently drilled well at the McGlincey site (MGCY) farther west (Fig. 3a) encountered Tertiary deposits, which are likely part of the Monterey Formation (Newhouse et al., 2004).

Within the adjacent mountain ranges, rocks are highly faulted and folded (Fig. 3a) due to tectonism, much of which is associated with the San Andreas fault system (CDWR, 1967; McLaughlin et al., 2001). Faulted and folded rocks may also underlie the near-surface Quaternary deposits within the SCV, as evidenced by strike-slip and reverse faults and folded strata that have been mapped on exposed ridges (for example, the Santa Teresa Hills and Sierra Azul) within the valley (McLaughlin et al., 2001). Some of the buried faults are active, as shown by seismic events recorded beneath the valley (ANSS Catalog, 2003-anss@quake.geo.berkeley.edu), but previous studies have not conclusively proven that these faults extend to the near surface beneath the valley. Differential movement on such faults may have produced a series of basement highs and lows, deep basins near the valley margins (i.e., Cupertino and Evergreen basins), and a relative basement high near the center of the valley (CWDR, 1967; Stanley et al., 2002; Catchings et al., 2006).

Fault and stratigraphic controls on ground-water flow and recharge require better delineation for improved management of the ground-water resources. Because the alluvial deposits of the regional aquifer system are layered, better delineation of stratigraphic layering can improve our understanding of land subsidence (Poland, 1988; Hanson et al., 2004; 2005) and ground water flow to multi-aquifer wells (Hanson et al., 2003). Fresh-water-bearing deposits that form the ground-water aquifer systems within the Santa Clara Valley are composed of Quaternary alluvial deposits and include associated Pliocene and Pleistocene deposits (Santa Clara Formation; SCFm) and the overlying Pleistocene-to-Holocene unconsolidated alluvial and bay deposits (CWDR, 1967). Near-surface consolidated and low-permeability sedimentary rocks and Franciscan Complex rocks are regarded as non-water bearing and not a part of the hydrogeology of the valley. Lateral variations in the thickness of the SCFm are not well known, but the SCFm deposits have been encountered in boreholes at depths ranging from about 30 m to several hundred meters within the valley. Where exposed in the adjacent Santa Cruz Mountains, the SCFm is mildly folded and faulted and consists of poorly sorted conglomerate, sandstone, siltstone, and clay that is as much as 600 m thick in outcrop (Dibblee, 1966; McLaughlin et al., 2001). Where it crops out on the southwest flanks of the valley, the SCFm dips 10 to 30 degrees northeastward (CDWR, 1967) but is assumed to be missing from beneath much of the alluvial deposits within the valley. The unconsolidated alluvial and bay deposits (clay, silt, sand, and gravel) that overlie bedrock and Tertiary deposits contain the most productive aquifers of the ground-water reservoir (Poland, 1971, 1988; Hanson et al., 2004). Minimum depths to the water table are highly variable within the valley, but generally range from about 10 to 40 m below the ground surface (CWDR, 1967; Hanson et al., 2002).

SCSI Data Acquisition

Data Acquisition

The SCSI seismic investigation consisted of two separate combined seismic refraction and reflection surveys, a relatively high-resolution (5-m shot and geophone spacing) combined reflection and refraction survey and a relatively low-resolution (50-m seismograph and 1-km shot spacing) combined reflection and refraction survey (see cover). Geographically, both surveys were mostly coincident, varying only in a few locations along the transect. The low-resolution survey (SCSI-LR) was approximately18 km long and extended along Los Gatos

Creek from the San Andreas Fault to downtown San Jose (Fig. 1). The high-resolution survey (SCSI-HR) was approximately 10 km long, extending between shot points 1 and 10 of the lower-resolution survey (Figs. 2a,b). Each survey was acquired in a manner that yields both seismic refraction and seismic reflection images of the subsurface to varying depths. The combined reflection and refraction data are needed to more clearly image complex structures, such as steeply dipping or faulted structures (Hole et al., 2001; Catchings et al., in press). This report describes data acquisition, processing, analysis, and preliminary interpretations for the high-resolution (SCSI-HR) survey.

The SCSI-HR transect was acquired along Los Gatos Creek between Lexington Dam and the City of Campbell (Figs. 1 and 2a,b). The overall trend of the transect was approximately N 60°E, but to aid in data acquisition, processing, and interpretation, we acquired and processed the transect as a series of 14 approximately near-linear segments (referred to as profiles SCSI-1 through SCSI-14), with each profile trending at varying azimuths along Los Gatos Creek. For discussion purposes in this report, we differentiate between the SCSI profiles, which are individual near-linear segments, and the SCSI-HR transect, which is the composite of the linear profiles. We acquired each segment using a shoot-through acquisition technique, whereby the recording sensors remained stationary as shots were fired through most or all of the recording arrays. This method allows the determination of details of the subsurface velocity structure, which are needed to infer lithology and to more clearly develop reflection images in areas with laterally varying velocities, such as fault zones (Catchings et al., in press). For profiles longer than 600 m, we typically fired shots through one-half to three-quarters of the active array before the southwestern 60 channels were moved to the northeastern end of the active array. Acquisition parameters for each segment of the transect are shown in Table 1.

Approximately 3 s of data were recorded on one or two Geometrics StrataviewTM RX 60 seismographs, each with 60 active channels. Seismic sources and sensors (geophones) were co-located (1-m separation) and spaced at 5-m increments along each segment of the profile. We used 400-grain Betsy- SeisgunTM blanks in 0.3-m-deep holes to generate the seismic sources. Sensors consisted of 40-Hz, single-element, Mark Products L-40A TM vertical geophones, spaced at 5-m increments along the profile. Shot timing was determined electronically at the seismic source when a hammer, used to trigger the seisgun, electrically closed contact with the BETSY SeisgunTM, sending an electrical signal to the seismograph. Data were recorded without acquisition filters at a sampling rate of 0.5 ms and were stored on the hard disk of the seismograph during field acquisition. We chose not to use acquisition filters in the field because filtering could be accomplished in the laboratory and because we desired to record the entire seismic wavefield, some of which is useful for other purposes (for example, surface waves). After recording each day, the data were retrieved from the hard disk of the seismographs and downloaded to 4-mm DAT tapes in SEG 2 format for long-term storage.

Table 1A. Acquisition parameters for profiles SCSI-1 through SCSI-14. Distances are relative to the first geophone or shot point of each profile.

Profile #	Orientation	Geo. Array Length (m)	Shot Array Length (m)	# Shots	# CDPs	Max. Fold
SCSI-1	S-N	59.75	49.65	10	23	10
SCSI-2	S-N	495.54	495.23	107	224	107
SCSI-3	S-N	559.37	558.93	111	232	111
SCSI-4	SW-NE	237.48	237.07	47	97	47
SCSI-5	SW-NE	818.01	818.27	138	331	83
SCSI-6	SW-NE	237.76	237.80	46	97	46
SCSI-7	SW-NE	543.29	543.54	111	235	111
SCSI-8	SW-NE	338.37	338.13	61	133	61
SCSI-9	SW-NE	1543.80	1533.6	245	661	67
SCSI-10	SW-NE	301.92	298.79	63	134	63
SCSI-11	SW-NE	567.20	567.07	108	235	108
SCSI-12	SW-NE	447.18	442.98	96	192	96
SCSI-13	SW-NE	2042.56	2022.76	427	899	115
SCSI-14	SW-NE	794.11	794.03	158	376	115

Table 1B. Additional acquisition geometry along profiles SCSI-1 through SCSI-14.

Profile #	Geo. Elev. Change	Shot Elev. Change (m)	Geo. Non-Linearity (m /%)	Shot Non-Linearity (m/%)	Skipped Shots
SCSI-1	0.8	0.8	0.7	0.7	3
SCSI-2	11	11	75/15%	76/15	5
SCSI-3	10	10	49/9%	42/7%	4
SCSI-4	1.6	16.6	17/9	47	2
SCSI-5	13.4	18.0	27/3%	27/3%	28
SCSI-6	3	2.4	34/14%	34/14%	2
SCSI-7	7.3	7.5	101/18%	101/18%	7
SCSI-8	2.7	2.6	44/13%	24.5/7%	1
SCSI-9	11	11	146/9%	145/9%	85
SCSI-10	5	4	42/14%	39/13%	4
SCSI-11	7	7	46/8%	47/8%	10
SCSI-12	3	3	55/12%	54/12%	1
SCSI-13	14	14	243/12%	244/12%	21
SCSI-14	1.5	1	30/4%	39/4%	3

Transect Geometry

Artifacts can be mistaken for structure in seismic reflection images and velocities can be incorrectly determined if geophones and/or shots locations have significant elevation and lateral variations and the are not included in processing the data. To account for variations in geometry, each shot point and geophone location was surveyed using an electronic distance meter (EDM) or a Global Positioning System (GPS) with theoretical accuracies of a few centimeters. We used GPS measurements along most of the seismic transect, but we used EDM measurements within the Santa Cruz Mountains, where 3-D satellite coverage (GPS) was limited steep canyons and by trees. The geometry data for the SCSI-HR survey are presented in Appendices A-O and are shown graphically in figures 5-18. These geometrical variations in the shot and recording arrays are compared with apparent structures observed on the reflection and velocity images to help differentiate among structure and possible artifacts.

On all seismic profiles, the shots were fired from the southward direction to the northward direction. Most of the 14 profiles were situated between California Highway 17 and Los Gatos Creek (Fig. 2), with varying distances from the Creek and Highway 17. Profiles SCSI-1 through SCSI-6 were consecutively oriented southward to northward, with a small amount of

overlap (<50 m) between the profiles. Profile SCSI-1 was about 60 m long, and it originated about 700 m northeast of the Lexington Dam. The data were recorded on one multi-channel seismograph with 13 live channels. Due to the short length of this profile, we did not process the data for structure. Although the data are available upon request, this profile will not be discussed further in this report. Profile SCSI-2 extended 495 m northward from the southern end of profile SCSI-1 (with ~25 m of overlap), and the SCSI-2 data were recorded on two multi-channel seismographs with 113 live channels. Profile SCSI-3 overlapped the northern end of profile SCSI-2 and extended 560 m northward (Fig. 2a). We used two multi-channel seismographs with 118 live channels to record the data along profile SCSI-3. Profile SCSI-4 extended 237 m from the northern end of SCSI-3 (Fig. 2a), and data were recorded on one multi-channel seismograph with 49 live channels. From the northern end of profile SCSI-4, profile SCSI-5 extended 818 m along the southeast side of California Highway 17 to Los Gatos High School (Fig. 2a). The SCSI-5 data were recorded on two multi-channel seismographs with 113 live channels. Because Los Gatos Creek crosses from the south side to the north side of Highway 17 near East Main Street in Los Gatos, the southern part of profile SCSI-5 was not coincident with Los Gatos Creek but was located across the freeway. Profile SCSI-6, recorded on one multi-channel seismograph with 50 live channels, extended 237 m northeast from the northern end of SCSI-5 along the southeast side of Hwy 17 (Fig. 2a).

Profiles SCSI-7 though SCSI-11 were located on the southeast side of Los Gatos Creek, between Los Gatos Creek and Highway 17. Due to the curvature of Los Gatos Creek and our desire to keep the profile as coincident with Los Gatos Creek as possible, we relocated profile SCSI-7 to the northwest side of California Highway 17 (Fig. 2a). Profile SCSI-7 originated southwestward of the northern end of profile SCSI-6, such that there was about 100 m of overlap between SCSI-6 and SCSI-7 in 2-D cross-sectional view. From its southern end point, profile SCSI-7 extended 543 m northward (Fig. 2a). We used two multi-channel seismographs with 118 live channels to record the SCSI-7 data. Profile SCSI-8 extended 338 m northeast of profile SCSI-7 (Fig. 2a), and the data were recorded on two multi-channel seismographs with 72 live channels. Ten geophones (~45 m) on the southwestern end of SCSI-8 were overlapped with 10 geophones on the northeastern end of profile SCSI-7. No shots were fired at the first 10 geophones along profile SCSI-8, but for the remaining stations along the profile, shot points were co-located with geophones. A sharp bend in Los Gatos Creek made it necessary to re-locate the southern end of profile SCSI-9 about 80 m northwest of the northern end of profile SCSI-8. In 2-D cross-sectional view, however, there is less than 50 m of offset between the two profiles. Profile SCSI-9 extended north 1543 m along the southeastern side of Los Gatos Creek and Vasona Reservoir (Fig. 2a). Due to the length of profile SCSI-9, the recording array moved multiple times during data acquisition. Two RX-60 seismographs with 120 live channels comprised the first recording array on the southwest end of the profile. We fired 63 shots into the southernmost part of the first array before moving the southernmost 60 channels northward to form the second recording array. We then fired an additional 64 shots into the second array before moving the southernmost 60 channels of the second array northward to form the third recording array. We fired 51 shots into the third array before moving 120 channels northward to form the fourth recording array. Eleven of the northernmost sites of the third array were reoccupied while recording the fourth array, with 120 shots fired into the fourth array. Profile SCSI-10 extended north 302 m from the northern end of SCSI-9 along the eastern side of Vasona Reservoir (Fig. 2a). We used two multi-channel seismographs to record the data, but only 68 of the 120 channels actively recorded data along the profile. Profile SCSI-11 was laterally offset about 200 m from SCSI 10 so that SCSI-11 would be coincident with Los Gatos Creek (Fig. 2a). Profile SCSI-11 extended 567 m north from Vasona Dam to about 60 m north of the Lark Avenue overpass (Figs. 2a,b). We used two multi-channel

seismographs with 120 live channels to record the data along profile SCSI-11. Profile SCSI-12 extended 447 m north from the northern end of SCSI-11 (Fig. 2b). We used two multi-channel seismographs with 97 live channels to record the data along profile SCSI-12.

Profiles SCSI-13 and SCSI-14 were located on the northwest side of Los Gatos Creek. Relative to the northern end of profile 12, the southern end of profile 13 was located about 50 m to the northwest, across Los Gatos Creek. In 2-D cross-sectional view, the two profiles overlapped by a few meters. Profile SCSI-13 extended northeastward 2043 m from the northern end of profile SCSI-12 (Fig. 2b). Profile SCSI-13 passed between several recharge ponds, under Hwy 85, through Los Gatos Creek Park, and ended at Camden Avenue in Campbell (Fig. 2b). We used two RX-60 seismographs with 120 live channels as the first recording array on the southeast end of the profile. We then shot 120 shots into the recording array before moving 120 channels northward to form the second recording array. We repeated the process, moving the recording array northeastward three additional times and shooting through the array each time. Along the profile, each recording array included geophones that overlapped with geophones of the previous recording array, whereby arrays 2, 3, and 4 had 10, 2, and 1 overlapping geophones, respectively. Profile SCSI-14 was located along the northwest side of Los Gatos Creek, northeast of Camden Avenue. The profile originated approximately 300 m northeast of the northern end of profile SCSI-13 and extended about 794 m to the northeast (Fig. 2b). Two multi-channel seismographs with 120 live channels were used to record the SCSI-14 data. We shot through the first 120-channel recording array before moving the southernmost 60 channels northeastward to form a second recording array. Thirteen of the southernmost geophones from the second recording array were overlapped with the northernmost geophones of the first recording array. Shots were then fired through the entirety of the second recording array.

Seismic Data and Data Processing

Cumulatively, we recorded more than 1700 shots along the SCSI-HR seismic transect. Signal-to-noise ratios varied locally along each profile and were strongly related to local cultural noises (including freeway noise, water pumps, and noises from homes and factories). Below, we present examples of shot gathers from each of the profiles comprising the SCSI-HR transect so that the variation in data quality can be seen (Figs. 19a-n). The shot gathers have been minimally processed, such that noisy or dead traces have been removed, and bandpass-filtering (25-50-100-200 Hz) has been applied. Three seconds of data were acquired in the field, but we present only 0.5 s of data in figures 19a-n. Although there was significant noise along much of the transect, due to the urban setting, seismic energy propagated maximum distances of about 600 m (the maximum length of the recording array) along many of the longer profiles, and reflected energy (hyperbolic arrivals following first-arrival refractions) is apparent on most shot gathers to varying distances (Fig. 19). In addition to the desired refraction and reflection seismic energy, other less desirable energy for reflection imaging, including surface waves, air waves, and/or multiples, are apparent on many of the shot gathers (Fig. 19). Most of the less desirable seismic energy did not affect our efforts in shallow-depth velocity imaging, but as discussed below, we expended appreciable effort to minimize the unwanted seismic energy.

Because we acquired the seismic data using a shoot-through method, we were able to develop both refraction (velocity) and variable-fold reflection images from the same data. The combined reflection and refraction data provide stronger constraints on the composition and structures of the shallow subsurface than having only one of the two types of data. Below, we describe the processing methods for the refraction data, and we present the resulting velocity models. We then describe the processing methods for the reflection data and present the

resulting reflection images. Individual profiles were analyzed separately, but we present them here as composite images to better understand the overall structure along the transect.

Velocity Analysis

First-arrival refractions from usable seismograms were used to develop 3-D P-wave tomographic velocity models of the shallow subsurface along each seismic profile. To pick first-arrivals, we bandpass filtered the seismic data with minimum frequencies of 35 Hz. First arrivals were first picked using an automatic picker in seismic processing program (ProMax™), but all arrivals were individually verified or repicked by a seismologist. We checked each arrival for consistency with its reciprocal travel time from shot and receiver pairs. All first-arrival reciprocal pairs were accurate to within 10 ms or less. To invert the first arrivals for velocity structure, we used a modified version of an algorithm by Hole (1992), whereby we parameterize the starting model into 5-m by 5-m vertical and horizontal grids, consistent with our shot and geophone spacing. As a check on the validity of the final models, we utilized multiple starting models, all of which yielded similar final models. In general, the velocity models are best resolved in the upper 50% depth range of the models, where the density of the ray coverage is highest. Checkerboard tests of the model resolution indicate that our resolution varies between about 20 and 50 m, with lower resolution near the base of the models. We vertically and horizontally smoothed the model during the inversion process, such that the final model was smoothed over distances and depths ranging from 10 to 20 m. The minimum depth of velocity imaging is related to the shot (5 m) and geophone (5 m) spacing, the model grid spacing (5 m), and the amount of smoothing used in modeling. The maximum depth of velocity imaging was limited by the maximum offset that clear first arrivals could be measured on the shot gathers (Fig. 19). Because of variable signal-to-noise ratios in the urban environment, clear first arrivals were measurable to varying distances for each shot, but first arrivals were measurable to minimal distances greater than several hundred meters from the source for many shots.

Seismic Velocity Images

Near-Surface Velocities

We present near-surface (~200 m or less) P-wave velocities along the SCSI-HR seismic profiles, and P- and S-wave velocities to greater depths along the SCSI-LR seismic profile, which was largely coincident with the SCSI-HR transect, are presented by Catchings et al. (2006). In this report, all depths discussed refer to depths below the ground surface (bgs) of the topographically lowest geophone along each SCSI-HR seismic profile. Due to a combination of high levels of urban noise, the small size of the seismic sources, and the short length of the actively recording array (600 m maximum), velocity imaging was limited to depths of 200 m or less along the SCSI-HR transect (Fig. 20). Generally, the shorter and noisier profiles yielded maximum velocity imaging depths significantly less than 200 m. Along the transect, measured velocities in the upper 200 m depth range from about 800 m/s to nearly 6500 m/s at varying locations and depths along the profile. Both the lowest and highest velocities along the transect are observed within the Santa Cruz Mountains. The lowest velocities occur in upper few meters of the subsurface, particularly where the transect was elevated relative to Los Gatos Creek or laterally offset from Los Gatos Creek, and these low velocities are likely due unsaturated near-surface sediments. The highest velocities along the transect are observed at depths of 100 to 200 m within the Santa Cruz Mountains along profiles SCSI-1 through SCSI-4. Although first-arrival travel times, from which the highest velocities were determined, were measured at the farthest shot-to-receiver offsets and are less reliably

determined than near-offset arrivals, we suggest that the higher velocities may be an accurate measure of the rock velocities. We discuss these higher velocities in sections below. Within each velocity model, there are localized areas (grids) lacking reversed ray coverage. However, to more clearly present and discuss the velocity models, we present the velocity models without differentiating such grids (Fig. 20). In this report, we discuss the variation in velocity along each seismic profile with special emphasis on the 1500 m/s P-wave velocity contour because it can be an indicator of water-saturated, unconsolidated sediments (Nur, 1982; Schon, 1996; Catchings et al., 1998; 1999a,b; 2001; Gandhok et al., 1999). We also note variations in the velocity structure that correlate with other anomalies observed on the seismic reflection images.

Profiles SCSI-2 through SCSI-6

Profiles SCSI-2 through SCSI-6 form a continuous series of profiles that extend from the elevated part of the Santa Cruz Mountains to the alluvial-covered valley within the foothills. Near-surface P-wave velocities along profiles SCSI-2 through SCSI 6 vary from 800 m/s in the near surface to as much as 6500 m/s at about 120 m depth (Fig. 20), but maximum and minimum velocities vary along each profiles. The highest (deepest) velocities are less well determined due to poor signal-to-noise ratios of the refraction data for some shots at far offsets, but because of the reciprocity discussed above, there are probably not significant errors in the data, suggesting that the modeled velocities are representative of the rocks at those depths. Velocities in excess of 6.5 km/s at 120 m depth are unusually high for most near-surface rocks, but these modeled velocities may result from localized high-velocity Coast Ranges Ophiolitic rocks. McLaughlin et al. (2001) reported that ultramafic rocks (including harzburgite and peridotite), which are high-velocity (8+ km/s) mantle rocks, have been serpentinized and thrust beneath near-surface Franciscan rocks along profile SCSI-2 (Fig. 3); these rocks likely exist in the shallow subsurface from profiles SCSI-2 through profile SCSI-6. Although serpentinization can result in lower-velocity rocks, such serpentinized ultramafics elsewhere in California have velocities in the range of about 6 km/s to 7 km/s (Carmichael, 1989). If such high-velocity rocks exist below profiles SCSI-2 though SCSI-6, these rocks are not likely to be more than a few hundred meters thick because the SCSI-LR seismic data, which averages velocities over 100 to 200 m, indicates lower maximum velocities (~4.0 km/s maximum) at shallow (~200 m) depths in the vicinity of profiles SCSI-2 though SCSI-6 (Catchings et al., 2006).

The largest variations in the depths of the relatively high-velocity rocks (>6 km/s) appear to occur across fault zones mapped at the surface or fault zones that are seismically imaged. Similar variations in the near-surface velocities are also observed along profiles SCSI-2 through SCSI-6 over the same mapped or seismically imaged fault zones. The variation in depth of the 1500 m/s velocity contour is particularly apparent across these apparent fault zones. Near meter 300 of profile SCSI-2, for example, velocities in excess of 1500 m/s are near the surface, but similar velocities are more than 35 m deep on the northeast end of profile SCSI-2. The significant change in the depth of the 1500 m/s velocity contour occurs across an extension of the Soda Springs Fault zone (Fig. 3), which is also inferred by offset reflectors on SCSI-HR reflection images and discussed later in this report. This abrupt change in depth of the 1500 m/s velocity contour along profile SCSI-2 may indicate that the Soda Spring fault zone acts as a ground-water barrier, with shallow-depth saturated (higher-velocity) sediments to the southwest, but the change in depth may also be related to a change in shallow-depth lithology (sediment types) across the fault zone. Similarly, along profile SCSI-3, the 1500 m/s velocity contour is about 20 m higher on the southern end of profile SCSI-3 relative to its depth on the northeastern end of profile SCSI-2, with the change in depth of the 1500 m/s contour occurring across a zone of reverse faults mapped at the surface (Figs. 3 and 20). Other significant variations in both the 1500 m/s and the deeper higher-velocity (>3 km/s) rocks

occur near meter 400 of profile SCSI-3, the central part of profile SCSI-4, northeast of meter 400 on profile SCSI-5 (across strands of the Berrocal Fault zone), and between the northern end of profile SCSI-5 and the southern end of profile SCSI-6. All of these changes in the depths of the 1500 m/s velocity contour and the depths of the higher-velocity rocks occur near the surface location of mapped faults or near apparent faults that were imaged on the seismic reflection images discussed later in this report.

There are variations in the linearity of profiles SCSI-2 though SCSI-6, and some of the variations in velocity structure may be attributable to the geometry of the recording array. However, we utilized a 3-D velocity inversion technique, which should account for such geometrical variations. Furthermore, we believe that geometrical variations have a limited effect on the velocity inversions because most large changes in the velocity structure do not coincide geographically with the variations in linearity of the profiles. For example, a significant change in velocity near the northern end of profile SCSI-2 is centered near meter 300, but the change in linearity of profile SCSI-2 occurs near meter 450 (Figs. 6 and 20). We cannot rule out the possibility that the velocity variations are related to the geometry on any of the SCSI profiles, but as discussed below, other images that are less sensitive to the geometry of the seismic profile show corresponding structures, suggesting that the velocity anomalies are due to structural complexities in the subsurface.

Profiles SCSI-7 though SCSI-8

Profiles SCSI-7 and SCSI-8 were located largely within the alluvial-covered parts of the Santa Clara Valley, but exposed rocks are observed both to the northwest and southeast of the profiles (Fig. 3). The maximum depth of velocity imaging along the profiles SCSI-7 and SCSI-8 varied along the two profiles, but minimum and maximum P-wave velocities range from 800 m/s near the surface to about 5500 m/s at 100 m depth, with the high velocities occurring on the extreme southern end of profile SCSI-7 (Fig. 20). Although the two profiles are separated by only a few hundred meters, relatively low velocities are observed at 100 m depth on the northern end of profile SCSI-5, whereas relatively high velocities (~5500 m/s) are observed at 100 m depth along the southern end of profile SCSI-7 (Fig. 20). Similarly, significant changes in the depths of the 1500 m/s velocity contour occur between profiles SCSI-5 and SCSI-7. This significant change in velocity occurs across an apparent fault zone imaged on the SCSI reflection images. Along the remainder of profiles SCSI-7 and SCSI-8, the depths to highest-velocity rocks (>2500 m/s) progressively decrease, with several-hundred-meter-wide zones of lower-velocity situated between several-hundred-meter-wide zones of higher-velocity, implying some type of horst and graben structures. For example, along profile SCSI-7, relatively high velocities are observed on both the southern and northern ends of the profile, separated by an approximately 200-m-wide zone of low velocities near the center of the profile. The central zone of low velocities (near meter 300) correlates with the projected location of a major strand of the Berrocal Fault zone (Figs. 3 and 20). Lower velocities within the Berrocal Fault zone are consistent with empirical studies that have shown most fault zones to be cored by low-velocity materials (Catchings et al., 2002).

Profiles SCSI-9 and SCSI-10

Profiles SCSI-9 was laterally offset about 200 m northwest of profile SCSI-8. However, the geological setting of profiles SCSI-9 and SCSI-10 is similar to that of SCSI-7 and SCSI-8, with alluvium immediately below the seismic profiles and exposed rocks northwest and southeast of the seismic profiles. P-wave velocities along profiles SCSI-9 and SCSI-10 range between 800 m/s near the surface to 3700 m/s in the upper 60 m (Fig. 20). As observed along profiles SCSI-5 through SCSI-8, profiles SCSI-9 and 10 are underlain by laterally varying low- and high-velocity zones below the near surface deposits. These laterally varying changes

in velocity are consistent with the apparent displacement of faults mapped in the adjacent by hills by McLaughlin et al. (2001). For example, the northern half of profile SCSI-5 and the southern half of profile SCSI-7 are located on an apparent down-dropped block, whereas the area from the northern tip of profile SCSi-8 to the southern tip of profile SCSI-9 is located along an up-thrown block. Overall, this pattern of uplifted and down-thrown blocks appear to persist along the alluvial-covered parts of the SCSI-HR transect (profiles SCSI-5 through SCSI-14), as the velocity images show a series of laterally varying high- and low-velocity zones (Fig. 20). This type of structure in the northern Santa Clara Valley has also been suggested on the basis of gravity measurements (CWDR, 1967).

Profile SCSI-11 through SCSI-14

P-wave velocities along profiles SCSI-11 though SCSI-14 range between 800 m/s near the surface to 4000 m/s within the upper 80 m (Fig. 20). As observed along the other alluvial-covered profiles, there are laterally varying high- and low-velocity zones, most of which occur in the vicinity of apparent faults that were seismically imaged on the SCSI reflection profiles. Because of the alluvial cover and the lack of exposed rocks near the seismic profiles, faults have not been mapped at the surface along profiles SCSI-11 through SCSI-14, except near the southern end of profiles SCSI-11. Variations in the depths to the 1500 m/s velocity contour also generally coincide with the apparent faults. Profile SCSI-14 was located about 300 m northwest of the McGlincey well, on the opposite (northwest) side of Los Gatos Creek. Sonic P- and S-wave velocities were measured in the McGlincey well, with P-wave velocities ranging from about 500 m/s near the surface to a maximum of about 3300 m/s at about 200 m depth. However, the majority of measurements ranged between 1500 m/s and about 2700 m/s. Similar velocities (~800 to ~2500 m/s) are observed on most of profile SCSI-14, but toward the center of the profile, maximum velocities (~4000 m/s) are significantly higher. Thus, for most westerly projections of McGlincey well onto the SCSI transect, the sonic and refraction velocities are consistent.

Reflection Data Processing

In seismic reflection data processing, we used procedures similar to those outlined by Brouwer and Helbig (1998). We chose to develop 2-D reflection profiles so that we could retain as much location precision as possible along the profiles. Processing steps included geometry installation, independent trace editing, timing corrections, elevation static corrections, AGC, bandpass filtering, F-K filtering (or surgical muting), velocity analysis (from refractions, semblence, and borehole-velocity measurements), NMO correction, stretch muting, common-depth-point (CDP) stacking, post-stack AGC, post-stack bandpass filtering, and post-stack deconvolution. Principal parameters used in processing each profile are shown in Table 2.

In trace editing, noisy traces (due to cultural noises) or redundant traces (due to nonlinear profile geometry) were removed from the shot gathers before stacking or migrating. Elevation statics, migration, and velocity analysis were accomplished using the tomographic velocity model from each profile. For depths below our tomography velocity model, we used velocities determined from the SCSI-LR profile (Catchings et al., 2006). We then compared those velocities with velocities determined from other methods, including velocities determined from semblence analysis, parabolic measurements, logs from nearby wells, and velocity-depth (pressure) relations (Christiansen, 1982; Carmichael, 1989).

Table 2. Processing parameters for the SCSI-HR profiles.

Profile	AGC Prestack Poststack(L) Poststack(H)	Filtering Notch Prestack Migration	Bandpass: Prestack Poststack(L) Poststack(H)	Migration (max freq, aperture, takeoff angle)	Decon (oper length, predict dist, time window)
SCSI-2	100 ms 25 ms 20 ms	60 Hz 27,60 Hz	35-70-200-400 35-70-140-280 75-150-300-600	400,50,30	100-27,0-1000
SCSI-3	100 ms 25 ms 20 ms	35, 60 Hz 27,35,60 Hz	35-70-200-400 15-30-200-400 75-150-300-600	400,50,30	100-23,0-1000
SCSI-4	100 ms 25 ms 20 ms	60 Hz 27,60 Hz	35-70-200-400 15-30-200-400 75-150-300-600	400,50,30	100-29,0-1000
SCSI-5	100 ms 25 ms 20 ms	60 Hz 27,60 Hz	35-70-200-400 15-30-200-400 75-150-300-600	400,50,30	100-23,0-1000
SCSI-6	100 ms 25 ms 20 ms	60, 100 Hz 27,60,100 Hz	35-70-200-400 35-70-140-280 75-150-300-600	400,50,30	none
SCSI-7	100 ms 25 ms 20 ms	60,71,100 Hz 27,60 Hz	35-70-200-400 35-70-140-280 75-150-300-600	400,50,30	100-27,0-1000
SCSI-8	100 ms 25 ms 20 ms	60 Hz 27,60 Hz	35-70-200-400 35-70-140-280 75-150-300-600	400,50,30	100-25,0-1000
SCSI-9	100 ms 25 ms 20 ms	60 Hz 27,60 Hz	35-70-200-400 35-70-140-280 75-150-300-600	400,50,30	100-25,0-1000
SCSI-10	100 ms 25 ms 20 ms	60 Hz 27,60 Hz	35-70-200-400 35-70-140-280 75-150-300-600	400,50,30	40-12,0-1000
SCSI-11	100 ms 25 ms 20 ms	60 Hz 27,60 Hz	35-70-200-400 35-70-140-280 75-150-300-600	400,50,30	100-23,0-1000
SCSI-12	100 ms 25 ms 20 ms	60 Hz 27,60 Hz	35-70-200-400 35-70-140-280 75-150-300-600	400,50,30	100-25,0-1000
SCSI-13	100 ms 25 ms 20 ms	60 Hz 27,38,60 Hz	35-70-200-400 35-70-140-280 75-150-300-600	400,50,30	100-23,0-1000
SCSI-14	100 ms 25 ms 20 ms	60,170 Hz 27,38,60 Hz	35-70-200-400 35-70-140-280 75-150-300-600	400,100,30	none

Imaging Methods

We developed multiple 2-D seismic reflection images for the SCSI-HR transect by stacking and migrating secondary arrivals from the same shot gathers used to develop the velocity image (Figs. 21-22). In this section, we discuss some of the physics and observations that are useful in understanding and interpreting the seismic images. We generated the stacked images by summing seismic energy from numerous shots along each profile. However, dipping, folded, or vertically offset (faulted) subsurface reflectors can result in incoherent images in the unmigrated images. The unmigrated images typically contain diffractions and scattered seismic energy within or across the fault zones that separate layers of differing velocities and densities. As such, the alignment of diffractions (hyperbolic arrivals on the seismic section) can be used to infer the location and dip of fault zones on unmigrated reflection images. To correct for the diffractions and the scattered energy, we applied Kirchoff prestack depth migration techniques to the seismic reflection data. We filtered the SCSI-HR data at relatively high minimum frequencies (35 Hz and 75 Hz) to develop the stacked and migrated images, and in this report, we compare those SCSI-HR images with SCSI-LR images, where 5-Hz seismic energy was used. The SCSI-LR data provide images to greater depths, but the resolution is much lower than that of the SCSI-HR data. Thus, the lower-frequency (SCSI-LR) data image a series of layers as a single reflector, whereas higher-frequency (SCSI-HR) data image individual thinner layers. For determining the overall structure over large depth ranges, the SCSI-LR data are

better, but to determine detail offsets in the shallow (upper 200 m), the SCSI-HR data are better.

A general formula (Dobrin and Savit, 1988) used to determine the minimum layer thickness needed to generate reflections is the one-quarter-wavelength criteria, where wavelength is:

λ = V/f, where V = velocity (m/s), λ= wavelength (m), and f = frequency (Hz):

and the radial width or length of the reflector is related to the Fresnel zone (*w):*

w = V/4 (sqrt(t/f)), where t is time (sec), V=velocity (m/s):

Stratigraphic layers that are at least as thick as (1/4λ) and at least as long as *w* will generate reflections. The minimum thickness (1/4 λ) of the reflectors varies with the velocity of the rocks, but assuming dominant frequencies of 35 Hz and average velocities of 1000 m/s, as determined in the near-surface (~10 m) along much of the SCSI-HR transect, the nearest-surface reflectors imaged on the 35-Hz images (Fig. 21) are at least 7 m thick and have radii of about 5 m. At 50 m depth, the 35-Hz data would image reflectors that are about 11 m or more thick, and the radii of the reflector would have to be about 24 m. For the high-frequency (~75 Hz) migrated sections, the resolutions would be approximately one-half those of the lower-frequency (35 Hz) images. Low-fold reflection images from the SCSI-LR profile (Catchings et al., 2006) were migrated with minimum frequencies of about 5 Hz. Assuming minimum velocities of about 2500 m/s in the upper 600 m, SCSI-LR reflectors would have to be about 125 m thick to generate reflections (Fig. 23). Thus, although the images are from two separate seismic surveys, the SCSI-LR image should show similar structures as the SCSI-HR image, but structures and layers would be averaged over about 125 m in the SCSI-LR images.

Seismic Reflection Images

Numerous sub-horizontal reflections are imaged in the upper few hundred meters of the SCSI-HR reflection images (Figs. 21-22). In the Santa Cruz Mountains (profiles SCSI-2 through SCSI-6), near-surface reflectors correlate with a range of rock types, including Quaternary deposits and Franciscan rocks (McLaughlin, et al., 2001). Strong diffractive energy and discontinuous or disrupted reflectors can be correlated with mapped surface faults in the Santa Cruz Mountains and the foothills, and where we observe similar features beneath the alluvial-covered areas of the SCSI transect, we also interpret faults. Below, we summarize the major structures observed in the reflection images along the seismic profiles.

Profiles SCSI-2 through SCSI-6

Profile SCSI-2 trended northeastward, adjacent to a contact between Quaternary deposits and Coast Ranges Ophiolitic rocks (Fig. 3). At the surface, a few strike and dip measurements suggest that rocks adjacent to profile SCSI-2 dip eastward or slightly northeastward, with local dips of 25 to 35 degrees (McLaughlin et al., 2001). Unmigrated reflection images show sub-horizontal (northward) apparent dips (5 to 10 degrees, with local dips up to 35 degrees) in the upper 50 m (Fig. 21). We emphasize that the seismic reflection images show apparent dips due to the nearly parallel orientation of the SCSI-2 seismic profile relative to the measured strike of the rocks. Migrated reflection images also show sub-horizontal strata with slightly northward dips (3 to 5 degrees) in the upper 50 m along most of profile (Fig. 22). On both unmigrated and migrated images along profile SCSI-2, there is an apparent change in structure between 50 and 200 m depth, whereby strata northward of meter 250 dip southward by as much as 20 degrees (Figs. 21 and 22). On unmigrated images, the apparent change in dip is accompanied by numerous diffractions (Fig. 21), and on migrated images (Figs. 22), individual layers appear to be near vertically offset, suggesting that the northern part of the SCSI-2 profile is faulted at several locations (Fig. 21b). Such an interpretation is consistent with geologic mapping near the northern end of profile SCSI-2 (Fig. 3), where thrust faulting has superimposed Franciscan

rocks over Coast Ranges Ophiolitic rocks. We label the imaged and/or mapped faults by number on figure 21b. The sub-parallel orientation of profile SCSI-2 relative to the thrust fault probably gives rise to the apparent south-dipping structure between 50 and 200 m depth. Imaged faults near meter 250 of the SCSI-2 seismic profile apparently do not extend to the surface, as the reflection image does not show vertical offsets of layers nearest to the surface (Fig. 21b). Between about 300 and 600 m depth, rocks along profile SCSI-2 are poorly imaged on the unmigrated reflection image, perhaps due to diffractions (Fig. 21). However, on the migrated image, the strata appear discontinuous over distances of several hundred meters with highly variable dips (Figs. 22). McLaughlin et al. (2001) show that this part of the SCSI-HR transect is disrupted by faults of the Soda Spring Fault zone. We interpret the near-surface sub-horizontal strata to be either layered Quaternary sedimentary deposits from Los Gatos Creek or weathering horizons (Figs. 21b). Faulting apparently occurs along multiple strands with vertical displacements that are difficult to determine because we cannot identify a discrete horizon that has been offset; instead, it appears that many horizons are offset, and we do not know which horizons match across the fault (Figs. 21 and 22). However, when viewed with lower-frequency data of the SCSI-LR seismic image, thick packages of reflectors apparently form a single reflector, and vertical displacements are apparent (Figs. 23, 24d and 26b,c).

Surface rocks along profile SCSI-3 consist of Quaternary alluvial and stream deposits, with Franciscan rocks exposed on the adjacent hills. The correlation between surface dips of strata and dips imaged seismically is uncertain because there are no strikes and dips mapped at the surface along profile SCSI-3. The closest reported measurement of dip (31 degrees northwestward) was made east of the profile, but profile SCSI-3 is largely sub-parallel to the measured strike (Fig. 3a). In unmigrated reflection images, layers in the upper few tens of meters are largely sub-horizontal, with slight (2 to 3 degrees either northward) apparent dips (Fig. 21). Near-surface, sub-horizontal strata appears to be less than about 20 m thick, but some of that apparent layering may be due to weathering horizons in the rocks. On migrated images (Fig. 22), strata in the upper 75 m are sub-horizontal to north dipping (up to 30 degrees locally). Shallow layers along profile SCSI-3 are vertically offset (Fig. 22) and diffractive (Fig. 21) along most of the profile, particularly along the southern half of the profile where McLaughlin et al., (2001) mapped multiple faults at the surface (Fig. 3a). At depth (> 150 m depth), the unmigrated images are diffractive, and on migrated images, the images show discontinuous strata, probably inferring multiple faults (Figs. 21 and 22). The deeper layers on the southern half of profile SCSI-3 are mostly sub-horizontal, but strata on the northern half of the profile dip southward, suggesting that the principal fault zone is centered near meter 250 (Fig. 22). From about 250-600 m depth, the dips of reflectors are variable, ranging from sub-horizontal to nearly 15 degrees northward and southward (Figs. 21-22). Reflections observed on the SCSI-LR low-fold reflection image, which are averaged over about 125 m, show the same general pattern (Figs. 23, 24d and 26b,c). McLaughlin et al. (2001) show faults of the Lim Kiln Fault zone project to the southern end of the SCSI-3 seismic profile (Fig. 3). However, the most prominent apparent fault imaged between meters 200 and 300 is unmapped at the surface (Figs. 3a, 24).

Shallow (upper ~25 m) layers along profile SCSI-4 are largely sub-horizontal (Figs. 21 and 22). Surface strata along the profile consist mostly of Quaternary alluvial and stream deposits, but Franciscan Complex rocks and Santa Clara Fm rocks are exposed on the adjacent hills. Few strikes and dips of strata are mapped along profile SCSI-4, and because numerous faults strands are inferred to cross the profile, it is difficult to correlate the surface geology with the seismic images. The sub-horizontal reflections suggest that near-surface sediments or weathered rock horizons are relatively thin (< 25 m) along profile SCSI-4 (Figs. 21-22). On unmigrated images (Fig. 21), numerous diffractions are observed at discrete locations along the

seismic profile, and on migrated images (Fig. 22), the strata are vertically offset in the same vicinity as the diffractions seen on the unmigrated image. The combination of the diffractions and the vertically offset layers geographically correlate with many of the mapped faults inferred to cross profile SCSI-4 (Figs. 3 and 22). Several of these faults appear to locally alter the dip of the underlying strata (Figs. 21 and 22). Most of the strata between about 25 and 75 m depth dip southward, but high-angle dips (>20 degrees) are apparent on the northern half of the seismic profile. Below about 75 m depth, much of the strata are sub-horizontal to slightly south-dipping (Fig. 22). The SCSI-LR and the SCSI-HR transects were not coincident along parts of SCSI-3 and SCSI-4, but the imaged structures are largely similar on the two migrated images (Figs. 22 and 24d).

Surficial deposits along profile SCSI-5 consist of Quaternary stream deposits, but rocks on the adjacent hills include Franciscan Complex rocks, Santa Clara Fm rocks, and Quaternary alluvial deposits. McLaughlin et al. (2001) do not report measurements of strikes and dips for the nearby rocks. Near-surface sub-horizontal reflections vary in thickness from about 20 m to about 100 m, with the thickest strata located northward of meter 450 (Figs. 21d and 24d). At about meter 450, the Berrocal fault zone (reverse fault) is inferred to cross the seismic profile (Fig. 3), which probably accounts for the thicker sub-horizontal strata (sediments) north of meter 450. On unmigrated and migrated reflection images, diffractions and vertical offsets of layers, respectively, coincide geographically (Figs. 21 and 22), suggesting multiple strands in the fault zone. Several unmapped fault strands are also apparent between the principal strands of the Berrocal Fault and the northern end of profile SCSI-5 (Fig. 3), as indicated by offset strata and diffractions on the seismic images (Figs. 21 and 22). However, some of the apparent fault strands do not extend to the surface. Most of the strata below about 100 m depth on the southern half of the profile are sub-horizontal, but strata north of meter 450 and below 100 m depth mostly dip northward. Averaged over 125-m intervals, the SCSI-LR low-fold reflection image shows largely the same dips and apparent fault zones as seen on the SCSI-HR reflection image (Figs. 22, 23 and 24). The relatively steep northward dips of the deeper (> 200 m) strata and the apparent fault-disrupted layers seen on the SCSI-LR reflection image (Fig. 26a) do not image well on the SCSI-HR reflection image (Fig. 24b), largely due to the relatively narrow recording aperture of the SCSI-HR seismic survey. Similar poorly reflective images are observed along profiles north of profile SCSI-9 that have steeply dipping (15-20 degrees) strata at depths greater than 200 m.

Because the northern half of profile SCSI-6 was parallel to the southern 100 m of profile SCSI-7, which was located on the northwestern side of the California Highway 17, profiles SCSI-6 and SCSI-7 overlap in 2-D cross-sectional view (Figs. 21-22). To provide an un-obscured view of profile SCSI-6 and SCSI-7, we also present the images separately from the 2-D SCSI cross-sectional view (Fig. 25). Surficial materials along profile SCSI-6 are principally Holocene levee, Pleistocene alluvial fan, and Pleistocene and Pliocene Santa Clara Fm deposits (Fig. 3). However, Miocene Monterey shale is exposed on nearby (< 1 km) hills to the southeast of SCSI-6. All of these deposits likely underlie profile SCSI-6. Strikes and dips of Quaternary deposits are not mapped near profile SCSI-6, but strikes and dips of Quaternary deposits are highly variable (0 to 50 degrees) where they are exposed on the nearby hills (Fig. 3). The greatest variation in strikes and dips occur near mapped faults. Along the southwestern Santa Clara Valley segment of the profile SCSI-6, similar rocks and structures to those inferred beneath profile SCSI-5 likely exist beneath the alluvium, as reflectors on the northern end of profile SCSI-5 are similar to those on the southern end of profile SCSI-6. However, there are significant disruptions of reflectors near the center of profile SCSI-6, with vertically offset layers on both the migrated images (Figs. 22) and diffractions on unmigrated images (Figs. 21 and 25), suggesting an unmapped fault that trends through profile SCSI-6.

No fault is inferred at the surface from geologic mapping (McLaughlin et al., 2001), but the area is covered by alluvium. The significant vertical offsets and apparent change in the reflectivity imaged along profile SCSI-6 suggest that the fault may be one of the major basin bounding faults of the western Santa Clara Valley, with vertical offsets of more than 100 m at depth. The SCSI-LR reflection image suggests that the fault zone along profile SCSI-6 also marks a significant change in the dip of strata along the SCSI transect (Figs. 23 and 24). The SCSI-HR reflection image shows that this apparent basin-bounding fault extends to the near surface (Figs. 21 and 22).

Profiles SCSI-7 and SCSI-8

Profile SCSI-7 was located on the opposite (northwest) side of California Highway 17 relative to profile SCSI-6, and as explained above, profiles SCSI-6 and SCSI-7 overlap in 2-D cross-sectional view. The geology along profile SCSI-7 is similar to that described for profile SCSI-6, except there are fewer Holocene levee deposits along profile SCSI-7. Near-surface, sub-horizontal strata vary laterally in thickness, ranging from about 40 to 70 m (Figs. 21 and 22). Although several hundred meters separate profiles SCSI-6 and SCSI-7, many of the same reflectors are apparent on both profiles. Most strata are sub-horizontally layered along profile SCSI-7, with slight dips northward. Near-vertical offsets (60 to 80 m) of reflectors between meters 300 to 400 of profile SCSI-7 (Figs. 21 and 22) are probably fault related because they also generate diffractions on the unmigrated reflection images (Fig. 21). This apparent fault zone coincides with the general location of an inferred strand of the Shannon fault zone (Fig. 3). Near-vertical offsets on the SCSI-LR seismic reflection image are relatively small along the area that geographically corresponds to profile SCSI-7 (Figs. 23 and 24), suggesting that the imaged and mapped fault is not a major fault or it has more horizontal offset than vertical offset. SCSI-8 has much the same geological setting as described for profile SCSI-6. Most of the near-surface reflectors appear continuous, except near meter 250 where an apparent fault zone is indicated by abrupt thinning of near-surface layers, diffractions on the unmigrated reflection images (Fig. 21), and vertical offsets on the migrated reflection images (Fig. 22). Most layers are sub-horizontal to north-dipping along the profiles. The SCSI-LR reflection image also shows largely sub-horizontal strata and apparent offsets along a near-vertical fault zone in the area that corresponds to profile SCSI-8 (Fig. 24).

Profile SCSI-9 and SCSI-10

The southern end of profile SCSI-9 is laterally offset by about 200 m from the northern end of profile SCSI-8. The surface geology along SCSI-9 consists of Pleistocene and Holocene alluvial fan deposits, but Santa Clara Fm rocks are located at the surface a few hundred meters to the northwest (Fig. 3). In the upper ~50 m, the reflectors are largely sub-horizontal, but they appear to be folded and faulted at multiple locations along profile SCSI-9. Prominent vertical offsets and truncations of layers between meters 200 and 300 and between meters 1000 to 1300 correlate with projected strands of the Berrocal and Shannon fault zones (Figs. 3a, 21, and 22). On the basis of diffractions (Fig. 21) and vertically offset reflectors (Fig. 22), other fault strands are likely present along the seismic profile, but some of these faults do not displace the shallowest layers and are not exposed at the surface (Fig. 21). Between meter 1200 and the northern end of profile SCSI-9, sub-horizontal strata overlie a northeast dipping discontinuity (Fig. 21). Lithologic logs interpreted from three wells (H.H. Main wells) located in the vicinity of the northern end of profile SCSI-9, along profile SCSI-10, or along profile SCSI-11 are interpreted by Stanley et al. (2002) as containing about 15, 36, and 42 m of Quaternary sediments. These Quaternary sediments are interpreted as overlying Tertiary Monterey Formation rocks. The exact locations of the H. H. Main wells are not known, but the H. H. Main wells were probably located somewhere between meter 1300 of profile SCSI-9

and about meter 50 of profile SCSI-12. Based on interpretations by Stanley et al. (2002), the wells project to the SCSI transect at meter 1300 of profile SCSI-9 and meter 275 of profile SCSI-11. On unmigrated images, rocks northeast of meter 1200 and below 200 m depth of profile SCSI-9 are much less reflective in unmigrated images than those rocks southwest of meter 1200 and above 200 m depth (Fig. 21). However, on migrated images, these rocks are reflective (Fig. 22), suggesting that there is structural complexity (faulted or dipping strata) in or around meter 1200 of profile SCSI-9. Comparison of the SCSI-HR images with the SCSI-LR image suggests that the low reflectivity below about 200 m depth (Fig. 21) results from steeply northward dipping strata that was poorly imaged due the short aperture of the SCSI-HR arrays (Fig. 24). The change in dip of the deeper layers occurs along unmapped faults (meters 1300 to 1475) that are probably part of the Berrocal fault zone (Figs. 24-25).

Rocks along profile SCSI-10 mainly consist of Pleistocene and Holocene alluvial fan deposits, with Santa Clara Fm rocks exposed a few hundred meters to the northwest and Tertiary Monterey Shale deposits exposed about 2 km to the southeast (Fig. 3a). Reflectors in the upper 50 m are largely sub-horizontal. On unmigrated high-resolution reflection images (Fig. 21), both shallow (< 50 m) and deeper (200+ m) strata appear to be folded, and there appear to be near-vertical offsets of reflectors. However, the shallow (50 m) strata appear to be less folded than the deeper strata, with a discontinuity between the strata that dips northward. Correlation with well data (Stanley et al., 2002) suggests that the discontinuity marks the boundary between Quaternary sediments and Miocene sediments (Fig. 21). Individual layers within the Quaternary sediments dip northward (~3 degrees) from the southern end profile SCSI-10 to about meter 150, but from about meter 150 to the northern end of the profile, layers in the upper 50 m largely dip southward (~2.5 degrees). Near meter 150, reflectors in the upper 50 m are vertically offset by about 10 m, and reflectors between 50 and 200 m appear vertically offset and folded, suggesting an unmapped fault that extends to within a few meters of the surface. This fault is probably part of the general fault zone that is mapped a few hundred meters to the northwest within Santa Clara Formation deposits (Fig. 3a). Strata below about 200 m are poorly reflective on unmigrated images (Fig. 21), suggesting relatively high-angle dips or disrupted layers below that depth range, as shown on the SCSI-LR reflection image (Fig. 24d) along SCSI-10. Where the strata are not disrupted, there appears to be a general northward dip of layers in the 200 to 600 m depth range (Fig. 24d).

Profile SCSI-11 through SCSI-14

Reflectors in the upper 100 m along profile SCSI-11 dip gently northward and are continuations of those seen along profile SCSI-10. Surficial geological materials are similar to those described along profile SCSI-10, except the northern end of profile SCSI-11 approaches within a few tens of meters of Santa Clara Formation rocks exposed in the nearby hills. As observed on profile SCSI-10, near-surface deposits along profile SCSI-11 are largely sub-horizontal, but they appear disrupted along most of the profile in both migrated and unmigrated images (Figs. 21 and 22). The near-surface deposits thicken toward the northeast and appear to be underlain by folded strata (in unmigrated sections) that have been vertically offset in places (Fig. 21). These vertical offsets may be fault strands of the Monte Vista fault zone (Fig. 3) as inferred by McLaughlin et al. (2001). Reflectors below about 200 m depth are weakly reflective, with sub-horizontal and north-dipping reflectors between 200 and 600 m depth. The SCSI-LR reflection image (Fig. 24) shows disruptions in strata along profile SCSI-11, with apparent folds in rocks below about 300 m depth.

The surficial geology along profile SCSI-12 is similar to that along profile SCSI-11. Near-surface sub-horizontal strata along profile SCSI-12 are about 100 m thick and are less disrupted than the near-surface strata along profile SCSI 11. However, within the upper 20 m depth, there are minor vertically offset strata near meter 100 and folded and offset strata near

meter 350 of profile SCSI-12. The vertically offset strata near meter 100 (Fig. 21 and 22) are along the southwestern projection of a mapped fault, possibly part of the Monte Vista fault zone (Fig. 3 and 21). On unmigrated images (Figs. 24c), the strata below about 100 m are weakly reflective due to dipping strata, faulting, and folding, as seen on the SCSI-LR reflection image (Fig. 24d). Such folded and faulted strata at depths greater 100 m do not image well on unmigrated images because of the small aperture of the SCSI-HR arrays.

Surficial geological materials along profile SCSI-13 consist principally of Holocene levee deposits and alluvial fan deposits (Fig. 3b), but older Pleistocene deposits occur within a few tens of meters of parts of profile SCSI-13. The near-surface reflectors vary in thickness and dip direction along the profile, and the Quaternary-Miocene discontinuity generally dips northward (Fig. 24). On unmigrated reflection images, diffractions are observed near meters 300, 1050, and 1600 (Fig. 21), and a near-surface fold is observed between meter 1600 and 2000. On migrated reflection images, the same areas of profile SCSI-13 have vertically offset strata (Fig. 22) that likely outline a series of faults along the profile (Fig. 21). The apparent fault located near meter 1050 approximately coincides with the New Cascade fault inferred by Hanson et al. (2004) on the basis of ground-water offsets. The apparent fault near meter 1600 of profile SCSI-13 appears to be associated with a significant anticline that has uplifted strata by about 400 m over a lateral distance of about 1400 m (Fig. 24d). Strata within the upper 15 m or less appear to have been faulted near the apex of the fold (~meter 1600 of profile SCSI-13), with apparent vertical offsets of Holocene strata. Because of the large (~2 km) amplitude of the fold and because Miocene and Holocene strata are offset (Fig. 21), it is likely that this fault zone has been active over a long period of time.

Reflectors are not well imaged on the SCSI-14 image (Fig. 21), but the reflectors along the southernmost 200 m of profile SCSI-14 are similar to those on the northern end of profile SCSI-13. Surficial geological materials consist of Holocene levee deposits and alluvial fan deposits, and on migrated reflection images, near-surface sub-horizontal strata appear to be about 40 m thick along profile SCSI-14 (Fig. 22). Strata appear to be disrupted at several locations along the SCSI-14 profile, including near meters 200 and 700 (Fig. 21 and 22). We interpret northward-dipping strata at about 175 to 200 m depth on the southern end of the profile to be the contact between Quaternary and Miocene sediments. An approximately 250-m-deep (McGlincey) well with lithologic and geophysical well logs was located about 300 m east of the SCSI-14 profile. The well, referred to as the McGlincey well, is interpreted to have encountered Miocene rock at about 240 m depth (Newhouse et al., 2004), suggesting that Quaternary rocks are at least 240 m deep near the northern end of profile SCSI-14. Although it is difficult to correlate a specific reflector with the contact between the Quaternary and Miocene on the SCSI-14 reflection image, we observe dipping reflectors that may constitute the contact in the 250 m depth range (Fig. 21). On the SCSI-LR reflection image, however, there is a reflector that can be better correlated with the base of the Quaternary at about 250 m (Figs. 23 and 24). The SCSI-LR reflection image also shows that reflectors are disrupted and vertically offset in the areas corresponding faults interpreted on profile SCSI-14.

Possible Seismic Imaging Artifacts

Apparent disruptions in stratigraphic layers occur along most of the seismic transect. At these locations, the reflection image is distorted by diffractive energy, which is often associated with faults. However, the degradation of the reflection image may also result from the non-linear geometry of the seismic array in specific locations, but this is an unlikely scenario along most of the SCSI-HR transect for multiple reasons. First, the location and degree of disruption of the layers do not correlate with the location and degree of curvature of the seismic profiles (Figs. 5-18). Second, vertical offsets in the sedimentary layers persist beyond the areas of

curvature of the seismic profiles. Third, there are similar disruptions in areas where the seismic array is linear. Fourth, most disrupted reflectors also correlate with zones of relatively low velocities (Fig. 20), which often correlate with fault zones (Catchings et al., 2002). Fifth, many of the apparent faults on the reflection images correlate with faults mapped at the surface or inferred at the surface. Sixth, most of the same general features (faults, folds, stratigraphy) are imaged on both the SCSI-LR and SCSI-HR images, even though the two reflection images were developed independently (Fig. 24). Furthermore, the SCSI-LR transect was linear in some of the places where prominent faults were observed on both transects. On the basis of these observations, we suggest that the majority of disrupted layers result from structural complexities in the Earth, such as faults and folds.

Interpretation and Discussion

The complex tectonic setting and history of the eastern Santa Cruz Mountains and the western Santa Clara Valley make interpretation of seismic velocity and reflection images difficult. Within the Santa Cruz Mountains, multiple fault zones with northeast and southwest dips and both strike-slip and reverse motions (Dietz and Ellsworth, 1997; Simpson, 2004) are superimposed upon rocks ranging in composition from sedimentary to ultramafic (McLaughlin et al., 2001). If similar tectonism and structural complexity are present beneath the alluvium of the western Santa Clara Valley, seismic images of the structures would be difficult to interpret, especially for the deeper (older) structures. By combining the reflection and refraction images with other data, such as seismicity data, geologic mapping, and borehole data, we present non-unique interpretations of the upper 600 m of the crust (Fig. 26), and we relate these interpretations to factors important in evaluating water resources and earthquake hazards. Many of these separate geophysical observations are consistent, leading to similar interpretations.

Near-Surface Geology

The near-surface geology along the SCSI-HR seismic transect can be inferred on the basis of surface geology, borehole data, and seismic (velocity and reflection) data presented in this report (Figs. 21 and 26). Within the Santa Cruz Mountains, nearby surface rocks along the SCSI-HR transect are largely Franciscan and older rock. Nearer to the valley, in the vicinity of Los Gatos, surface rocks to the north of the SCSI transect are largely Pleistocene and Pliocene Santa Clara Fm sediments, and surface rocks to the south are mostly Miocene sedimentary rocks. Along the seismic profiles, these older rocks are likely overlain by Quaternary deposits along Los Gatos Creek. In the vicinity of the SCSI-HR transect, rock types include Franciscan melange, shale, limestone, volcanic rocks, sandstone, chert, and ultramafic rocks. As described above, ultramafic rocks (Coast Ranges Ophiolite) are exposed at the surface adjacent to the parts of the SCSI-HR transect, and these rocks are likely imaged in the near surface along parts of the seismic transect. At depths of 100-200 m, these rocks appear to have maximum velocities of about 6500 m/s (Fig. 20). Although there is some uncertainty regarding these modeled velocities, they are consistent with velocities measured for near-surface serpentinized ophiolites (harzburgite and peridotite) found elsewhere in California (Carmichael, 1989). Similar high velocities that are apparent along profiles SCSI-3 and SCSI-4 suggest the presence of these ultramafic rocks along those profiles at relatively shallow depths. In reflection images, these rocks are poorly reflective at low frequencies on unmigrated images (Fig. 21), but these rocks are more reflective on higher-frequency migrated images (Figs. 22). The change in reflective character suggests that the rocks are thinly layered. We conclude that the possible ultramafic rocks along the Santa Cruz Mountains segment of the SCSI-HR transect are probably no more than a few hundred meters thick because the average velocity

(over several hundred meters depth) on the SCSI-LR velocity image no more than about 4000 m/s (Catchings et al., 2006).

Whereas near-surface rocks in the Santa Cruz Mountains are generally high in velocity, lower-velocity deposits dominate the near-surface geology of the Santa Clara Valley. These low-velocity deposits include Quaternary (Holocene to Pleistocene) sediments, such as levee deposits, alluvial fan deposits, and Santa Clara Fm (Figs. 3 and 4). From the Santa Cruz Mountains to Vasona Dam, the near-surface Quaternary deposits are generally less than about 50 m thick, varying locally near fault zones. From Vasona Dam to the northeast end of the SCSI-HR transect, Quaternary deposits generally thicken northeastward, also varying locally along and between faults and folds. The Quaternary deposits appear to be underlain largely by Miocene sedimentary rocks. The contact between the Quaternary and older materials appears to be faulted in multiple locations, but the average dip of the contact is about 7 to 10 degrees northward. In most places, the Quaternary and older strata do not dip at the same angles (Fig. 24). High-frequency, migrated images indicate that the Quaternary sediments were deposited onto older sediments that dip both northward and southward at various locations along the transect (Fig. 22). The near-surface rocks along the entire SCSI-HR transect appear to be faulted, although the density of near-surface faults appears to be less northeast of Vasona Dam. The number of faults seismically imaged within the Santa Cruz Mountains segment of the transect appears to be similar to those mapped by McLaughlin et al. (2001), but within the Santa Clara Valley, our seismic images suggest that there are significantly more faults beneath the alluvium than is inferred from geologic mapping.

Rocks and Structures Below the Quaternary to 600 m

The overall structure along the SCSI-HR transect to 600 m depth can be interpreted from a combination of the SCSI- and SCSI-LR seismic images (Figs. 24 and 26). From the Santa Cruz Mountains to downtown Los Gatos (Berrocal Fault zone), rocks underlying the near-surface deposits consist of faulted and folded Franciscan and older metamorphic rocks (Figs. 3 and 24), but northeast of downtown Los Gatos (Berrocal Fault zone), we interpret rocks below the near-surface Quaternary deposits to be Miocene sedimentary rocks to at least 600 m depth. We base our interpretation on several observations. First, northeast of Vasona Reservoir, lithologic well logs and cuttings indicate that Miocene sedimentary rocks underlie the Quaternary deposits (Stanley et al., 2002; Newhouse et al. 2004). Second, on the SCSI-LR reflection images, these sedimentary rocks appear to be faulted, but similar reflectors can be identified along the entire Santa Clara Valley segment of the SCSI transect (Figs. 24 and 26). Third, Miocene rocks are exposed at the surface about 1 km to the southeast along the flanks of the Santa Cruz Mountains (Fig. 3). These Miocene rocks likely extend northwestward approximately 1 km to underlie the SCSI-HR profile (Fig. 3).

From the profile SCSI-4 in the Santa Cruz Mountains to profile SCSI-6 at Los Gatos High School, the Miocene deposits appear to be highly faulted within the Berrocal Fault zone, and the overall Miocene section appears to dip northward at about 18 degrees (Figs. 2 and 26). Near Los Gatos High School (profile SCSI-6), the Miocene strata appear to be tightly folded along a prominent reverse fault (fault #9 on fig. 26c). For purposes of discussion, we refer to this fault as the Los Gatos fault (#9). Although the Los Gatos fault is unmapped at the surface (McLaughlin et al., 2001), it appears to be one of the most prominent basin-bounding faults of the western Santa Clara Valley because this fault marks the change from north-dipping Miocene strata in the northeastern Santa Cruz Mountains to sub-horizontal-dipping strata in the Santa Clara Valley. The Los Gatos fault may be a prominent strand of the Berrocal fault zone, but McLaughlin et al. (2001) show the principal reverse fault of the Berrocal Fault zone to be several hundred meters south of Los Gatos fault.

From a few hundred meters northeast of Los Gatos High School to the central part of Vasona Park, sub-horizontal Miocene rocks appear to be locally disrupted along a series of faults (# 10 -15 on fig. 26c) that cause minor local folding. These faults are probably part of the Shannon Fault zone because they exhibit similar structure as mapped by McLaughlin et al. (2001) for the Shannon Fault zone. In particular, the faults appear to bound a series of horst-and-graben structures that are about 300 to 600 m wide (Fig. 24). On unmigrated SCSI-HR reflection images, the sub-horizontal Miocene strata are highly reflective to at least 600 m depth (Fig. 26a), but these deposits are probably about 1.6 to 1.8 km thick in the area of Vasona Reservoir based on our interpretation of our SCSI-LR reflection and velocity images (Catchings et al., 2006). The deeper images of the Miocene strata on the unmigrated SCSI-HR image are likely due the fact that these layers are largely sub-horizontal in this area (Fig. 26).

From the central part of Vasona Park to approximately Lark Street, rocks below the Quaternary sediments dip northward at about 10 degrees along a series of faults that may comprise the Monte Vista Fault zone (faults # 17 and 18; fig. 26c). Similarly, the base of Quaternary sediments also dips northward at about 7 to 10 degrees but is apparently faulted in many places. Near Lark Street, Quaternary and Miocene strata appear to be tightly folded along the possible Monte Vista Fault zone. From Lark Street to Vasona Junction (Figs. 2b and 26), Miocene strata are uplifted between two oppositely dipping faults, with mild folding of the strata between the two faults. Because strata do not dip steeply in this area, the strata are imaged to at least 600 m depth on the unmigrated SCSI-HR reflection images. From Vasona Junction to the approximate center of the recharge (percolation) basins (Fig. 2b), Miocene strata in the upper 600 m form an approximately 1-km-wide syncline asymmetric syncline. Strata on the south side of the syncline dip about 14 degrees northward, and on the north limb of the syncline, the Miocene strata dip about 18 degrees southward. The near-surface Quaternary strata in this area is largely sub-horizontal, except near faults, and as observed elsewhere along the SCSI transect, the dipping strata are not imaged below about 200 to 300 m on the SCSI-HR image (Fig. 26a). However, the dipping strata are well imaged on the SCSI-LR reflection image (Fig. 26b). The northern limb of the syncline is also the southern limb of an approximately 400-m-high set of anticlines beneath the Campbell area. For discussion purposes, we refer to these folds as the Campbell folds. The Campbell folds are the largest structures observed in the upper 600 m along the SCSI-HR profile, with greater local relief of Miocene strata than is observed in the Santa Cruz Mountains at similar depths. Both the SCSI-HR and SCSI-LR reflection images show the folds to be faulted in several locations. One of these faults southwest of the City of Campbell is located within 100 m of an apparent fault that Hanson et al. (2004) inferred on the basis of ground-water studies (fault # 20). This New Cascade fault and several additional faults to the north form an apparent fault zone that buttresses the northern ends of the Campbell folds (faults # 21 and unmarked faults). We refer to these northern faults as the Campbell Fault zone, but one or more of these faults may belong to previously inferred Stanford/Cascade fault zone (Bortugno et al., 1991). Faults of the Campbell Fault Zone appear to be more vertically oriented in the near surface than most of the faults to the southwest. The large vertical displacements (including Quaternary sediments) along the Campbell folds suggests that the Campbell Fault zone has been active longer, the vertical component of its slip rate is greater, and/or the overall slip rate is greater than the other faults along the SCSI-HR transect.

Cumulative Evidence for Faulting Along SCSI Transect

In this section, we discuss the cumulative evidence for near-surface faults and their relation to deeper seismically active faults. Along the SCSI-HR transect, faults are mapped at the surface in the northeastern Santa Cruz Mountains and southeastern Santa Clara Valley, and thus, are known to exist along the transect (McLaughlin et al., 2001). Evidence for faults

northeast of Vasona Park (Monte Vista fault zone?) was previously based on gravity and ground-water data from a 1960's study (CDWR, 1967) and was believed to be speculative by many researchers. However, on the basis of our study, we find multiple lines of evidence for faults within the alluvial-covered Santa Clara Valley. The principal SCSI seismic evidence for the existence of shallow-depth (~600 m) buried faults beneath the western Santa Clara Valley include: (1) near-vertically offset reflectors, (2) abrupt lateral variations in seismic velocities, (3) vertical offsets in the apparent water table (as inferred by the 1500 m/s velocity contour), and (4) folded near-surface and deep strata (Fig. 26). Many of the near-vertically offset reflectors occur beneath or near fault zones mapped or inferred at the surface in the southwestern part of the valley; thus, this same pattern of near-vertically offset reflectors that is seen beneath the alluvial-covered parts of the valley are taken to be indicative of faulting beneath the alluvium. We suggest that offset reflectors are particularly strong evidence because the offsets are observed on both the SCSI-HR and SCSI-LR reflection images in similar geographical locations, even though the images were developed from two separate data sets, the transects are not everywhere coincident, and the transects do not have the same resolution. These observations suggest that the displacements occur over distances and depths of at least hundreds of meters.

Another indicator of faulting is the coincidence of relatively the low P-wave velocities and imaged faults on SCSI-HR seismic reflection images, as most fault zones elsewhere are known to be cored by relatively low seismic velocities (Aki and Lee, 1976; Mooney and Luetgert, 1982; Catchings et al., 2002). Along the SCSI-HR transect, we observe low-velocity anomalies within most fault zones that are identified in the seismic reflection images. Many near-surface faults are also indicated by vertical variations in the 1500 m/s velocity contour (likely top of the ground-water table) along the transect (Fig. 24). Such vertical variations likely occur because many faults act as barriers to ground-water flow, resulting in differing depths to the ground-water table on different sides of the faults. Because saturated sediments are generally higher in velocity than the same unsaturated sediments, this abrupt change in velocity is often indicative of offsets in the ground-water table. Seismic imaging elsewhere in California has shown that water-saturated sediments typically have P-wave velocities of 1500 m/s or greater (Catchings et al, 1999; Gandhok et al., 1999) in our tomographic velocity models. As discussed in the section on seismic velocities, abrupt changes in the depths to 1500 m/s velocity contour along the SCSI-HR transect can be directly correlated with most faults mapped at the surface or imaged in the subsurface (Fig. 24). However, because the SCSI-HR transect trends along the actively flowing Los Gatos Creek and along recharge ponds, recharge of the ground-water table may be aided by water flowing over the fault zones at the surface, making the faults be less effective barriers than at other locations more distant from the flowing creek.

Earthquake hypocenters beneath the Santa Clara Valley demonstrate that there are faults beneath the valley at depths between about 1 and 25 km (Figs. 26d, 27, and 28). However, on the basis of seismicity data, it is not known if the alluvial-covered faults extend to the near surface (< 1 km depth). Our seismic images indicate that a number of high-angle (75-90 degrees) faults extend from at least 600 m to the near surface (upper 5 m). We analyzed earthquake focal mechanisms (Fig. 28) from a subset of earthquakes recorded on at least 25 stations in the valley since 1967. We selected northwest-trending fault planes of the focal mechanisms because most known faults in the region trend northwestward. The focal mechanisms show that the average dip of the fault planes for earthquakes within 3 km of the SCSI profile varies from about 60 degrees at 15+ km depth to nearly 85 degrees at 1 km depth. Although there were few earthquakes with hypocenters above 2 km depth during that time, the focal mechanisms for those earthquakes show the likely causative (NW) fault planes to be

nearly vertical. The focal-mechanism-determined dips of shallow faults are consistent with fault dips observed on our seismic reflection images in the upper 600 m, suggesting that our imaged faults are likely near-surface extensions of faults that generated the deeper (1-25 km) earthquakes.

The lateral extents of the imaged fault zones are unknown because our seismic images illuminate only a single 2-D transect. However, if the faults have been Holocene active, as our data indicates, those faults would likely offset stream channels within the foothills of the Santa Cruz Mountains and within the western Santa Clara Valley. We projected some of our imaged faults northwestward, parallel to the Santa Cruz Mountains, to see if such projections would align with bends in the natural stream channels (Fig. 29). Many of the imaged faults do align with bends in the stream channels, suggesting that such faults are possible and Holocene active. Furthermore, the inferred New Cascade Fault (Hanson et al. 2004), which was inferred on the basis of ground-water modeling, also projects along similar bends in the natural drainages (Fig. 29). Many of these faults project southward to other mapped faults exposed in the hills, suggesting that many of these faults may be at least 30 km long. Another indicator of the probable length of these faults is the lateral extent of earthquake epicenters. Earthquakes recorded since 1967 indicate that faults in the Santa Clara Valley may extend from the southern Santa Clara Valley to at least the central part of the SF Peninsula, but additional sub parallel seismic transects are needed to delineate the lateral extent of the fault zones beneath the Santa Clara Valley alluvium. The lengths of the fault zones are important because they relate to the maximum-magnitude earthquake that can be expected on faults beneath the Santa Clara Valley.

Ground Water Aquifer and the Effects of Faults

The combined SCSI-HR seismic velocity and reflection data provide constraints on lateral variations in the thickness of the ground-water aquifer system along Los Gatos Creek between Lexington Reservoir and the City of Campbell. Along the SCSI-HR transect, minimum depths of ground-water table, as inferred from the 1500 m/s velocity contour, range from about 5 m to about 40 m (Fig. 20). The largest apparent variations in depth to the ground-water table occur in areas near mapped and/or seismically imaged faults, suggesting that the fault zones affect ground-water flow in the Santa Clara Valley. The maximum depth of the ground-water aquifer system can be inferred on the basis of the thickness of Quaternary deposits as outlined in yellow on the SCSI-HR seismic images (Fig. 21) and SCSI-LR images (Fig. 26; Catchings et al., 2006). Although older consolidated rocks, such as the underlying Miocene sediments and Franciscan rocks, may contain water, they are unlikely to be a major part of the ground-water aquifer system because of their low permabilities (CDWR, 1967). Along the SCSI-HR seismic transect, the lateral variations in the contact between Quaternary and Miocene sediments can be inferred on the basis of wells along the SCSI transects (Stanley et al., 2002; Newhouse et al., 2004) and reflectors on the SCSI-HR reflection images (Fig. 21). Within about 1 km of Vasona Reservoir, lithologic logs indicate as the Quaternary-Miocene (Q-M) contact varies between 15 and 55 m, and about 1 km farther to the northeast, the Q-M contact is interpreted to be about 120 m deep (Stanley et al., 2002). When plotted on unmigrated SCSI-HR reflection images, reflectors correlated with the interpreted Q-M contact (Fig. 21). A third well, referred to as the McGlincey well (Newhouse et al., 2004), was drilled by the USGS near the northeast end of the SCSI-HR transect (Fig. 21). The base of the ground-water aquifer and the interpreted Q-M contact are located at about 240 m below the ground surface at the McGlincey well site (Fig. 21). Although the SCSI-HR and the McGlincey well were geographically separated by about 300 m and the SCSI-HR image is not particularly high in quality along that part of the profile, reflections from about 240 m depth appear to correlate with the Q-M contact. Similarly, a strong reflector is observed at that depth on the SCDI-LR reflection image (Fig. 24d). Southwest of Vasona Reservoir, the Q-M contact can be traced

toward the Santa Cruz Mountains at depths ranging from about 10 to 50 m below the surface along the SCSI-HR transect, except locally where the Q-M (or the Quaternary-Tertiary – Q-T) deepens northeast of the Berrocal fault zone (Los Gatos High School) and near Roberts Road (Fig. 21). Within the Santa Cruz Mountains, both the reflectivity pattern and relatively shallow depths to high-velocity rocks indicate that the ground-water table is relatively shallow (10-20 m) along the Los Gatos Creek trail.

Variations in the 1500 m/s velocity contour across known and imaged fault zones suggest that many of the faults in the western Santa Clara Valley affect ground water flow. Because the some of the fault zones trend northwest to southeast and appear to be ground-water barriers, the preferred direction of ground-water flow may not be southwest to northeast in parts of the valley. Instead, the preferred direction of ground-water flow may be parallel to the faults (likely northwest or southeast). Such variations in ground-water flow could cause difficulty in recovering recharged water, if the flow direction is not toward the deepest part of the ground-water basin and depending on the alignments of production wells. Hanson et al. (2004) infer one such fault (New Cascade Fault) that acts as a ground-water barrier, limiting ground-water flow to the northeast. However, our seismic images suggest several faults northeast and southwest of the New Cascade fault that appear to offset Quaternary sediments and, therefore, may be ground-water barriers. A better understanding of the 3-D variation in the aquifers and fault zones is needed to assess the effect of faults on ground-water flow within the Santa Clara Valley.

During a large-magnitude earthquake, movement on faults underlying the Santa Clara Valley may negatively impact ground-water flow by vertically displacing the aquifer across the fault zones. Wells placed on the southwest side of the fault zones may mitigate the effect of vertically offset aquifers, but the fault zone geometry must be determined at the depth of the aquifer. Similarly, vertical or horizontal offsets on faults during earthquakes may hamper ground-water recovery if transport pipelines (aqueducts) are severed across the faults. A more complete understanding of the locations, orientations, and maximum slip of active faults within the Santa Clara Valley may allow for mitigation efforts before future damaging earthquakes. Such planning was implemented along the Alaska oil pipeline where it crossed four major fault zones identified from scientific investigations conducted in the 1970's. During the November 3, 2002 M. 7.9 Denali earthquake (Eberhart-Phillips et al., 2003), nearly 4 m of horizontal and 0.75 m of vertical offset occurred across the Denali fault, but because of special engineering at the pre-determined fault zones, there was no disruptive damage to the pipeline (Cluff and Slemmons, 2002). Similar engineering could be implemented across the Santa Clara Valley faults if their locations are known.

Acknowledgements

The Santa Clara Valley Water District (SCVWD) and the USGS High-Resolution Seismic Imaging Group (HRSIG) in Menlo Park provided funding for SCSI data acquisition, and funding for data processing, interpretation, and report preparation was provided by the HRSIG and the U.S. Geological Survey's (USGS) Earthquake Hazards Program. We thank numerous individuals and organizations, including the SCVWD, the City of Los Gatos, City of Campbell, Open Space District, Los Gatos High School, Del Mar High School, and the San Jose Water Company, who provided permits and access to their properties. We thank Samuel V. Gudino, Samuel R. Gudino, Silvia Gudino, Shawn Hanson, Laura Kiger, and Jose Rodriguez, who assisted in data acquisition. We thank John Hamilton, Laura Kiger and Andy Morita for providing survey data. Thanks to Kelly Grijavla, who assisted in preparation of this report. Reviews by Tom Brocher and Randy Hanson are greatly appreciated.

References

Advanced National Seismic System (ANSS) Catalog (2004). anss@quake.geo.berkeley.edu

Aki, K., and W.H.K. Lee (1976). Determination of three-dimensional velocity anomalies under a seismic array using P-arrival times from location earthquakes. A homogenous initial model, J. Geophys. Res. 81, 4381-4399.

Bortugno, E.J., McJunkin, R.D., and Wagner, D.L. (1991). Map showing recency of faulting, San Francisco-San Jose quadrangle, 1:250,000: Department of Conservation, Division of Mines and Geology Regional Geologic Map Series, Map 5A, Sheet 5.

Brocher, T. M., A. L. Ruebel, and E. E. Brabb (1997). Compilation of 59 sonic and density logs from 51 oil test wells in the San Francisco Bay area, California. U.S. Geological Survey Open-File Report 97-987 75 pp.

Brouwer, J., and K. Helbig (1998). Shallow high-resolution reflection seismics. In: Helbig, K., Treitel, S. (Eds.), Handbook of Geophysical Exploration: Seismic Exploration, Vol. 19, Elsevier, New York, New York, 391 pp.

California Department of Water Resources (CDWR) (1967). Evaluation of Ground Water Resources, South Bay, Appendix A: Geology: Bulletin 118-1, 153 p.

California Department of Water Resources (CDWR) (1975). Evaluation of groundwater resources, south San Francisco Bay, Volume III, northern Santa Clara County area: Bulletin No. 118-1, various pagination.

Carmichael, R. S. (1989) Practical Handbook of Physical Properties of Rocks and Minerals, CRC Press, Boca Raton, Ann Arbor, Boston.

Catchings, R. D., E. Horta, M. R. Goldman, M. J. Rymer, and T. R. Burdette (1998). High resolution seismic images for environmental and earthquake hazards assessment at the Ray Chem site, Menlo Park, California: U.S. Geological Survey Open-File Report 98-146, 37 pp.

Catchings, R. D. (1999). Regional Vp, Vs, Vp/Vs, and Poisson's ratios across earthquake source zones from Memphis, Tennessee to St. Louis, Missouri. Bull. Seism. Soc. Am, 89, 1591-1605.

Catchings, R. D., G. Gandhok, M. R. Goldman, E. Horta, M. J. Rymer, P. Martin, and A. Christensen (1999). Subsurface, high-resolution, seismic images from Cherry Valley, San Bernardino County, California: Implications for Water Resources and Earthquake Hazards, U.S. Geological Survey Open-File Report 99-26, 57 pp.

Catchings, R. D., M. R. Goldman, G. Gandhok, E. Horta, M. J. Rymer, P. Martin, and A. Christensen (1999). Structure, velocities, and faulting relationships beneath San Gorgonio Pass, California: Implications for water resources and earthquake hazards, U.S. Geological Survey Open-File Report 99-568, 53 pp.

Catchings, R. D., M. R Goldman,., G Gandhok,., M. J Rymer,., and D. H. Underwood (2000). Seismic imaging evidence for faulting across the northwestern projection of the Silver Creek Fault, San Jose, California: U.S. Geological Survey Open-File Report 00-125, 29 p.

Catchings, R. D., M. J. Rymer, M. R. Goldman, J. A Hole, R. Huggins, and C. Lippus (2002). High-resolution seismic velocities and shallow structure of the San Andreas fault zone at Middle Mountain, Parkfield, California, Bull. Seis. Soc. Am, 92, 2493-2503.

Catchings, R. D., M. R. Goldman, and G. Gandhok (2006), Structure and velocities of the northeastern Santa Cruz Mountains and the western Santa Clara Valley, California, from the SCSI-LR seismic survey, U.S. Geological Survey Open-File Report 2006-1014, 77 pp.

Catchings, R. D., G. Gandhok, M. R. Goldman, and D. Okaya (in press). Near-surface location, geometry, and velocities within the Santa Monica Fault zone, West Los Angeles, California, submitted to Bull. Seism. Soc. Am

Christiansen, N.I. (1982). Seismic Velocities in R.S. Carmichael ed., Handbook of Physical Properties of Rocks, v. II, CRC Press, Boca Raton.

Cluff, L. S., and D. B. Slemmons (2002). Trans Alaska pipeline design accommodations November 3, 2002 magnitude 7.9 earthquake EOS trans. AGU, 83, S72F-1329.

Dibblee, T.R., Jr. (1966). Geology of the Palo Alto quadrangle, Santa Clara and San Mateo Counties, California: California Division of Mines and Geology Map Sheet 8, scale 1:62,500.

Dietz, Lynn D., and William L. Ellsworth (1997). Aftershocks of the Loma Prieta Earthquake and their tectonic implications, in The Loma Prieta, California Earthquake of October 17, 1989: Earthquake Occurrence. Aftershocks and Postseismic Effects, U.S. Geological Survey Profess. Paper 1550-D, p. D5-D47

Dobrin, Milton B., and Carl H. Savit (1988). Introduction to Geophysical Prospecting, Fourth Edition, McGraw-Hill Book Co., San Francisco, 867 p.

Eberhart-Phillips, D. and 28 others (2003). The 2002 Denali Fault earthquake, Alaska: A large-magnitude, slip-partitioned event, Science, 300, 1113-1118.

Gandhok, G., R. D. Catchings, M. R. Goldman, E. Horta, M. J. Rymer, P. Martin, and A. Christensen (1999). High-Resolution Seismic Reflection/Refraction Imaging from Interstate 10 to Cherry Valley Boulevard, Cherry Valley, Riverside County, California: Implications for Water Resources and Earthquake Hazards, US Geological Survey Open-file Report 99-320, 52 p.

Helley, E. J., R. W. Graymer, G. A. Phelps, P. K. Showalter, and C. M. Wentworth (1994). Quaternary geology of the Santa Clara Valley, Santa Clara, Alameda, and San Mateo Counties, California: A digital database. US Geological Survey Open-File Report 94-231

Hanson, R.T., N.W. Newhouse, C.M. Wentworth, C.F. Williams, T.E. Noce, M.J. Bennett (2002). Santa Clara Valley Water District Multi-aquifer monitoring site, Coyote Creek Outdoor Classroom, San Jose, California: U.S. Geological Survey Open-File Report 2002-369, 4 p.

Hanson, R.T., Zhen Li, and C.C. Faunt (2004). Documentation of the Santa Clara Valley Regional ground-water/surface-water flow model, Santa clara County, California, U.S. Open-File Report 2004-5231, 85 p

Hanson, R.T., Zhen Li, and C.C. Faunt (2004)., Documentation of the Santa Clara Valley regional ground-water/surface-water flow model, Santa Clara County, California: Scientific Investigations Report SIR2004-5231 , 75 p. [http://pubs.water.usgs.gov/sir2004-5231/].

Hole, J. A. (1992). Nonlinear high-resolution three-dimensional seismic traveltime tomography. J. Geophys. Res. 97, 6553–6562.

Hole, J. A., R. D. Catchings, K. C. St. Clair, M. J. Rymer, D. A. Okaya, and B. J. Carney (2001). Steep-dip seismic imaging of the shallow San Andreas fault near Parkfield, Science, 294, 1513-1515

McLaughlin, R. J., J. C. Clark, E.E. Brabb, E.J. Helley, and C.J. Colon (2001). Geologic maps and structure sections of the southwestern Santa Clara Valley and southern Santa Cruz Mountains, Santa Clara and Santa Cruz Counties, California, U.S. Geol. Surv. Misc. Field Studies Map MF-2373

Mooney, W. D., and J. H. Luetgert (1982). A seismic refraction study of the Santa Clara Valley and southern Santa Cruz Mountains, west-central California, Bull. Seism. Soc. Am. 72, 901-909.

Newhouse, M.W., Hanson, R.T., Wentworth, C.M., Everett, R., Williams, C.F., Tinsley J., Noce, T.E., and Carkin, B.A. (2004). Geologic, water-chemistry, and hydrologic data from multiple-well monitoring sites and selected water-supply wells in the Santa Clara Valley, California, 1999-2003: U.S. Geological Survey Scientific Investigations Report SIR2004-5250, 134 p. [http://pubs.water.usgs.gov/sir2004-5250/]

Nur, A. (1982). Notes on wave propagation in porous rocks, Stanford Rock Physics Progress Report, January 1982, vol. 13, 121 pp. Stanford University, Stanford, CA,

Poland, J.F. (1971). Land subsidence in the Santa Clara Valley, Alameda, San Mateo, and Santa Clara Counties, California: U.S. Geological Survey Open-File Report, Map Scale 1:125,000

Poland, J.F., and Ireland R.L. (1988). Land Subsidence in the Santa Clara Valley, California, as of 1982: U.S. Geological Survey Professional Paper 497-F, 61 p.

Schon, J.H. (1996). Physical Properties of Rocks. Fundamentals and principals of petrophysics, in Handbook of Geophysical Exploration V. 18 (K. Helbig and S. Treitel, eds.), Pergamon Press, Elsevier Science, Inc. New York, New York, 583 pp.

Simpson, R. (2004). Profiles Using Double Difference Earthquakes Santa Clara Valley Blind Thrusts: U.S. Geological Survey [http://ehzweb-menlo.wr.usgs.gov/DD_Eq_Plots/Eqs_scvbt/].

Stanley, R.G., Jachens, R.C., Lillis, P.G., McLaughlin, R.J., Kvenvolden, K.A., Hostettler, F.D., McDougall, K.A., and Magoon, L.B. (2002). Subsurface and Petroleum Geology of the Southwestern Santa Clara Valley ("Silicon Valley"), California: U.S. Geological Survey Professional Paper 1663, 55 p.

Wagner, D.L., K.J. Bortugno, and R.D. McJunkin (1990). Geologic map of the San Francisco-San Jose quadrangle: California Department of Conservation, Division of Mines and Geology, Regional Geologic Map Series, Map No. 5A, 5 sheets.

Wentworth C.M. (1997). General distribution of geologic materials in the San Francisco Bay region, California: a digital map database: U.S. Geological Survey Open File Report 97-744.

United States Census Bureau (2003). State and county QuickFacts, Santa Clara County, California [http://quickfacts.census.gov/qfd/states/06/06085.html].

Zoback, M.L., J.A. Olson, and R.C. Jachens (1995) Seismicity and basement structure beneath the south San Francisco Bay, California, in Sangines, E.M., Anderson, D.W., and Busing, A.V., eds., Recent geologic studies in the San Francisco Bay area: Society of Economic Paleontologists and Mineralogists, Pacific Section Special Publication 76, p. 31-46

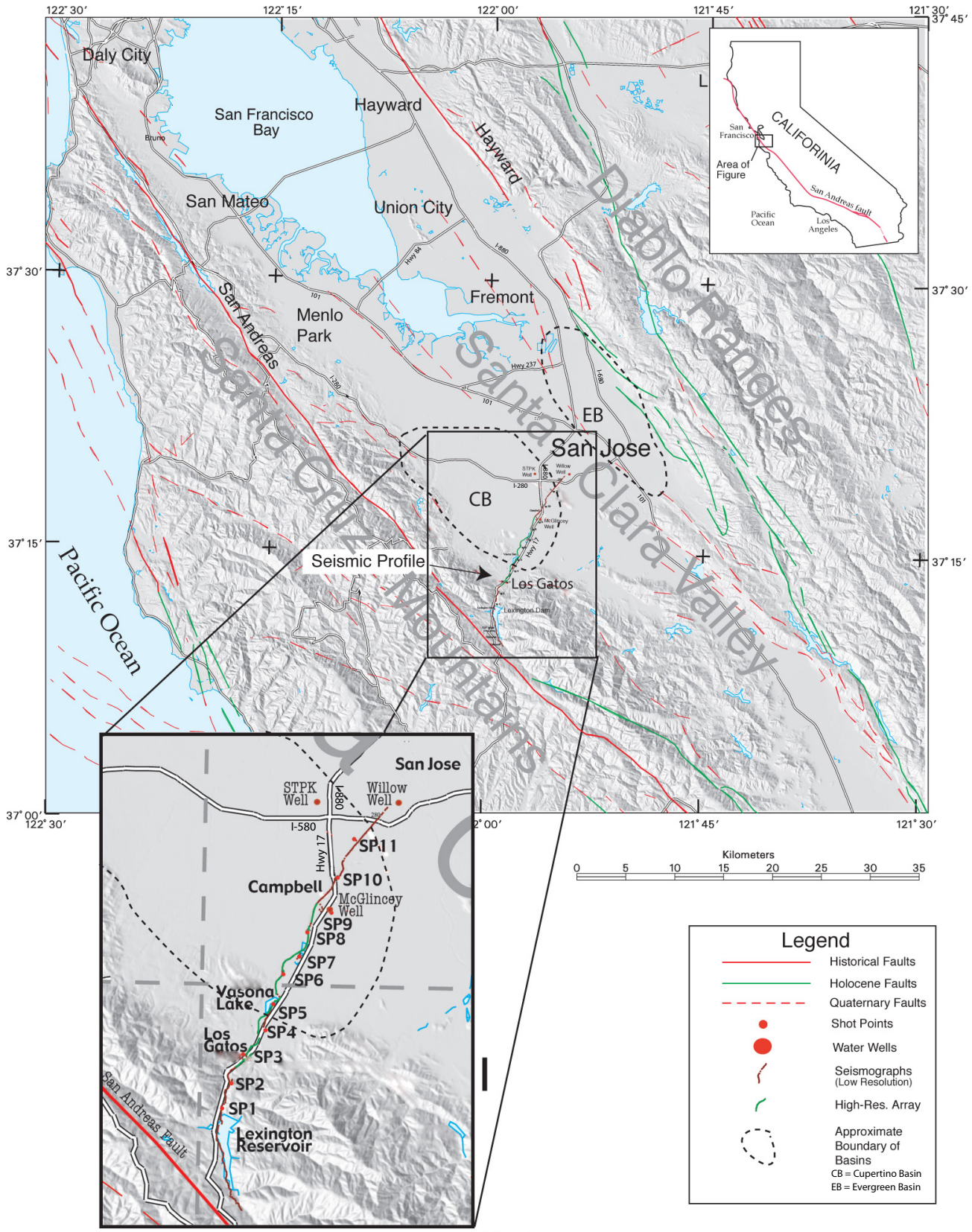

Figure 1. Location map of the southern San Francisco Bay region showing major geographic and geological features, freeways, selected cities, the SCSI-HR and SCSI-LR seismic transect (in green and red, respectively), and mapped or inferred faults from Bortugno et al. (1991). The dashed black lines outline the approximate are of the major basins in the Santa Clara Valley, the Cupertino Basin (CB) and the Evergreen Basin (EB). In the inset, SP# refers to shot points along the SCSI-LR seismic transect. The locations of wells recently drilled by the USGS are also shown.

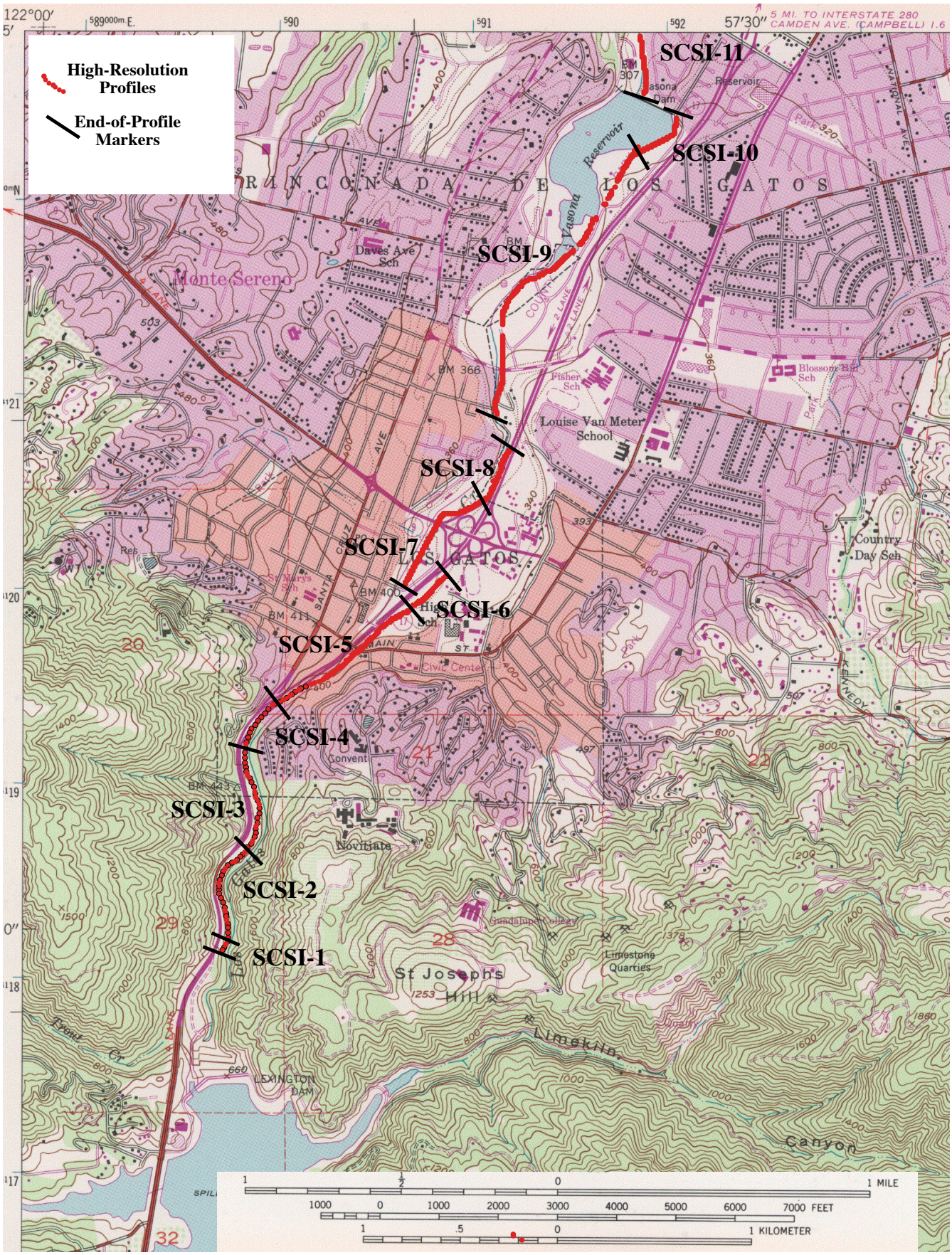

Figure 2. (a). The northern part of the USGS 7.5-minute Los Gatos quadrangle map, with the location of the southern part of SCSI-HR transect (red dots). Geophones and shots were spaced at 5-m increments along the transect. The transect was segmented into approximately 14 near-linear profiles for ease of acquisition and processing. Individual profiles are labeled SCSI-#, and their endpoints are shown by the black lines.

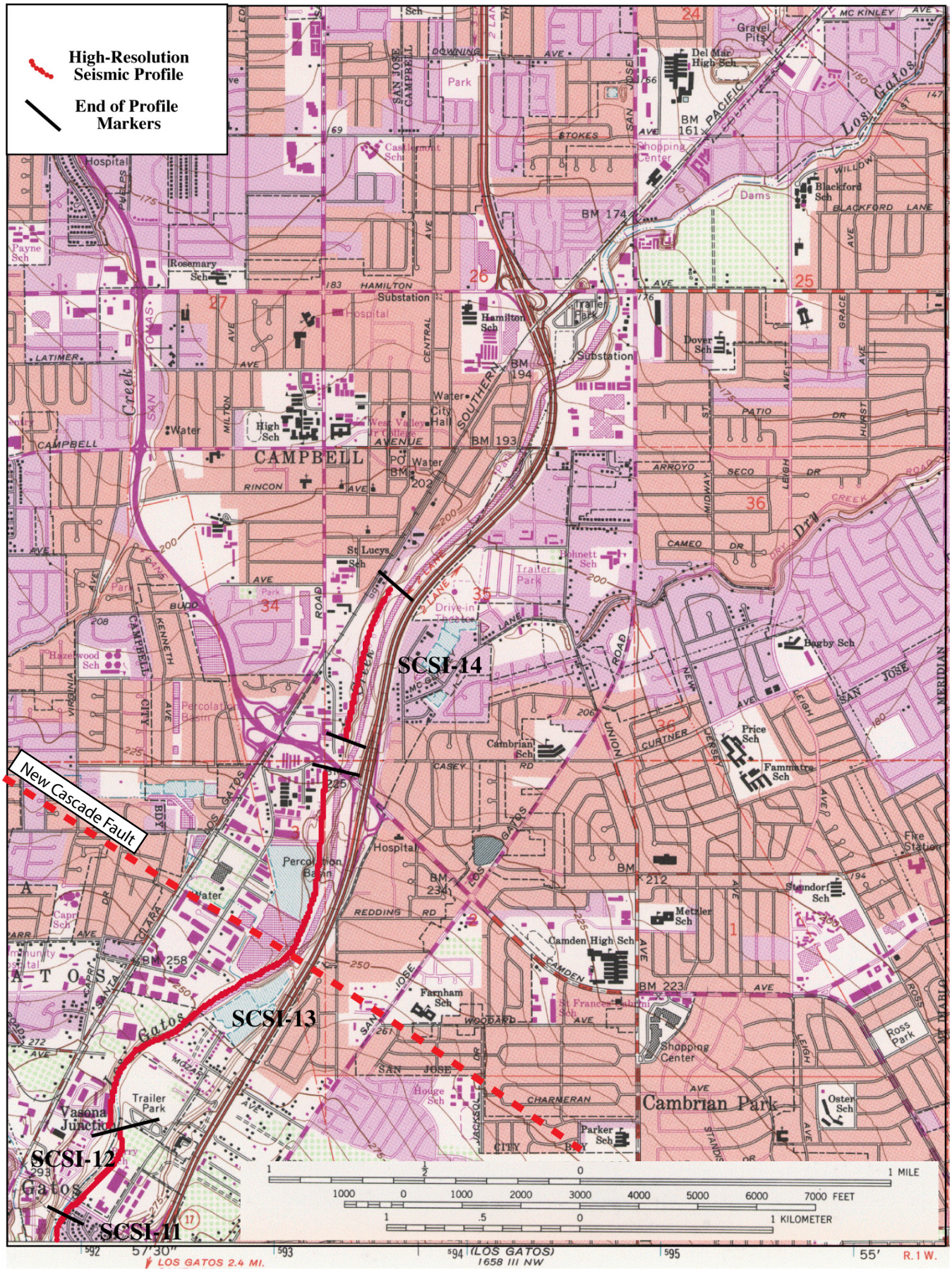

Figure 2. (b) The southern part of the USGS 7.5-minute San Jose West Quadrangle map, showing the northern part of the SCSI-HR transect and plotted as in figure 2a. The location of the New Cascade Fault inferred by Hanson et al. (2004) is shown along profile SCSI-13.

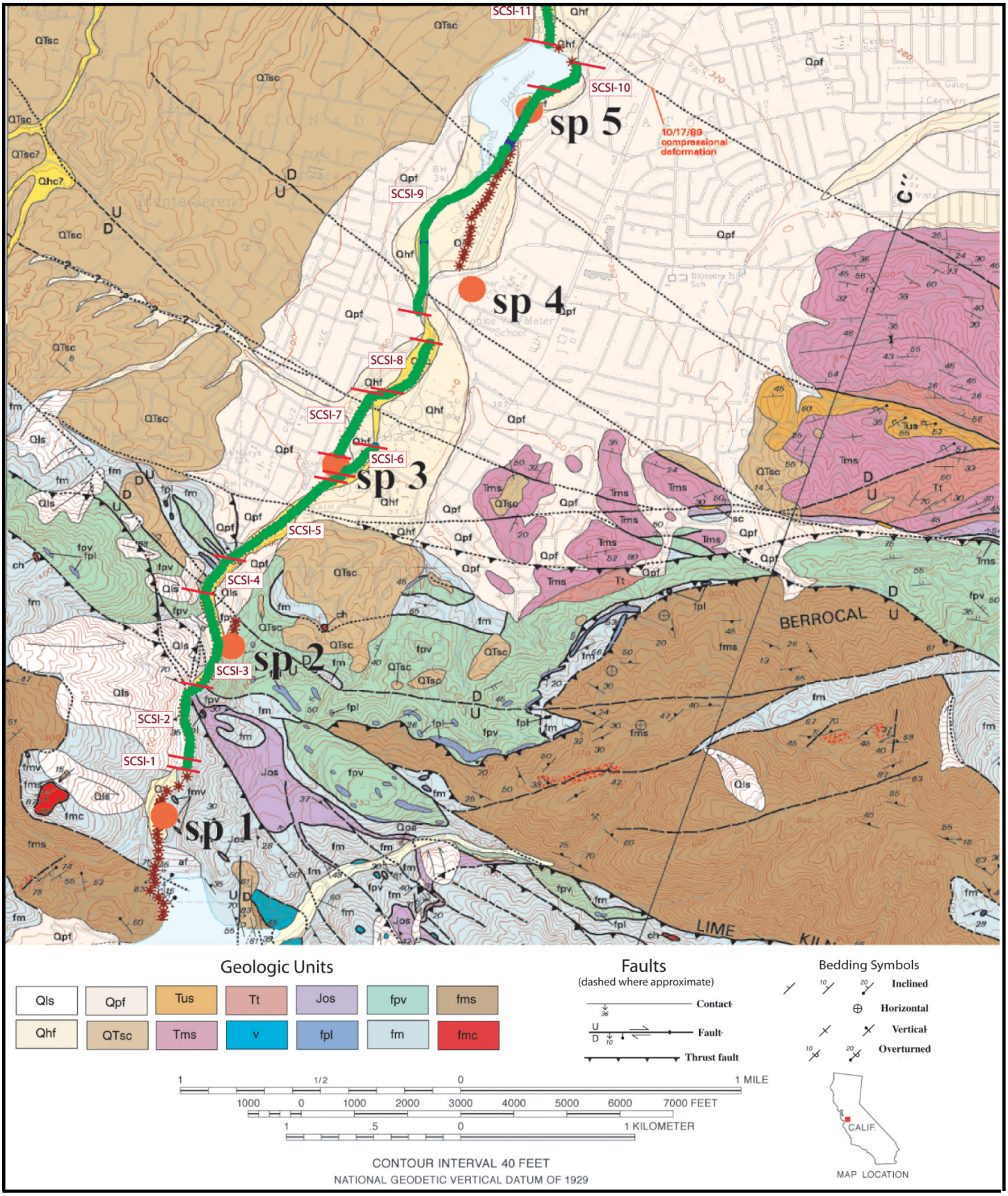

Figure 3. (a) Geologic map along the southern part of the SCSI transect (from McLaughlin et al., 2001). The southern part of the SCSI-HR transect is shown in green, and the locations of seismographs used in the SCSI-LR transect are shown in brown. Where the two transects coincide, only the SCSI-HR transect is shown. The orange dots labeled "SP #" refer to large shot points used along the SCSI-LR transect. The shot orange lines show the end points of individual SCSI profiles.

Geologic Map Units For Figure 3a

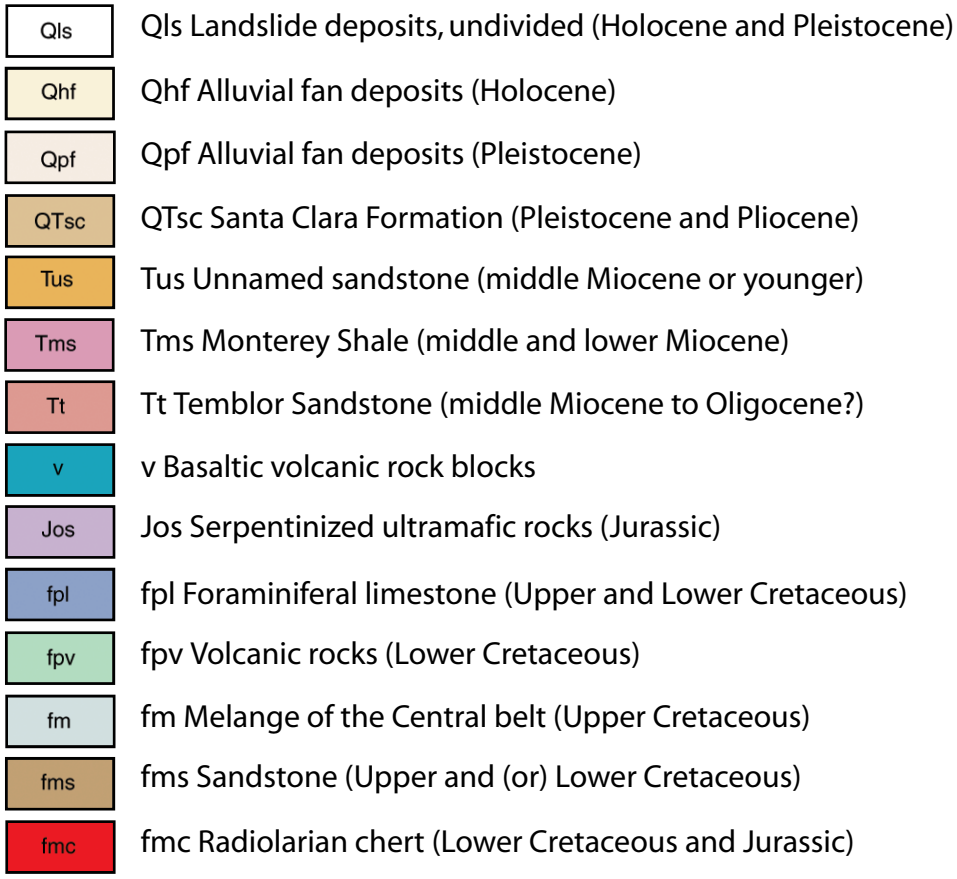

Figure 3. (b) Abbreviated descriptions of the geologic units shown in figure 3a.

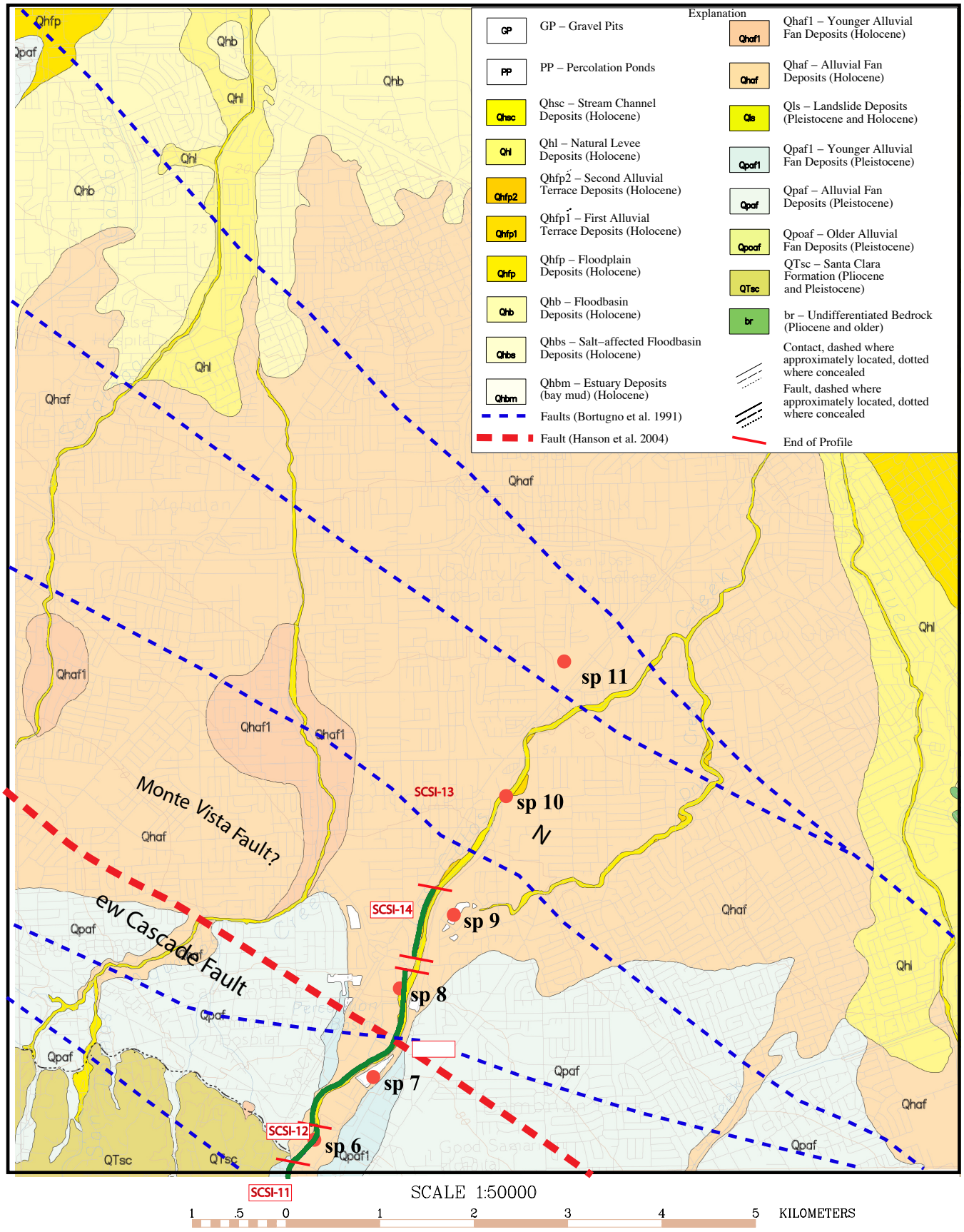

Figure 4. Geologic map along the northern part of the SCSI transects (from Helley et al. 1994). Green asterisks show the location of shot points and geophones of the SCSI-HR transect. Red dots labeled "sp#" refer to shot points used for the SCSI-LR transect. Individual profiles are labeled SCSI-# and are oulined by the short orange lines. The location of the New Cascade Fault (red dashed line) inferred by Hanson et al. (2004) is shown along profile SCSI-13. Other faults inferred by Bortugno et al. (1991) are show as blud dashed lines.

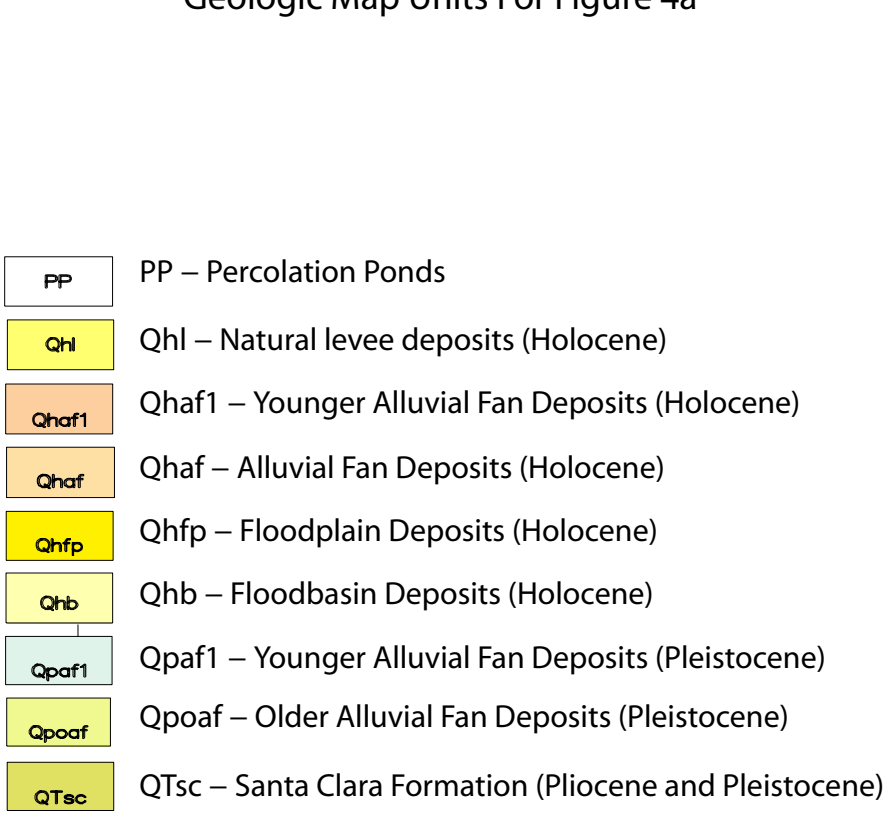

Figure 4. (b) Abbreviated descriptions of the geologic units shown in figure 4a.

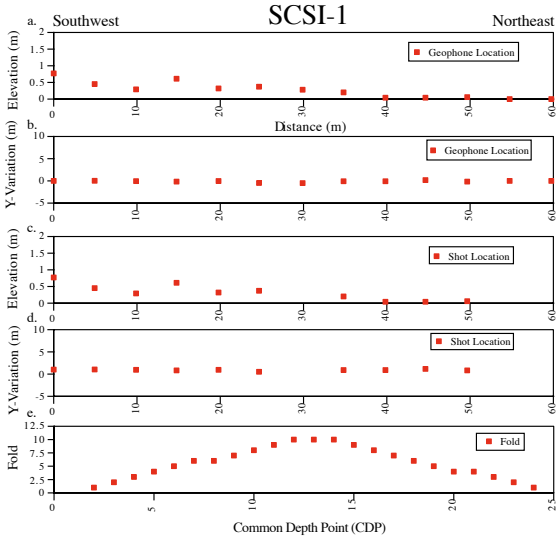

Fig. 5

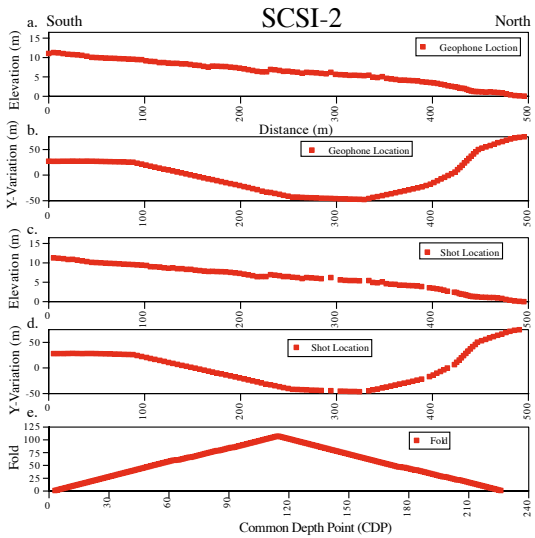

Fig. 6

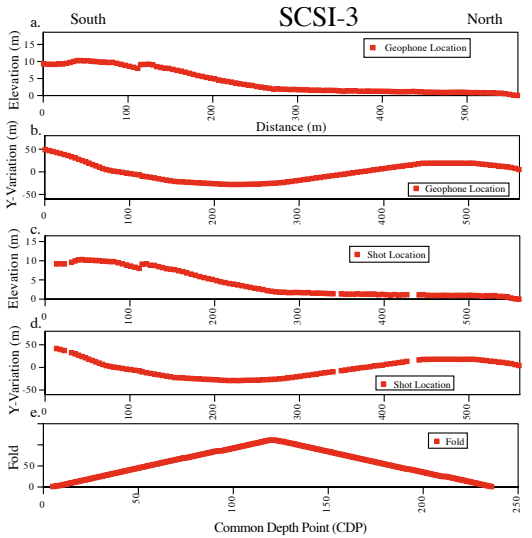

Fig. 7

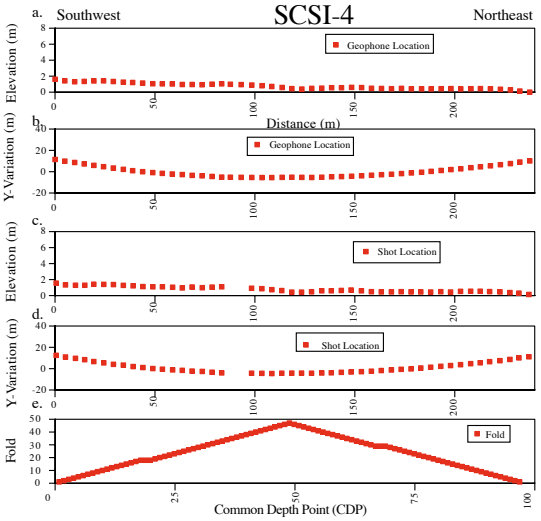

Fig. 8

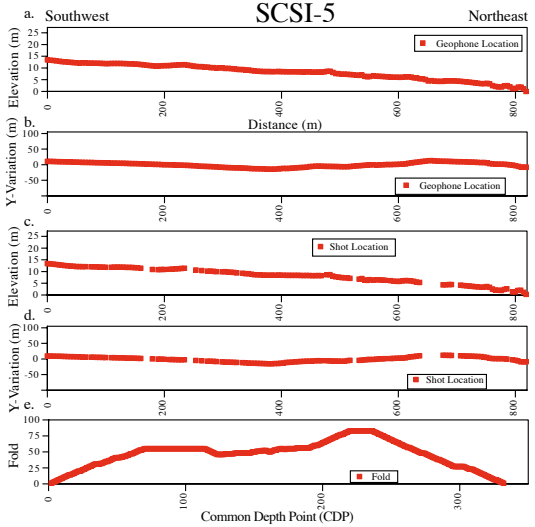

Fig. 9

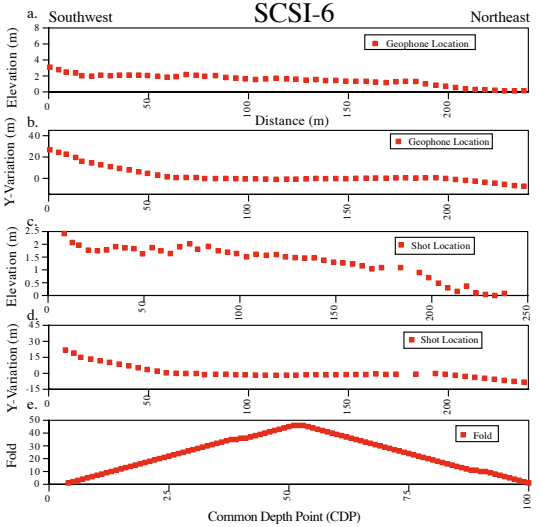

Fig. 10

Figures 5-10. Geometry of the SCSI-1 through SCSI 6 profiles. Variation in (a) geophone elevation, (b) geophone-array linearity, (c) shot-point elevation, (d) shot-point-array linearity, and (e) fold along the SCSI-1 profile. Elevation is relative to the topographically lowest geophone or shot point. Geophone and shot-point array "Y" variations (linearity) are relative to a line connecting the endpoints of the arrays. Vertical exaggeration on the elevation plots is 12:1, and horizontal exaggeration on the linearity plots is 0.5:1.

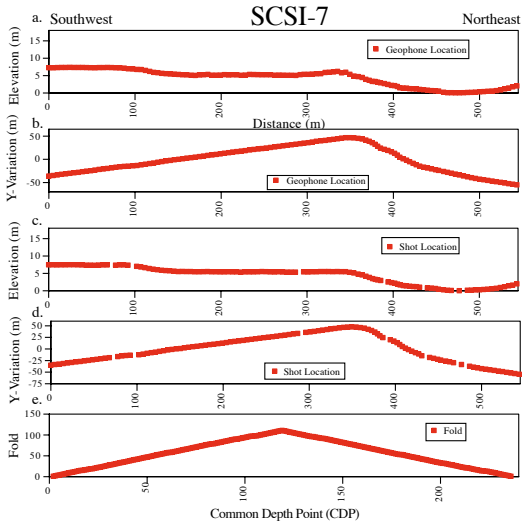

Fig. 11

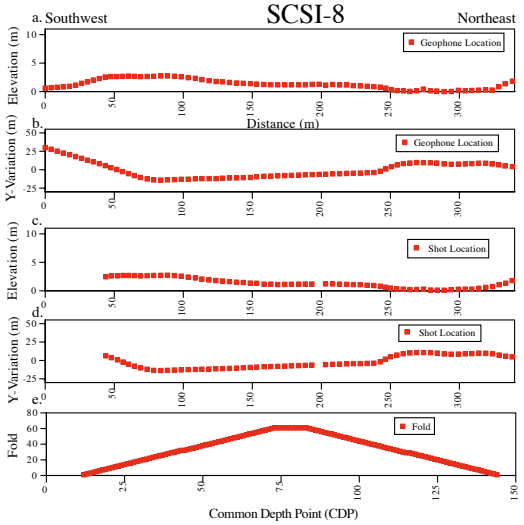

Fig. 12

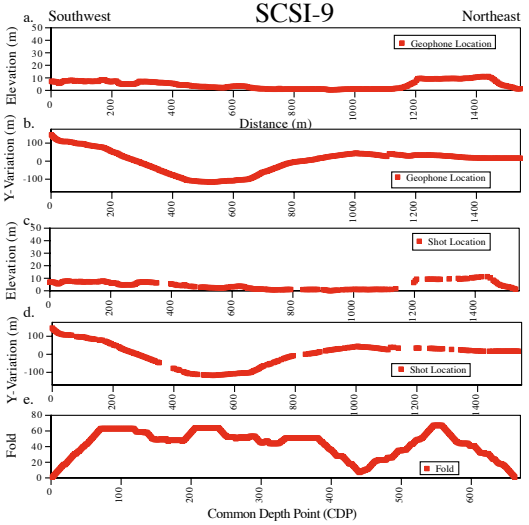

Fig. 13

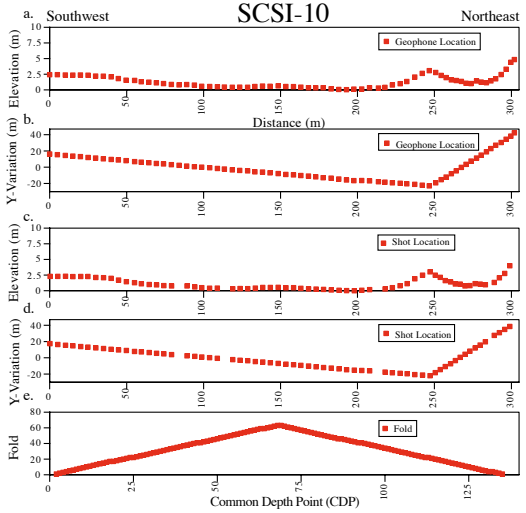

Fig. 14

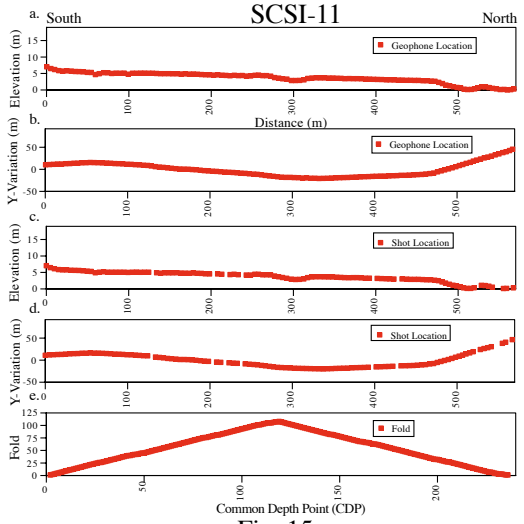

Fig. 15

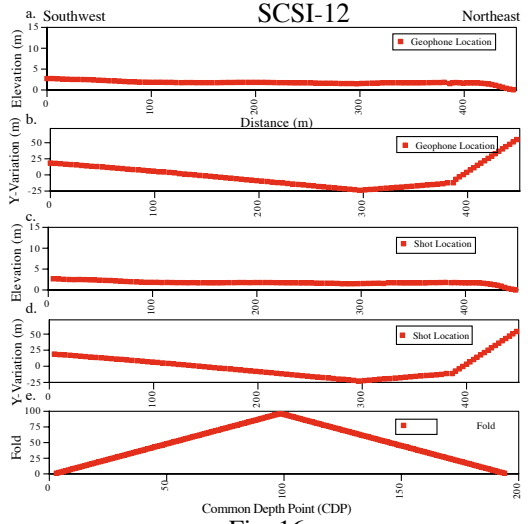

Fig. 16

Figures 11-16. Geometry of the SCSI-7 through SCSI 12 profiles. Variation in (a) geophone elevation, (b) geophone-array linearity, (c) shot-point elevation, (d) shot-point-array linearity, and (e) fold along the SCSI-1 profile. Elevation is relative to the topographically lowest geophone or shot point. Geophone and shot-point array "Y" variations (linearity) are relative to a line connecting the endpoints of the arrays. Vertical exaggeration on the elevation plots is 12:1, and horizontal exaggeration on the linearity plots is 0.5:1. For SCSI-9, the horizontal exaggeration on the linearity plots is 0.6:1. For SCSI-12, the horizontal exaggeration on the linearity plots is 0.6:1.

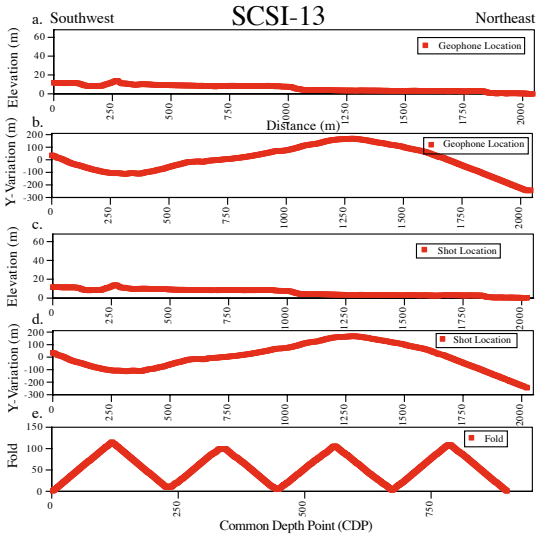

Fig. 17

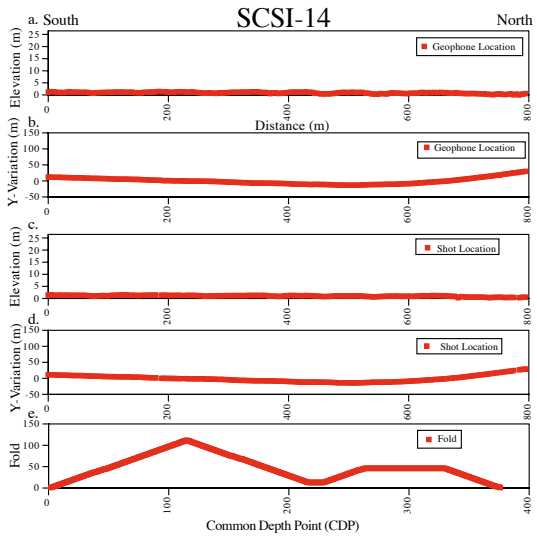

Fig.18

Figures 17-18. Geometry of the SCSI-13 through SCSI 14 profiles. Variation in (a) geophone elevation, (b) geophone-array linearity, (c) shot-point elevation, (d) shot-point-array linearity, and (e) fold along the SCSI-1 profile. Elevation is relative to the topographically lowest geophone or shot point. Geophone and shot-point array "Y" variations (linearity) are relative to a line connecting the endpoints of the arrays. Vertical exaggeration on the elevation plots is 12:1, and horizontal exaggeration on the linearity plots is 0.5:1.

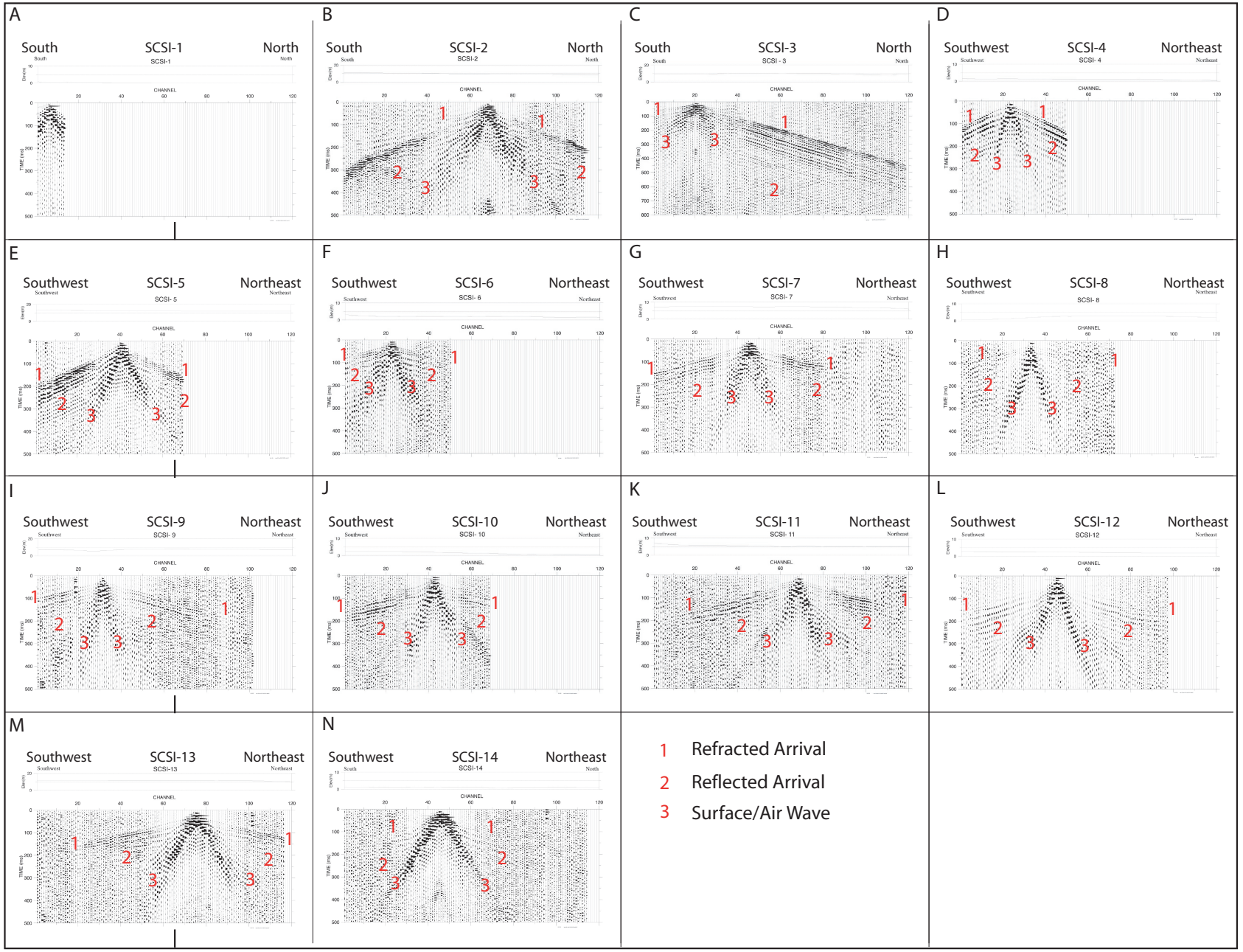

Figure 19. Representative shot gathers for profiles SCSI-1 through SCSI-14 (figures a-n, respectively). Bandpass filtering and AGC have been added. Blank traces indicate channels not used along specific profiles, generally along short profiles. The numbers on the shot gathers refer to various arrivals: "1" refers to refracted arrivals, "2" refers to reflections, and "3" refer to surface and air waves.

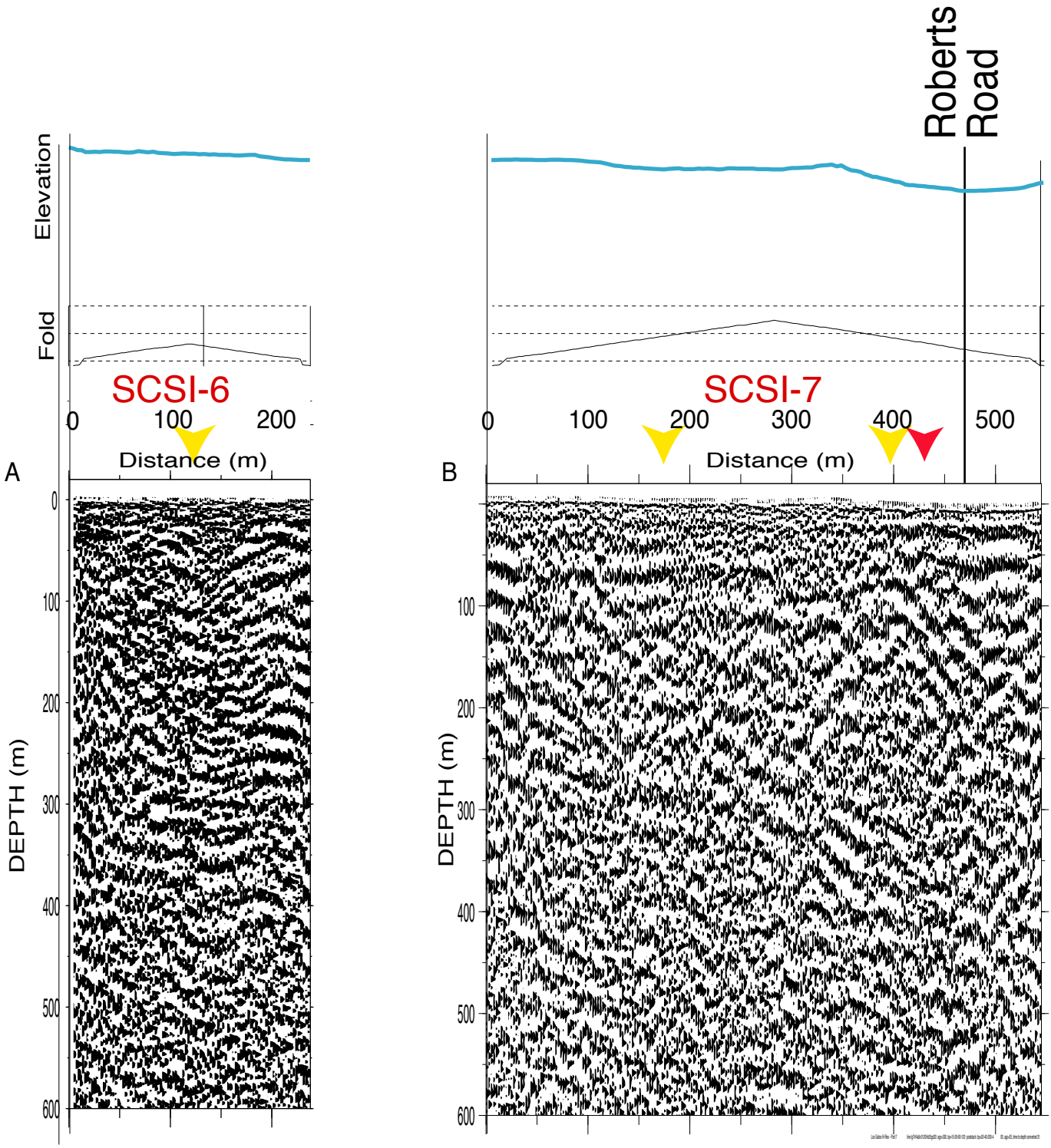

Figure 25. Seismic reflection images along profiles SCSI-6 and SCSI-7 from figure 21. The two profiles have been separated, but in 2-D cross-sectional view, the two profiles overlap.

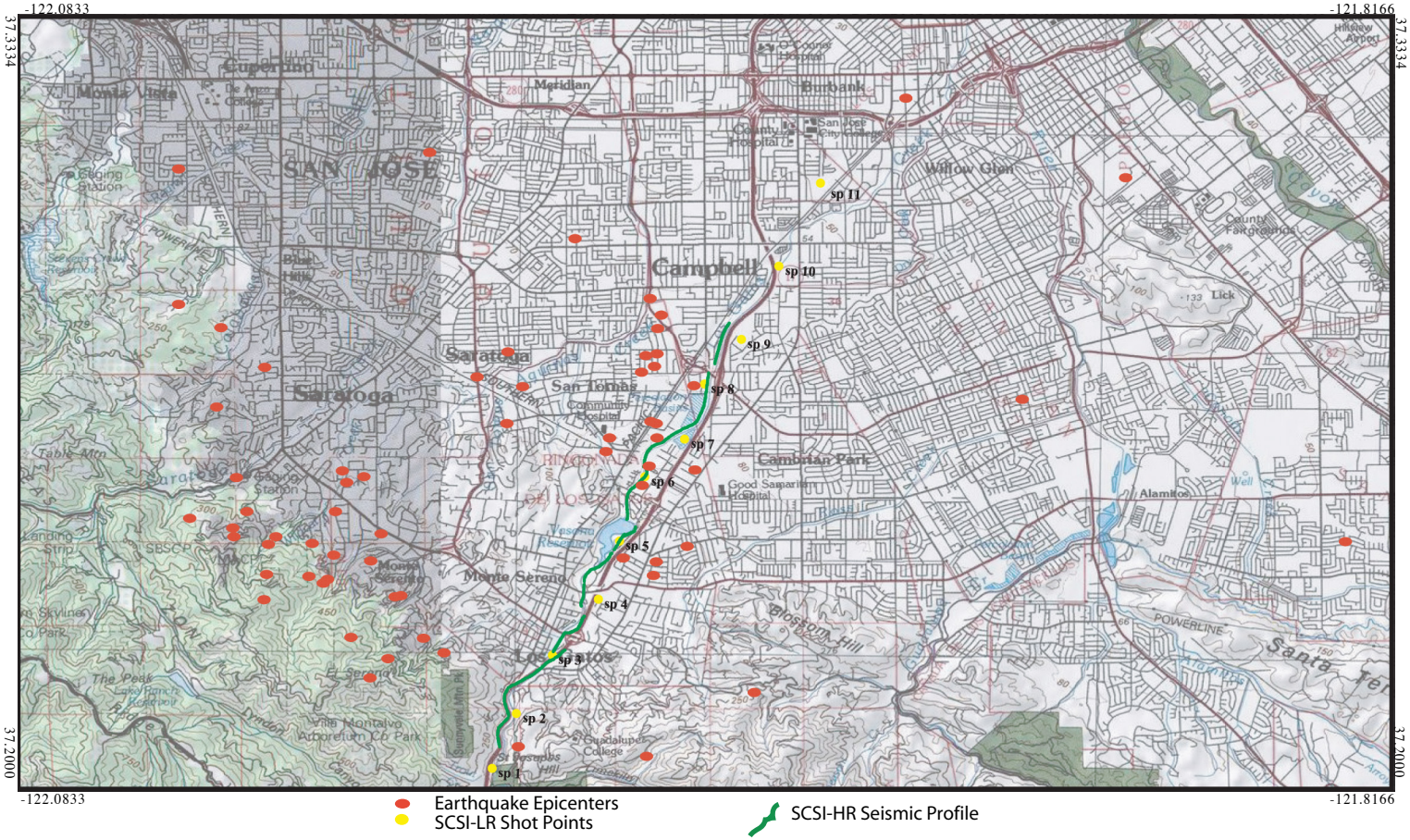

Figure 27. Topographic map of the southwestern Santa Clara Valley with the locations of the SCSI-HR seismic transect (green), shot points for the SCSI-LR transect (yellow) and earthquake epicenters for a subset of well-recorded earthquakes in the area since 1967.

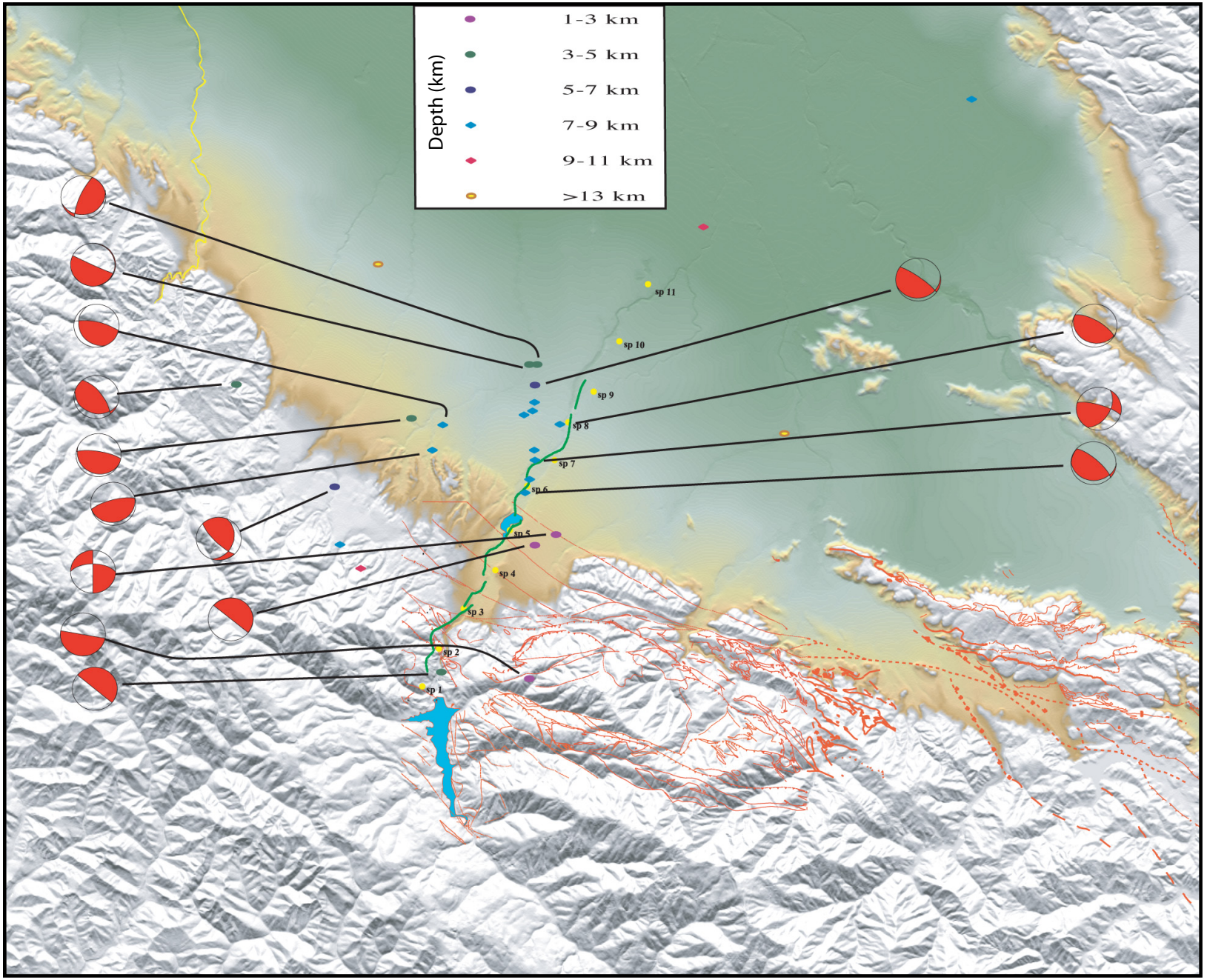

Figure 28. Shaded relief map of the study area with the locations the SCSI transect, faults (red lines) mapped by McLaughlin et al. (2001), earthquakes within 3 km of the SCSI transect, and focal mechanisms for well-recorded earthquakes. Higher elevations are shown in white, and the lowest elevations are shown in dark green.

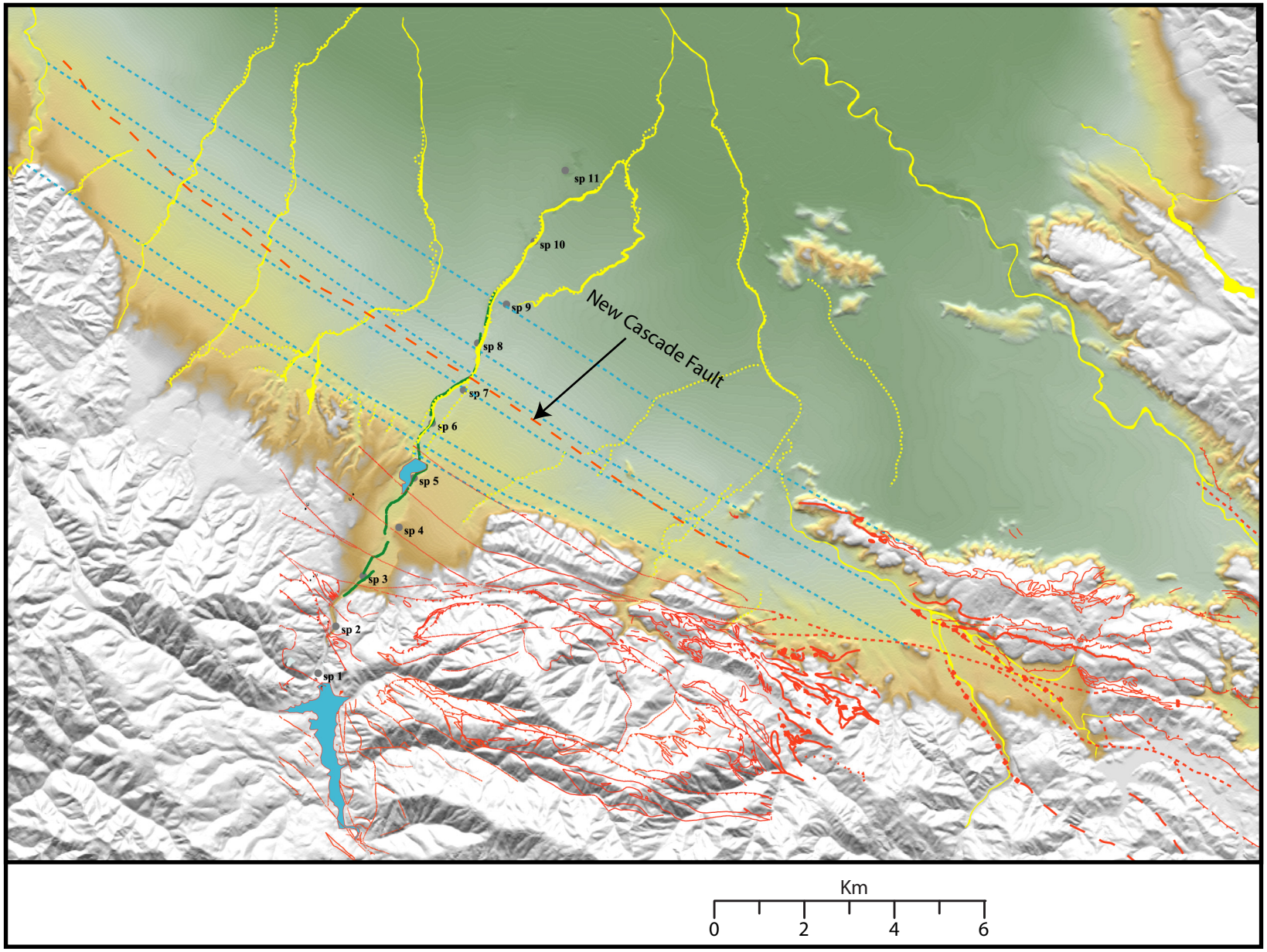

Figure 29. Shaded relief map from figure 28, with the locations of the SCSI transect, natural drainages (yellow), and mapped faults (red – from figure 28). The orange dashed line denotes the New Cascade Fault of Hanson et al. (2004). Blue lines are interpretative lineaments that connect drainage-offsets and some of the faults imaged on the SCSI-HR transect. Note that elevation variations within the valley approximately parallel the mountain range front, and mapped faults (exposed in hills) to the southeast project toward the SCSI profile.

Figures, oversized (20, 21, 22, 23, 24, and 26; links to separate files)

Figure 20. Composite of P-wave velocity images along profiles SCSI-2 through SCSI-14 of the SCSI-HR transect. Distance and depth are shown in meters, and the distance scale along the top refers to distance long each profile. Individual profiles are labeled SCSI-#. Vertical exaggeration is 4 to 1. Velocities are in meters per second. The white contour highlights the 1500 m/s velocity contour, the minimum velocity of water-saturated unconsolidated sediments. SP# refers to shot-point locations for the SCSI-LR profile. The blue arrow infers the general direction of ground-water flow. Red arrows show the locations of mapped faults from figures 3 and 4 or coincident mapped and imaged faults. Green arrows show locations of faults imaged on the SCSI reflection images (see Fig. 21), but not mapped at the surface (Figs. 3 and 4). Profiles SCSI-6 and SCSI-7 overlap in 2-D cross-sectional view (see Fig. 2a).

Figure 21. (a) Composite of unmigrated seismic reflection images of the upper 600 m along profiles SCSI-2 through SCSI-14 of the SCSI-HR transect. Distance and depth are in meters and are without vertical exaggeration. The distance scale along the top refers to distance along each profile, and distance along the bottom refers to composite distance along the SCSI-HR transect. "Meter xxxx" (bottom of figure) refers to distance along the SCSI-LR transect. SP# refers to shot-point locations along SCSI-LR transect. Elevation along the SCSI-HR transect is shown in blue. Fold along each profile is shown below the elevation profile. Red arrowheads show the locations of mapped surface faults from figures 3 and 4 or coincident mapped and imaged faults. Yellow arrowheads show the locations of faults on the SCSI-HR reflection images but not mapped at the surface. Profiles SCSI-6 and SCSI-7 overlap in 2-D cross-sectional view (see fig. 2a). The seismic data have been bandpass filtered with minimum frequencies of 35 Hz (35-70-140-280 Hz). (b) Composite image from figure 21a with interpretative Quaternary sediments (yellow), faults (yellow lines), and wells (magenta) plotted in their approximate locations. Blue lines on the wells refer to the base of the Quaternary, as interpreted from the well logs (Stanley et al., 2002 and Hansen et al., 2004). The blue numbers above the figure are interpreted faults. (c) The red and white symbols are focal mechanisms (plan view) determined from shallow-depth (upper 10 km) earthquakes along the SCSI-HR transect and plotted in the approximate epicentral locations. Hypocentral depths are listed below the focal mechanisms. Note that the northwest-oriented fault planes are nearly vertical.

Figure 22. Composite of migrated seismic reflection images of the upper 300 m along profiles SCSI-2 through SCSI-14 of the SCSI-HR transect, plotted as in figure 21. The seismic data have been bandpass filtered with minimum frequencies of 75 Hz (75-150-300-600 Hz).

Figure 23. (a) Topographic profile and landmarks along the SCSI-HR seismic profile, which was approximately coincident with the SCSI-LR profile. (b) Migrated seismic reflection image for the SCSI-LR transect (Catchings et al., 2006) where it approximately coincides with the SCSI-HR seismic transect. SP# refers to shot-point locations for the SCSI-LR profiles. Elevations (blue), locations (red numbers), fold, and landmarks along the SCSI-HR transect are shown above. Because the SCSI-LR and SCSI-HR transects were not everywhere coincident, distances and correlations between the profiles are approximate. Because elevations change from southwest to northeast, 600-m depth differs on the southwest (black line) from that on the northeast (base of plot). (c) Migrated SCSI-LR reflection image from figure 23a, with interpretative near-surface Quaternary sediments (yellow) as shown in figure 21b. Blue (Miocene sediments) and green (Franciscan?) coloring between reflections is intended to help correlate layers laterally. The yellow coloring correlates with Quaternary near-surface sediments. Well logs from figure 23 are also shown. Calculated layer resolution on the SCSI-LR image is about 125 m.

Figure 24. Comparative figures of (a) topographic profile along the SCSI-HR seimsic profile, (b) composite P-wave velocity images from figure 20, (c) composite interpretative unmigrated reflection images from figure 21b, (d) interpretative SCSI-LR migrated reflection image from figure 23b, and (e) focal mechanisms in plan view for shallow-depth earthquakes along the profile. The numbers above figure 24d indicate imaged faults on both the SCSI-HR and SCSI-LR seimsic profiles.

Figure 26. Comparative figure showing the relation between (a) the interpretative SCSI-HR migrated reflection image from figure 21b, (b) the interpretative SCSI-LR reflection image from figure 23b, (c) line drawing (solid lines) of reflectors from the SCSI-LR reflection image (fig. 23b), and (d) focal mechanisms for earthquakes along the SCSI seismic profiles in plan view. The line drawing includes interpretive (dashed) lines and coloring to highlight reflector groups. Yellow reflectors indicate Quaternary, green reflectors indicate Franciscan, and blue and white indicate Miocene sediments. Focal mechanism show high-angle dips of fault planes at relatively shallow depths beneath the SCSI transect. On figure 26c, the numbers above the figure indicate imaged faults on both the SCSI-HR and SCSI-LR seimsic profiles.

Appendixes

Appendix A

Distances and elevations along SCSI-1.
Measurements are relative to the first geophone at the south end of the line.

Geophone No.	Geo. Dist. (m)	Geo. Elev. (m)	Shot Point No.	Shot Dist (m)	Shot Elev. (m)
1	0	0.77	1	0	0.77
2	4.91	0.45	2	4.91	0.45
3	9.89	0.29	3	9.89	0.29
4	14.75	0.61	4	14.75	0.61
5	19.79	0.32	5	19.79	0.32
6	24.65	0.37	6	24.65	0.37
7	29.88	0.28			
8	34.8	0.2	8	34.8	0.2
9	39.83	0.04	9	39.83	0.04
10	44.64	0.04	10	44.64	0.04
11	49.65	0.06	11	49.65	0.06
12	54.75	0			
13	59.75	0			

Appendix B

Distances and elevations along SCSI-2.
Measurements are relative to the first geophone at the south end of the line.

Geophone No.	Geo. Dist. (m)	Geo. Elev. (m)	Shot Point No.	Shot Dist (m)	Shot Elev. (m)
1	0	11.05			
2	5.04	11.27	2	5.04	11.28
3	9.96	11.2	3	9.96	11.21
4	14.85	11.02	4	15.39	11.09
5	19.98	10.85	5	20.06	10.88
6	24.97	10.77	6	24.89	10.92
7	29.91	10.69	7	29.7	10.75
8	34.6	10.57	8	34.83	10.51
9	39.8	10.34	9	39.8	10.35
10	44.95	10.05	10	44.74	10.13
11	49.72	10	11	49.53	10.07
12	54.48	9.94	12	54.32	10.01
13	59.25	9.89	13	59.11	9.94
14	64.02	9.83	14	63.9	9.88
15	68.78	9.78	15	68.69	9.82
16	73.55	9.72	16	73.48	9.76
17	78.32	9.67	17	78.27	9.69
18	83.08	9.61	18	83.06	9.63
19	87.85	9.56	19	87.85	9.57
20	92.13	9.47	20	92.13	9.48
21	96.83	9.44	21	96.83	9.45
22	101.37	9.17	22	101.9	9.33
23	105.99	9.01	23	105.99	9.02
24	110.63	8.97	24	110.63	8.98
25	115.29	8.71	25	115.69	8.92
26	119.88	8.71	26	120.23	8.72
27	124.5	8.6	27	124.83	8.62
28	129.21	8.49	28	129.52	8.7
29	133.77	8.49	29	134.05	8.51
30	138.36	8.35	30	138.79	8.5
31	143.04	8.36	31	143.42	8.33
32	147.49	8.23	32	148.06	8.33
33	152.35	8.04	33	152.63	8.14
34	156.96	7.97	34	157.32	8.03
35	161.37	7.74	35	161.95	7.9
36	166.05	7.57	36	166.5	7.8
37	170.62	7.8	37	170.62	7.81
38	175.25	7.75	38	175.25	7.76
39	179.89	7.71	39	179.89	7.72
40	184.52	7.66	40	184.52	7.67
41	189.41	7.53	41	189.41	7.55
42	194.3	7.41	42	194.3	7.42
43	198.97	7.28	43	198.97	7.29
44	203.49	7.08	44	203.49	7.09
45	208	6.88	45	208	6.89
46	212.52	6.68	46	212.52	6.69
47	217.16	6.44	47	217.16	6.45
48	222.42	6.3	48	221.66	6.46
49	227.07	6.32	49	226.39	6.46
50	231.21	6.94	50	231.21	6.95
51	235.72	6.83	51	235.72	6.84
52	240.44	6.68	52	240.44	6.69
53	244.61	6.45	53	244.61	6.46
54	249.51	6.46	54	249.51	6.47
55	254.14	6.29	55	254.14	6.3
56	259.23	6.2	56	259.23	6.21
57	264.12	5.95	57	264.12	5.96
58	268.81	6.19	58	268.81	6.2

Appendix C

Distances and elevations along SCSI-3.
Measurements are relative to the first geophone at the south end of the line.

Geophone No.	Geo. Dist. (m)	Geo. Elev. (m)	Shot Point No.	Shot Dist (m)	Shot Elev. (m)
1	0.45	9.32			
2	4.95	9.21			
3	9.54	9.16			
4	14.06	9.18	4	13.61	9.17
5	18.38	9.26	5	17.93	9.23
6	22.88	9.25	6	22.49	9.17
7	27.39	9.45			
8	31.63	9.7	8	31.15	9.59
9	35.9	10.02	9	35.28	9.94
10	40	10.26	10	39.37	10.2
11	44.15	10.26	11	43.47	10.3
12	48.28	10.2	12	47.7	10.17
13	52.01	10.23	13	51.38	10.16
14	56.32	10.09	14	55.67	10.1
15	60.22	10	15	59.69	10.05
16	64.44	9.95	16	63.87	10.01
17	68.41	9.82	17	67.84	9.92
18	72.25	9.83	18	71.89	9.84
19	76.9	9.67	19	76.53	9.76
20	81.57	9.76	20	81.07	9.76
21	86.55	9.47	21	86.05	9.47
22	91.54	9.18	22	91.04	9.18
23	96.52	8.88	23	96.02	8.88
24	101.5	8.59	24	101	8.59
25	106.5	8.3	25	106	8.3
26	111.48	8.01	26	110.98	8.01
27	114.95	9.11	27	114.45	9.11
28	119.95	9.15	28	119.45	9.15
29	124.35	9.19	29	123.98	8.81
30	129.13	8.99	30	128.82	8.78
31	133.95	8.5	31	133.67	8.47
32	138.72	8.26	32	138.24	8.21
33	143.38	8.05	33	143.21	7.94
34	148.05	7.96	34	147.81	7.8
35	152.98	7.69	35	152.61	7.68
36	157.82	7.4	36	157.61	7.38
37	162.81	7.17	37	162.63	7.17
38	167.53	6.85	38	167.34	6.81
39	172.58	6.51	39	172.26	6.51
40	177.31	6.21	40	177.33	6.21
41	182.2	5.86	41	182.27	5.87
42	187.56	5.63	42	187.45	5.6
43	192.42	5.34	43	192.39	5.32
44	197.2	5.13	44	197.2	5.12
45	202.27	4.87	45	202.29	4.82
46	207.14	4.55	46	207.16	4.51
47	212.2	4.3	47	212.13	4.3
48	217.05	4.12	48	217.12	4.07
49	222.1	3.94	49	222.1	3.92
50	226.92	3.69	50	227.16	3.69
51	231.91	3.43	51	232.11	3.49
52	237.05	3.25	52	237.16	3.27
53	241.91	3.06	53	241.97	3.05
54	246.87	2.92	54	246.97	2.83
55	251.84	2.63	55	251.96	2.65
56	256.82	2.49	56	256.98	2.49
57	261.83	2.25	57	261.94	2.21
58	266.67	2.12	58	266.92	2.05
59	271.6	1.91	59	271.77	1.9
60	276.56	1.92	60	276.73	1.83
61	281.49	1.87	61	281.67	1.8
62	286.18	1.83	62	286.45	1.7
63	291	1.75	63	291.4	1.69
64	295.94	1.8	64	296.14	1.73
65	300.75	1.72	65	300.96	1.69
66	305.56	1.66	66	305.84	1.66
67	310.39	1.65	67	310.52	1.69
68	315.18	1.59	68	315.7	1.52
69	320.07	1.58	69	320.37	1.58
70	324.89	1.57	70	325.06	1.55
71	329.75	1.47	71	330.02	1.49
72	334.45	1.51	72	334.77	1.42
73	339.39	1.5	73	339.61	1.4
74	344.21	1.48			
75	349.1	1.35	75	349.45	1.33
76	353.95	1.31	76	354.24	1.31

77	358.8	1.35	77	359.02	1.28
78	363.42	1.34	78	364.04	1.28
79	368.42	1.35	79	368.7	1.33
80	373.27	1.27	80	373.43	1.28
81	378.12	1.25	81	378.48	1.3
82	382.83	1.31	82	383.33	1.31
83	387.77	1.27	83	388.09	1.31
84	392.53	1.25	84	392.91	1.14
85	397.49	1.25	85	397.57	1.23
86	402.23	1.23	86	402.54	1.15
87	406.93	1.23	87	407.39	1.07
88	411.9	1.15	88	412.26	1.17
89	416.74	1.12	89	416.91	1.07
90	421.64	1.1	90	421.9	1.1
91	426.57	1.11	91	426.71	1.15
92	431.22	1.11			
93	436.31	1.19			
94	440.98	1.11	94	441.16	1.08
95	445.79	1.06	95	446.06	1.14
96	450.9	1.01	96	450.95	0.99
97	455.9	1	97	456.04	0.93
98	460.87	0.98	98	460.97	0.94
99	466.02	0.92	99	466.03	0.97
100	470.89	0.9	100	470.82	0.99
101	475.93	0.89	101	475.94	0.97
102	481.01	0.94	102	480.91	0.9
103	486.12	0.96	103	485.96	0.96
104	491.08	0.96	104	490.9	0.96
105	496.11	0.96	105	496.06	0.93
106	501.08	0.89	106	500.78	0.99
107	506.09	0.85	107	505.9	0.94
108	510.96	0.88	108	510.84	0.87
109	516.01	0.79	109	515.77	0.81
110	520.85	0.84	110	520.62	0.85
111	525.7	0.78	111	525.59	0.85
112	530.62	0.77	112	530.38	0.9
113	535.55	0.71	113	535.3	0.7
114	540.4	0.67	114	540.17	0.69
115	545.29	0.53	115	545.02	0.58
116	550.19	0.32	116	549.87	0.27
117	554.8	0.13	117	554.36	0.04
118	559.37	0.02	118	558.93	0

Appendix D

Distances and elevations along SCSI-4.
Measurements are relative to the first geophone at the south end of the line.

Geophone No.	Geo. Dist. (m)	Geo. Elev. (m)	Shot Point No.	Shot Dist (m)	Shot Elev. (m)
1	0	1.61	1	0.51	1.56
2	4.88	1.42	2	5.21	1.33
3	9.82	1.31	3	10.21	1.29
4	14.57	1.34	4	14.84	1.29
5	19.4	1.4	5	19.38	1.41
6	24.23	1.42	6	24.37	1.4
7	29.14	1.33	7	29.18	1.38
8	34.12	1.25	8	34.17	1.28
9	38.82	1.21	9	39.01	1.22
10	43.79	1.14	10	43.99	1.13
11	48.85	1.06	11	48.93	1.09
12	53.64	1.04	12	53.71	1.09
13	58.65	1.02	13	58.84	1.04
14	63.62	0.96	14	63.66	0.96
15	68.59	0.95	15	68.54	1.07
16	73.56	0.93	16	73.66	0.98
17	78.54	1	17	78.52	1.05
18	83.35	1.04	18	83.36	1.1
19	87.71	0.99			
20	93.07	0.94			
21	98.43	0.89	21	98.33	0.92
22	103.54	0.81	22	103.49	0.86
23	108.43	0.71	23	108.5	0.74
24	113.6	0.58	24	113.44	0.62
25	118.46	0.44	25	118.42	0.43
26	123.49	0.39	26	123.29	0.43
27	128.4	0.47	27	128.3	0.47
28	133.44	0.5	28	133.43	0.59
29	138.36	0.56	29	138.23	0.6
30	143.31	0.55	30	143.18	0.64
31	148.36	0.59	31	148.1	0.69
32	153.36	0.57	32	153.24	0.6
33	158.33	0.49	33	158.27	0.49
34	163.34	0.45	34	163.21	0.46

35	168.33	0.43	35	168.28	0.46
36	173.34	0.47	36	173.17	0.48
37	178.27	0.42	37	178.09	0.46
38	183.35	0.41	38	182.99	0.46
39	188.14	0.4	39	187.92	0.44
40	193.16	0.43	40	192.97	0.48
41	198.08	0.44	41	197.86	0.44
42	202.98	0.4	42	202.89	0.52
43	208.09	0.43	43	207.95	0.54
44	212.84	0.44	44	212.71	0.54
45	217.8	0.41	45	217.41	0.5
46	222.84	0.36	46	222.61	0.45
47	227.81	0.28	47	227.61	0.38
48	232.54	0.14	48	232.11	0.3
49	237.48	0	49	237.07	0.14

Appendix E

Distances and elevations along SCSI-5.
Measurements are relative to the first geophone at the south end of the line.

Geophone No.	Geo. Dist. (m)	Geo. Elev. (m)	Shot Point No.	Shot Dist (m)	Shot Elev. (m)
1	0.02	13.44	1	0	13.4
2	5.05	13.33	2	5.04	13.26
3	10.01	13.21	3	9.9	13.16
4	15.06	13.01	4	14.9	13.05
5	20.17	12.87	5	19.97	12.86
6	25.05	12.71	6	24.81	12.72
7	30.07	12.59	7	29.85	12.55
8	35.05	12.49	8	34.84	12.45
9	40	12.41	9	39.92	12.36
10	45.08	12.26	10	44.81	12.26
11	49.97	12.21	11	49.74	12.13
12	54.99	12.13	12	54.81	12.13
13	59.97	12.16	13	59.79	12.1
14	64.92	12.16	14	64.96	12.1
15	69.97	12.09			
16	74.88	12.08	16	74.78	12.03
17	79.93	12.03	17	79.73	12.02
18	85.01	12.02	18	84.72	11.99
19	89.92	11.98	19	89.66	11.94
20	94.92	11.92	20	94.73	11.9
21	99.93	11.86	21	99.62	11.83
22	104.75	11.89			
23	109.72	11.92	23	109.69	11.85
24	114.73	11.93	24	114.43	11.89
25	119.81	11.92	25	119.49	11.92
26	124.77	11.95	26	124.37	11.91
27	129.76	11.9	27	129.5	11.87
28	134.73	11.86	28	134.53	11.8
29	139.83	11.77	29	139.6	11.78
30	144.73	11.74	30	144.54	11.76
31	149.73	11.7	31	149.4	11.67
32	154.74	11.62	32	154.51	11.6
33	159.7	11.46	33	159.61	11.43
34	164.72	11.31			
35	169.72	11.18			
36	174.73	11.05			
37	179.73	10.92	37	179.43	10.89
38	184.51	10.86			
39	189.54	10.86	39	189.31	10.81
40	194.6	10.93	40	194.38	10.88
41	199.62	10.99	41	199.38	10.91
42	204.51	10.99			
43	209.44	11.02	43	209.31	11
44	214.52	11.18	44	214.2	11.05
45	219.54	11.23	45	219.2	11.14
46	224.51	11.3	46	224.2	11.24
47	229.43	11.37	47	229.25	11.34
48	234.45	11.43	48	234.25	11.4
49	239.36	11.24			
50	244.27	11.04			
51	249.19	10.84			
52	254.1	10.65	52	253.96	10.66
53	259.01	10.57			
54	264.14	10.55	54	263.97	10.4
55	269.15	10.37			
56	274.08	10.36	56	273.83	10.2
57	279.13	10.16	57	278.85	10.18
58	284.16	10.15	58	283.91	10.08
59	289.05	9.96	59	288.72	9.96
60	294	10.03			
61	298.95	10.11	61	298.76	9.89

62	303.88	9.81	62	303.68	9.94
63	308.99	9.83	63	308.8	9.79
64	313.91	9.69	64	313.69	9.7
65	318.87	9.6	65	318.68	9.63
66	323.8	9.43	66	323.68	9.44
67	328.86	9.33			
68	334.08	9.32	68	333.88	9.29
69	338.92	9.15	69	338.76	9.11
70	343.97	9.14	70	343.86	9.09
71	348.86	8.91	71	348.77	8.86
72	353.89	8.72	72	353.8	8.67
73	358.81	8.62	73	358.79	8.61
74	363.81	8.55	74	363.76	8.56
75	368.8	8.5	75	368.75	8.48
76	373.82	8.48	76	373.75	8.46
77	378.65	8.46	77	378.81	8.44
78	383.55	8.45	78	383.77	8.48
79	388.66	8.44	79	388.71	8.44
80	394.7	8.51	80	394.7	8.51
81	398.6	8.45	81	398.6	8.45
82	403.65	8.43	82	403.64	8.41
83	408.34	8.38	83	408.32	8.38
84	413.33	8.4	84	413.33	8.4
85	418.26	8.36	85	418.15	8.38
86	423.38	8.38	86	423.38	8.38
87	428.32	8.35	87	428.32	8.37
88	433.29	8.33	88	433.15	8.34
89	438.25	8.3	89	438.16	8.29
90	443.21	8.35	90	443.21	8.35
91	447.96	8.33	91	448.1	8.31
92	452.94	8.24	92	453.1	8.25
93	458.09	8.26	93	458.09	8.26
94	463.01	8.3	94	463.08	8.27
95	468.07	8.29	95	468	8.26
96	473.03	8.33			
97	477.84	8.58	97	477.94	8.62
98	483.07	8.63	98	482.97	8.65
99	487.88	8.11	99	487.85	8.12
100	492.9	7.64	100	492.89	7.76
101	497.78	7.57	101	497.85	7.62
102	502.85	7.33	102	502.85	7.42
103	507.89	7.38	103	507.85	7.32
104	512.86	7.3	104	512.69	7.3
105	517.74	7.18	105	517.21	7.11
106	522.7	7.11			
107	527.58	6.97			
108	532.64	6.87	108	532.94	6.78
109	537.38	7.04	109	537.64	6.99
110	542.63	6.46	110	542.63	6.37
111	547.2	6.24	111	547.45	6.24
112	550.93	6.37	112	550.89	6.53
113	557.34	6.6	113	557.17	6.41
114	562.47	6.53	114	562.28	6.51
115	567.2	6.44	115	567.11	6.43
116	572.36	6.39	116	572.23	6.39
117	577.19	6.29	117	577.17	6.28
118	582.15	6.2			
119	586.99	6.11	119	586.99	6.11
120	592.21	6.04	120	592.21	5.86
121	597.36	6.04	121	597.53	5.84
122	602.17	6.01	122	602.15	5.84
123	607.26	6.08	123	607.16	5.99
124	612.35	6.15	124	612.17	6.14
125	617.09	6.24	125	616.94	6.1
126	621.96	6.12	126	621.63	5.99
127	626.85	5.79	127	626.34	5.81
128	631.53	5.71	128	630.92	5.53
129	636.51	5.41	129	636.26	5.36
130	641.23	5.38			
131	646.02	5.07			
132	650.96	4.44			
133	656.7	4.6			
134	661.51	4.4			
135	666.57	4.29			
136	671.5	4.29			
137	676.38	4.31	137	676.51	4.29
138	681.24	4.43	138	681.18	4.37
139	686.5	4.49	139	686.48	4.43
140	690.81	4.52	140	690.75	4.46
141	696.41	4.46			
142	701.55	4.38			
143	706.31	4.29	143	706.37	4.2

144	711.63	4.16	144	711.58	4.02
145	716.69	4.04	145	716.62	3.94
146	721.51	3.92	146	721.49	3.81
147	726.17	3.77	147	726.2	3.69
148	731.25	3.6	148	731.38	3.55
149	735.65	3.48	149	735.98	3.44
150	741.39	3.33	150	741.64	3.33
151	746.33	3.31	151	746.37	3.38
152	751.36	3.45	152	751.19	3.59
153	755.75	3.22	153	755.79	3.25
154	760.94	2.48	154	760.89	2.57
155	765.83	2.13	155	765.8	2.14
156	770.85	1.9	156	770.92	2.02
157	776.07	1.9	157	775.94	1.96
158	781.03	2.31	158	780.81	2.37
159	785.51	2.47	159	785.43	2.62
160	790.53	1.93			
161	795.29	1.23	161	795.13	1.3
162	800.25	1.26	162	799.87	1.33
163	804.94	1.84	163	804.4	1.92
164	809.57	1.82	164	809.17	2.03
165	813.89	1.14	165	814.05	1.13
166	818.01	0	166	818.27	0.3

Appendix F

Distances and elevations along SCSI-6.
Measurements are relative to the first geophone at the south end of the line.

Geophone No.	Geo. Dist. (m)	Geo. Elev. (m)	Shot Point No.	Shot Dist (m)	Shot Elev. (m)
1	0.57	3.1			
2	5	2.79			
3	8.73	2.48	3	8.41	2.42
4	13.49	2.38	4	12.65	2.07
5	16.61	2.02	5	16.06	1.97
6	21.47	1.97	6	21.05	1.77
7	26.06	2.09	7	25.74	1.75
8	30.85	2.02	8	30.45	1.78
9	35.41	2.1	9	35.23	1.91
10	40.25	2.11	10	40.07	1.86
11	45.1	2.09	11	44.76	1.83
12	49.45	2.06	12	49.25	1.63
13	54.55	1.95	13	54.23	1.87
14	59.24	1.84	14	58.83	1.75
15	63.68	1.92	15	63.78	1.64
16	68.78	2.18	16	68.64	1.9
17	73.75	2.08	17	73.83	2.02
18	78.06	1.95	18	77.91	1.81
19	83.4	2.04	19	83.52	1.92
20	88.67	1.8	20	88.69	1.75
21	93.67	1.74	21	93.58	1.69
22	98.33	1.64	22	98.27	1.64
23	103.48	1.55	23	103.45	1.51
24	108.52	1.63	24	108.36	1.61
25	113.76	1.7	25	113.75	1.57
26	119.04	1.63	26	118.98	1.6
27	123.72	1.59	27	123.69	1.51
28	128.78	1.47	28	128.77	1.48
29	133.7	1.55	29	133.73	1.46
30	138.53	1.42	30	138.69	1.47
31	143.66	1.44	31	143.71	1.38
32	148.62	1.35	32	148.8	1.3
33	153.63	1.33	33	153.69	1.27
34	158.8	1.33	34	158.73	1.23
35	163.51	1.23	35	163.69	1.16
36	168.8	1.17	36	168.76	1.04
37	173.75	1.28	37	173.78	1.09
38	178.55	1.33			
39	183.68	1.3	39	183.73	1.09
40	188.48	1.01			
41	193.74	0.85	41	193.48	0.9
42	198.59	0.72	42	198.37	0.7
43	203.52	0.55	43	203.44	0.48
44	208.52	0.37	44	208.32	0.3
45	213.37	0.3	45	213.21	0.16
46	218.25	0.28	46	218.11	0.37
47	223.25	0.2	47	223	0.1
48	228.06	0.13	48	227.91	0.04
49	233.04	0.13	49	232.84	0
50	237.76	0.15	50	237.8	0.08

Appendix G

Distances and elevations along SCSI-7.
Measurements are relative to the first geophone at the south end of the line.

Geophone No.	Geo. Dist. (m)	Geo. Elev. (m)	Shot Point No.	Shot Dist (m)	Shot Elev. (m)
1	0	7.29	1	0	7.47
2	4.82	7.25	2	4.57	7.48
3	9.67	7.32	3	9.4	7.44
4	14.59	7.34	4	14.32	7.47
5	19.41	7.35	5	19.14	7.48
6	24.3	7.37	6	24.06	7.49
7	29.14	7.35	7	28.91	7.51
8	34.2	7.34	8	33.85	7.47
9	38.96	7.33	9	38.64	7.43
10	43.75	7.3	10	43.5	7.37
11	48.49	7.29	11	48.34	7.36
12	53.41	7.25	12	53.31	7.34
13	58.26	7.31	13	57.94	7.4
14	63.04	7.32	14	62.89	7.43
15	67.99	7.35	15	67.79	7.43
16	72.92	7.3			
17	77.84	7.25	17	77.63	7.38
18	82.51	7.23	18	82.36	7.43
19	87.35	7.16	19	87.15	7.43
20	92.13	6.98	20	92.03	7.36
21	97.48	6.89			
22	102.24	6.78	22	102.11	7.03
23	107.08	6.74	23	107.03	6.85
24	112.16	6.49	24	111.79	6.64
25	116.97	6.23	25	116.57	6.4
26	121.75	5.93	26	121.26	6.23
27	126.49	5.85	27	126.17	6.05
28	131.32	5.65	28	130.95	5.9
29	135.98	5.57	29	135.71	5.81
30	141.01	5.45	30	140.53	5.74
31	145.57	5.44	31	145.41	5.66
32	150.58	5.33	32	150.33	5.54
33	155.23	5.26	33	154.93	5.57
34	160.12	5.23	34	159.82	5.52
35	165.08	5.12	35	164.8	5.52
36	169.94	5.07	36	169.67	5.47
37	174.84	5.18	37	174.51	5.46
38	179.62	5.24	38	179.39	5.5
39	184.51	5.34	39	184.32	5.53
40	189.33	5.13	40	189.13	5.45
41	194.12	5.13	41	194.07	5.46
42	198.96	5.15	42	198.97	5.43
43	203.87	5.29	43	203.73	5.44
44	208.76	5.19	44	208.53	5.48
45	213.38	5.26	45	213.38	5.43
46	218.32	5.22	46	218.03	5.42
47	223.4	5.09	47	223.07	5.38
48	227.98	5.14	48	227.8	5.44
49	232.94	5.33	49	232.8	5.42
50	237.83	5.32	50	237.64	5.44
51	242.81	5.29	51	242.57	5.46
52	247.38	5.26	52	247.29	5.52
53	252.42	5.26	53	252.35	5.51
54	257.33	5.26	54	257.25	5.44
55	262.27	5.12	55	262.05	5.41
56	267.17	5.16	56	267	5.45
57	271.85	5.12	57	271.76	5.41
58	276.7	5.1	58	276.67	5.38
59	281.5	5.09	59	281.4	5.37
60	286.68	5.06	60	286.46	5.36
61	291.73	5.28			
62	296.22	5.37	62	296.06	5.42
63	301.08	5.37	63	300.95	5.4
64	305.79	5.44	64	305.6	5.47
65	310.61	5.54	65	310.67	5.47
66	315.56	5.55	66	315.38	5.52
67	320.79	5.89	67	320.64	5.54
68	325.41	5.97	68	325.03	5.53
69	330.3	6.06	69	329.9	5.51
70	335.1	6.23	70	334.86	5.52
71	339.86	5.81	71	339.78	5.51
72	344.59	5.98	72	344.61	5.49
73	349.44	5.36	73	349.34	5.32
74	354.22	4.86	74	354.38	5.12
75	359.05	4.73	75	359.27	4.81
76	363.7	4.45	76	363.97	4.55
77	367.91	3.92	77	368.36	4.18

78	371.85	3.66	78	372.38	3.85
79	375.45	3.33	79	376.12	3.51
80	378.74	3.31	80	379.17	3.27
81	381.75	3.13	81	382.07	3.12
82	385.03	2.93	82	385.45	2.96
83	389.35	2.71			
84	393.74	2.46	84	394.07	2.53
85	397.7	2.18	85	398.26	2.35
86	401.36	2.12	86	401.95	2.17
87	404.49	1.86	87	405.07	1.94
88	407.49	1.51	88	408.1	1.69
89	411.2	1.42	89	411.61	1.5
90	415.3	1.41	90	415.16	1.41
91	418.76	1.26	91	419.09	1.3
92	422.8	1.22	92	423.17	1.22
93	426.46	1.16	93	427.14	1.19
94	430.56	1.02	94	430.66	1.04
95	435.1	0.93			
96	439.65	0.82	96	439.75	0.82
97	444.24	0.69	97	444.43	0.78
98	448.95	0.59	98	449.03	0.65
99	452.48	0.56	99	452.58	0.47
100	458.31	0.21	100	458.45	0.27
101	462.87	0.09	101	462.93	0.15
102	467.34	0.09	102	467.53	0.08
103	471.89	0.05			
104	476.53	0.07	104	476.69	0.03
105	481.35	0.1			
106	486.02	0.16	106	486.11	0.15
107	490.7	0.19	107	490.76	0.19
108	495.24	0.25	108	495.32	0.26
109	500.22	0.34	109	500.23	0.29
110	504.89	0.41	110	505.01	0.36
111	509.65	0.5	111	509.77	0.45
112	514.57	0.56	112	514.72	0.59
113	519.53	0.67	113	519.61	0.71
114	524.37	0.87	114	524.42	0.93
115	529.14	1.18	115	529.26	1.14
116	533.9	1.44	116	534.09	1.43
117	538.55	1.77	117	538.71	1.63
118	543.29	2.02	118	543.54	2.01

Appendix H

Distances and elevations along SCSI-8.
Measurements are relative to the first geophone at the south end of the line.

Geophone No.	Geo. Dist. (m)	Geo. Elev. (m)	Shot Point No.	Shot Dist (m)	Shot Elev. (m)
1	0	0.6			
2	4.25	0.67			
3	8.59	0.76			
4	13.05	0.82			
5	17.57	0.93			
6	21.97	1.13			
7	26.3	1.44			
8	30.62	1.7			
9	34.85	2.03			
10	39.15	2.28			
11	43.38	2.55	11	43.91	2.46
12	47.59	2.64	12	47.89	2.61
13	51.85	2.63	13	52.3	2.63
14	55.95	2.67	14	56.32	2.69
15	60.24	2.72	15	60.33	2.69
16	64.51	2.68	16	64.7	2.68
17	68.94	2.64	17	69.01	2.62
18	73.77	2.65	18	73.75	2.65
19	78.52	2.69	19	78.53	2.69
20	83.73	2.75	20	83.69	2.7
21	88.55	2.74	21	88.55	2.72
22	93.63	2.69	22	93.56	2.67
23	98.5	2.59	23	98.49	2.57
24	103.56	2.44	24	103.54	2.4
25	108.75	2.33	25	108.79	2.25
26	113.56	2.1	26	113.45	2.06
27	118.64	1.91	27	118.6	1.91
28	123.71	1.77	28	123.59	1.8
29	128.34	1.71	29	128.39	1.72
30	133.47	1.6	30	133.46	1.6
31	138.54	1.5	31	138.55	1.51
32	143.45	1.44	32	143.41	1.45
33	148.62	1.4	33	148.52	1.35
34	153.15	1.32	34	153.1	1.31
35	158.43	1.24	35	158.49	1.16

36	163.43	1.21	36	163.41	1.16
37	168.39	1.18	37	168.38	1.09
38	173.61	1.19	38	173.56	1.13
39	178.35	1.19	39	178.3	1.15
40	183.54	1.18	40	183.48	1.16
41	188.39	1.19	41	188.32	1.18
42	193.36	1.25	42	193.11	1.19
43	198.31	1.28			
44	203.12	1.15	44	203.04	1.21
45	208.22	1.23	45	208.25	1.21
46	213.24	1.17	46	213.2	1.16
47	218.27	1.16	47	218.27	1.13
48	223.12	1.04	48	223.18	1.08
49	228.18	1	49	228.13	1.06
50	233.16	0.93	50	233.11	0.98
51	238.15	0.86	51	238.09	0.91
52	242.73	0.78	52	242.68	0.8
53	246.67	0.61	53	246.38	0.63
54	250.76	0.31	54	250.08	0.47
55	254.9	0.17	55	254.66	0.32
56	259.42	0.14	56	259.24	0.29
57	264.2	0.04	57	264.15	0.2
58	269.11	0.13	58	269.07	0.22
59	273.98	0.43	59	274.06	0.28
60	279.04	0.13	60	279.11	0.14
61	283.65	0.09	61	283.97	0.12
62	288.9	0	62	289	0.1
63	294.06	0.02	63	293.96	0.19
64	299.32	0.2	64	299.25	0.27
65	304.3	0.14	65	304.15	0.29
66	309.08	0.18	66	309.08	0.29
67	313.95	0.25	67	314.09	0.44
68	319	0.28	68	319.09	0.59
69	323.7	0.27	69	324	0.75
70	328.59	0.84	70	328.74	1.06
71	333.05	1.37	71	333.5	1.33
72	338.37	1.84	72	338.13	1.8

Appendix I

Distances and elevations along SCSI-9.
Measurements are relative to the first geophone at the south end of the line.

Geophone No.	Geo. Dist. (m)	Geo. Elev. (m)	Shot Point No.	Shot Dist (m)	Shot Elev. (m)
1	1.31	7.14	1	0	6.91
2	3.34	7.22	2	2.15	6.91
3	6.26	7.11	3	5.4	6.89
4	8.7	6.99	4	7.59	6.9
5	11.77	6.99	5	10.8	6.85
6	14.7	6.89	6	13.94	6.66
7	17.82	6.72	7	17.04	6.47
8	21.24	6.61	8	20.62	6.01
9	24.64	5.61	9	24.64	5.61
10	29.35	5.73	10	28.94	5.61
11	33.13	6.29	11	32.66	5.94
12	38.44	7.05	12	38.28	6.8
13	42.71	7.55	13	42.76	7.32
14	48.23	7.73	14	48.25	7.6
15	53.17	7.65	15	53.2	7.68
16	58.7	7.74	16	58.44	7.78
17	63.97	8.05	17	63.63	7.8
18	69.51	8.09			
19	76.11	7.38			
20	81.33	7.77	20	80.8	7.37
21	87.29	7.67	21	87.04	7.29
22	92.17	7.52	22	92.21	7.25
23	96.5	7.47	23	96.39	7.29
24	100.97	7.73	24	100.76	7.43
25	105.26	7.34	25	104.96	7.27
26	109.36	7.07	26	108.93	7.08
27	112.45	7	27	111.73	6.98
28	116.93	7.32	28	116.13	7.17
29	121.3	7.31	29	121.24	7.21
30	125.73	7.33	30	125.61	7.25
31	130.96	7.23	31	130.63	7.17
32	135.77	7.12	32	135.41	7.12
33	140.66	7.2	33	140.36	7.19
34	145.43	7.32			
35	149.71	7.38			
36	154.87	7.21	36	154.65	7.15
37	159.97	7.9	37	159.82	7.3
38	165	8.34	38	164.7	7.56
39	169.83	8.42			

40	174.31	8.39	40	173.77	7.8
41	178.27	8.16	41	177.85	7.7
42	182.53	7.62	42	182.04	7.34
43	186.46	7.42	43	186.03	6.98
44	190.51	7.09	44	189.74	6.88
45	193.92	7.12	45	193.41	6.82
46	197.38	6.91			
47	201.42	7.04	47	201.2	6.17
48	205.73	7.26	48	205.73	6.26
49	210.42	7.38	49	210.42	6.38
50	215.12	7.33			
51	219.78	6.48	51	218.87	6.05
52	223.28	5.84	52	222.43	5.56
53	226.5	5.38	53	225.76	5.14
54	230.04	5.28	54	229.31	4.96
55	233.85	4.98	55	233.46	4.82
56	238.09	4.85	56	237.64	4.66
57	242.35	4.97	57	241.9	4.68
58	246.68	5.09	58	246.23	4.79
59	250.79	5.04	59	250.37	4.82
60	255.04	4.96	60	254.61	4.82
61	259.45	4.92	61	259.04	4.79
62	263.93	4.99	62	263.49	4.8
63	268.3	5.07	63	267.8	4.81
64	272.75	4.99	64	272.06	4.74
65	277.02	5.39	65	276.46	5.03
66	280.9	5.72	66	280.22	5.25
67	285.29	6.15	67	284.68	5.94
68	289.65	7.14	68	288.69	6.41
69	293.8	7.1	69	292.83	6.95
70	297.51	6.88	70	297.08	6.72
71	302.09	7.03	71	301.34	6.85
72	306.24	7.02	72	305.55	7.02
73	310.35	7.08	73	309.67	7.09
74	314.54	7.06	74	313.97	7
75	318.58	6.93	75	318.19	6.92
76	323.23	6.91	76	322.35	6.9
77	327.13	6.89	77	326.45	6.85
78	331.36	6.74	78	330.7	6.79
79	335.43	6.7	79	334.92	6.69
80	339.54	6.61	80	338.94	6.64
81	343.7	6.56			
82	347.96	6.42	82	347.35	6.41
83	352.33	6.26	83	351.6	6.35
84	355.88	6.18			
85	359.94	6.25			
86	364.13	6.2			
87	368.31	6.13			
88	372.52	6.04			
89	376.69	5.97			
90	380.9	5.88			
91	385.05	5.82			
92	389.27	5.74			
93	393.45	5.66			
94	398.88	5.53	94	398.03	5.52
95	402.18	5.44	95	401.85	5.39
96	407.28	5.31			
97	411.05	5.01	97	410.54	5.01
98	415.33	4.73	98	414.82	4.68
99	419.7	4.35	99	419.12	4.34
100	423.93	4.33			
101	428.4	4.38			
102	432.36	4.23	102	431.95	4.23
103	436.54	4.08	103	435.93	4.19
104	440.82	4.23	104	440.25	4.44
105	443.74	4.41	105	443.25	4.65
106	446.81	4.26	106	446.2	4.33
107	450.42	3.96	107	450.09	3.9
108	455.66	3.95			
109	461.9	3.52	109	461.58	3.53
110	467.69	3.39	110	467.32	3.44
111	472.41	3.37	111	472.27	3.37
112	477.83	3.31	112	477.58	3.23
113	482.59	3.11			
114	487.32	3.11			
115	492.01	3.07			
116	497.26	2.96	116	497.24	2.94
117	502.31	3.04	117	502.29	2.83
118	507.29	2.99	118	507.33	2.94
119	512.31	2.76	119	512.29	2.74
120	517.33	2.65	120	517.3	2.65
121	522.18	2.53	121	522.23	2.55

122	527.1	2.53	122	527.1	2.53
123	531.97	2.53	123	531.97	2.53
124	536.85	2.52	124	537.06	2.47
125	541.79	2.46	125	542.07	2.42
126	546.86	2.36	126	547	2.35
127	551.89	2.28	127	552.01	2.27
128	556.71	2.25	128	556.94	2.23
129	561.59	2.25	129	561.7	2.15
130	566.01	2.2	130	566.2	2.17
131	571.62	2.18	131	571.81	2.25
132	576.49	2.55	132	576.46	2.43
133	581.33	2.83	133	581.45	2.68
134	586.65	2.97	134	586.53	2.85
135	590.79	3.06			
136	596.51	3.22	136	596.15	3.13
137	601.57	3.32	137	601.43	3.29
138	606.59	3.42			
139	611.27	3.33	139	611.23	3.28
140	616.24	3.53	140	616.26	3.57
141	620.72	3.43	141	620.61	3.6
142	625.64	3.49	142	625.61	3.68
143	630.43	3.35	143	630.63	3.48
144	635.34	3.32	144	635.37	3.47
145	640.14	3.16	145	640.4	3.18
146	645.11	2.92	146	645.58	2.64
147	650.26	2.34	147	650.69	2.16
148	654.69	2.34	148	655.27	2.1
149	659.06	2.27	149	659.36	2.07
150	663.06	1.97	150	663.34	1.8
151	666.75	1.73	151	667.34	1.63
152	670.82	1.67	152	671.24	1.52
153	674.85	1.61	153	675.38	1.58
154	678.64	1.53	154	679.41	1.43
155	681.48	1.52	155	682.06	1.46
156	685.36	1.42	156	685.86	1.42
157	689.3	1.42	157	689.56	1.42
158	692.54	1.34	158	693.23	1.39
159	696.21	1.36	159	696.21	1.36
160	701.49	1.32			
161	706.77	1.28	161	706.77	1.28
162	711.01	1.04	162	711.35	1.08
163	715.09	0.97	163	715.48	0.97
164	719.34	0.98	164	719.75	0.96
165	723.21	0.93			
166	727.36	0.86	166	728.14	0.83
167	731.75	0.82	167	732.45	0.79
168	736.12	0.85	168	736.54	0.8
169	740.33	0.83	169	740.84	0.8
170	744.43	0.82	170	745.02	0.81
171	748.81	1.41			
172	753.17	1.44	172	753.6	0.79
173	757.09	0.89			
174	761.27	0.89	174	761.73	0.88
175	765.43	0.93	175	765.89	0.88
176	769.75	0.96	176	770.16	0.93
177	774.37	1.02	177	774.48	0.95
178	778.52	1.05	178	779.05	0.99
179	783.27	1.01	179	783.61	1.01
180	787.55	1.04	180	788.04	0.99
181	792.73	1.06	181	792.91	1.04
182	797.28	1.05			
183	802.4	1.07			
184	807.05	1.03			
185	812.21	1.04			
186	817.16	1.07			
187	822.12	1.04			
188	826.93	1.05			
189	832.84	1.01	189	833.1	0.97
190	837.6	1.02			
191	842.5	1.07	191	842.74	1.02
192	847.23	1.04	192	847.46	0.98
193	851.94	1.07	193	852.22	1.02
194	856.94	1.06	194	857.11	1.02
195	861.48	1.08	195	861.75	1.05
196	866.36	1.07	196	866.64	1.03
197	871.03	1.05	197	871.55	1.01
198	876.03	1.05	198	876.52	1.02
199	880.52	1.09	199	881.02	1.04
200	884.72	1.07			
201	889.83	1.05			
202	894.67	0.99			
203	899.22	0.92	203	899.48	0.88

204	904.01	0.86	204	904.28	0.79
205	908.52	0.71	205	908.81	0.62
206	913.73	0.43	206	913.92	0.31
207	918.61	0.37	207	919.02	0
208	923.48	0.42	208	923.88	0.09
209	928.36	0.47	209	928.75	0.18
210	933.23	0.52	210	933.61	0.26
211	938.11	0.57	211	938.48	0.35
212	942.98	0.63	212	943.34	0.44
213	947.86	0.68	213	948.21	0.53
214	952.73	0.73			
215	957.61	0.78			
216	962.48	0.83	216	962.8	0.79
217	967.24	0.95			
218	972.05	0.98	218	972.51	0.96
219	977.1	1	219	977.46	0.99
220	981.93	1.01			
221	986.53	0.97	221	986.85	0.93
222	992.95	1.11	222	993.28	1.11
223	996.95	1.22			
224	1001.7	1.13	224	1001.86	1.1
225	1006.65	1.11	225	1006.65	1.1
226	1011.85	1.11	226	1011.77	1.06
227	1016.6	1.08	227	1016.49	1.06
228	1021.83	1.06	228	1021.71	1.04
229	1026.49	1.05	229	1026.41	1.04
230	1031.65	1.06	230	1031.53	1
231	1036.53	1.15	231	1036.5	1.08
232	1041.73	0.99	232	1041.5	0.98
233	1046.7	1.03	233	1046.48	0.97
234	1051.4	1.01	234	1051.35	0.98
235	1056.57	0.99	235	1056.51	0.99
236	1061.39	1.1	236	1061.22	1.06
237	1066.49	0.99	237	1066.23	0.99
238	1071.36	1.17	238	1071.01	1.08
239	1076.11	1.09	239	1075.78	1.09
240	1081.03	1.08	240	1080.72	1.08
241	1086.12	1.07	241	1085.78	1.04
242	1090.53	1.04	242	1090.48	1.01
243	1095.59	1.1	243	1095.31	1.1
244	1100.37	1.03	244	1100.24	1.01
245	1104.96	1.16	245	1104.85	1.13
246	1113.68	0.97	246	1113.6	1
247	1118.71	1.14			
248	1123.59	1.13	248	1123.75	1.1
249	1128.53	1.37			
250	1133.15	1.55			
251	1138.77	1.64	251	1138.77	1.64
252	1143.49	1.67			
253	1148.83	1.82			
254	1153.97	2.21			
255	1159.26	2.45			
256	1164	2.88			
257	1168.81	3.29			
258	1173.6	3.56			
259	1178.47	4.44			
260	1183.54	4.94			
261	1188.02	5.57			
262	1192.56	6.09			
263	1197.66	6.55	263	1197.66	6.55
264	1202.8	8.26	264	1202.75	7.89
265	1206.84	9.36	265	1207	9.3
266	1212.75	9.57			
267	1218.02	9.53			
268	1223.26	9.42			
269	1228.51	9.29			
270	1233.61	9.21			
271	1238.12	9.21			
272	1242.82	9.22	272	1242.63	9.36
273	1247.65	9.2	273	1247.64	9.22
274	1252.5	9.21	274	1252.58	9.17
275	1257.47	9.22	275	1257.65	9.18
276	1262.28	9.28	276	1262.49	9.26
277	1267.35	9.37	277	1267.6	9.22
278	1274.22	9.08	278	1274.7	9.1
279	1279.57	9.16	279	1279.52	9.11
280	1283.94	9.24	280	1284.49	9.17
281	1289.5	9.34			
282	1294.52	9.41			
283	1299.45	9.45			
284	1304.42	9.48			
285	1309.38	9.49			

286	1314.13	9.46	286	1314.09	9.43
287	1319.44	9.55			
288	1324.28	9.52			
289	1329.26	9.47			
290	1334.18	9.45			
291	1339.13	9.42			
292	1344.42	9.32	292	1344.42	9.86
293	1348.63	9.3	293	1349.09	9.3
294	1353.78	9.42	294	1353.81	9.46
295	1358.58	9.57	295	1359	9.61
296	1363.84	9.67	296	1363.82	9.76
297	1369	9.65	297	1369.08	9.76
298	1374.46	9.66	298	1374.07	9.75
299	1379.5	9.78			
300	1384.1	9.93			
301	1389.18	10.12	301	1389.18	10.22
302	1394.2	10.33	302	1393.99	10.48
303	1397.92	10.46	303	1398.1	10.61
304	1403.94	10.68	304	1404.04	10.77
305	1409.08	10.73	305	1409.16	10.87
306	1414.78	10.93			
307	1419.72	11.05	307	1419.71	11.22
308	1424.45	10.99			
309	1429.18	10.93			
310	1434.12	10.94			
311	1439.17	11.13	311	1439.31	11.24
312	1444.55	10.46			
313	1449.68	10.01	313	1449.23	10.26
314	1454.31	9.22			
315	1458.91	8.31	315	1459.14	8.5
316	1463.83	7.42	316	1463.81	7.65
317	1469.11	6.62	317	1468.85	6.81
318	1473.59	5.67	318	1473.48	5.79
319	1478.48	4.95	319	1478.81	5
320	1483.7	4.42	320	1483.6	4.5
321	1488.17	4.01	321	1488.52	4.12
322	1493.34	3.8	322	1493.56	3.85
323	1498.44	3.52	323	1498.78	3.59
324	1504.21	3.23	324	1504.17	3.28
325	1508.61	2.98	325	1508.41	3.07
326	1513.58	2.74	326	1513.53	2.79
327	1518.46	2.48	327	1518.39	2.55
328	1523.21	2.08	328	1523.23	2.09
329	1528.55	1.63	329	1528.42	1.7
330	1533.8	1.21	330	1533.6	1.3
331	1538.8	1.21			
332	1543.8	1.21			

Appendix J

Distances and elevations along SCSI-10.
Measurements are relative to the first geophone at the south end of the line.

Geophone No.	Geo. Dist. (m)	Geo. Elev. (m)	Shot Point No.	Shot Dist (m)	Shot Elev. (m)
1	0	2.42	1	0.22	2.29
2	5	2.42	2	5.28	2.29
3	10.16	2.38	3	10.31	2.3
4	14.99	2.36	4	15.11	2.25
5	19.92	2.38	5	20.19	2.27
6	24.89	2.34	6	24.86	2.27
7	29.87	2.2	7	29.97	2.11
8	34.87	2.18	8	34.97	2.08
9	39.9	2.08	9	39.87	1.98
10	44.6	1.81	10	44.77	1.7
11	49.64	1.54	11	49.79	1.44
12	55.18	1.51	12	55.12	1.29
13	59.48	1.3	13	59.58	1.11
14	64.42	1.23	14	64.63	0.98
15	69.33	1.12	15	69.42	0.93
16	73.96	1	16	74.19	0.81
17	79.06	0.86	17	79.18	0.76
18	84.03	0.8			
19	89.03	0.84	19	89.19	0.77
20	94.04	0.76	20	94.28	0.61
21	98.73	0.57	21	98.81	0.49
22	103.94	0.53	22	103.89	0.4
23	109	0.5	23	108.94	0.42
24	113.49	0.45			
25	118.64	0.41	25	118.93	0.31
26	123.45	0.44	26	123.64	0.35
27	128.58	0.42	27	128.7	0.32
28	133.36	0.54	28	133.64	0.41
29	138.3	0.61	29	138.4	0.52

30	143.15	0.57	30	143.38	0.52
31	148.47	0.64	31	148.44	0.54
32	153.44	0.54	32	153.56	0.47
33	158.38	0.52	33	158.49	0.49
34	163.21	0.43	34	163.23	0.38
35	168.12	0.35	35	168.2	0.3
36	172.9	0.32	36	173.1	0.25
37	177.68	0.35	37	177.94	0.21
38	182.82	0.16	38	182.98	0.12
39	187.87	0.06	39	187.98	0.06
40	192.84	0.03	40	192.95	0.02
41	197.66	0.12	41	197.92	0
42	202.77	0.14	42	202.84	0.06
43	207.8	0.35	43	207.89	0.17
44	213.6	0.29			
45	217.85	0.39	45	217.92	0.28
46	222.66	0.78	46	222.64	0.49
47	227.75	0.99	47	227.69	0.8
48	232.06	1.34	48	232.25	1.13
49	237.18	2.05	49	237.26	1.91
50	242.07	2.64	50	242.29	2.48
51	246.68	3.07	51	247.12	3.02
52	250.82	2.77	52	250.51	2.48
53	254.38	2.31	53	253.82	2.14
54	257.6	1.96	54	257.04	1.62
55	260.99	1.6	55	260.5	1.4
56	264.15	1.49	56	263.58	1.08
57	267.52	1.35	57	266.71	1.05
58	270.52	1.06	58	269.92	0.76
59	273.75	1	59	273.07	0.82
60	277.38	1.43	60	276.46	1.12
61	280.32	1.25	61	279.68	1.06
62	283.78	1.14	62	283.06	0.95
63	286.69	1.44			
64	289.79	1.77	64	288.9	1.32
65	293.36	2.44	65	292.21	2.06
66	296.55	3.29	66	295.65	2.75
67	299.7	4.41	67	299.01	3.99
68	301.92	4.85			

Appendix K

Distances and elevations along SCSI-11.
Measurements are relative to the first geophone at the south end of the line.

Geophone No.	Geo. Dist. (m)	Geo. Elev. (m)	Shot Point No.	Shot Dist (m)	Shot Elev. (m)
1	0.3	7.03	1	0	7.04
2	5.22	6.5	2	4.79	6.46
3	9.91	6.2	3	9.75	6.13
4	14.82	5.86	4	14.75	5.86
5	19.83	5.74	5	19.71	5.76
6	24.79	5.81	6	24.68	5.77
7	29.9	5.72	7	29.69	5.68
8	34.72	5.59	8	34.58	5.64
9	39.59	5.56	9	39.49	5.59
10	44.32	5.49	10	44.54	5.5
11	49.43	5.33	11	49.45	5.41
12	54.32	5.3	12	54.36	5.3
13	59.26	4.68	13	59.44	4.92
14	63.98	4.94	14	64.4	5.06
15	69.31	5.24	15	69.48	5.21
16	74.44	5.21	16	74.41	5.08
17	79.33	5.01	17	79.48	5.07
18	84.37	5.1	18	84.41	5.08
19	89.41	5.06	19	89.41	5.08
20	94.21	5.11	20	94.3	5.09
21	99.15	4.77	21	99.16	5
22	104.29	5.09	22	104.28	5.07
23	109.14	5.07	23	109.36	5.1
24	114.33	5.1	24	114.33	5.04
25	119.09	5.12	25	119.16	5.06
26	124.28	5.07	26	124.27	5.09
27	128.7	5.09			
28	133.48	5	28	133.84	4.9
29	138.39	4.93	29	138.7	4.79
30	143.26	4.93	30	143.46	4.87
31	148.5	4.95	31	148.67	4.89
32	153.26	4.92	32	153.39	4.88
33	158.5	4.9	33	158.55	4.91
34	163.28	4.85	34	163.37	4.8
35	168.42	4.88	35	168.56	4.77
36	173.41	4.82	36	173.33	4.74
37	178.35	4.86	37	178.39	4.84

38	183.05	4.78	38	183.15	4.75
39	188.17	4.67	39	188.26	4.72
40	192.94	4.6	40	193.04	4.59
41	197.94	4.57	41	198.16	4.55
42	203.01	4.53			
43	208.02	4.58	43	208.07	4.56
44	213.07	4.48	44	212.99	4.46
45	217.91	4.41			
46	222.86	4.32	46	223.02	4.35
47	227.94	4.46	47	227.99	4.45
48	232.89	4.34	48	232.93	4.31
49	237.61	4.38			
50	242.71	4.23	50	242.77	4.21
51	247.75	4.25	51	247.81	4.23
52	253.14	4.46	52	253.14	4.46
53	257.44	4.52	53	257.64	4.44
54	262.48	4.35	54	262.6	4.29
55	267	4.34	55	267.31	4.28
56	272.12	4.18	56	272.27	4.26
57	276.86	3.76	57	277.06	3.93
58	281.88	3.59	58	282	3.68
59	286.7	3.39	59	286.83	3.45
60	291.86	3.28	60	291.84	3.23
61	297.31	2.87	61	297.35	2.96
62	302.28	2.86	62	302.37	2.87
63	307.42	2.89	63	307.44	2.9
64	312.53	3.05	64	312.47	3.04
65	317.28	3.49	65	317.3	3.43
66	322.35	3.63	66	322.3	3.64
67	327.3	3.7	67	327.23	3.7
68	332.3	3.67	68	332.28	3.69
69	337.57	3.67	69	337.51	3.67
70	342.83	3.64	70	342.81	3.61
71	347.75	3.62	71	347.64	3.62
72	352.59	3.57	72	352.58	3.55
73	357.7	3.52	73	357.71	3.48
74	362.14	3.42	74	362.16	3.41
75	367.48	3.47	75	367.35	3.38
76	372.39	3.42	76	372.34	3.41
77	377.35	3.44	77	377.36	3.41
78	382.33	3.38	78	382.3	3.36
79	387.33	3.34	79	387.2	3.26
80	392.37	3.3	80	392.28	3.26
81	397.34	3.22			
82	401.61	3.18	82	401.67	3.21
83	407.06	3.17	83	407.02	3.13
84	412.69	3.07	84	412.66	3.06
85	417.17	3.05	85	417.09	3.03
86	422.03	3.04	86	422.07	2.99
87	427.12	3.01			
88	431.89	3.01	88	431.95	3.02
89	437.53	2.94	89	437.56	2.95
90	441.89	2.92	90	441.88	2.91
91	446.98	2.9	91	446.97	2.91
92	451.78	2.9	92	451.69	2.89
93	457.17	2.81	93	457.06	2.83
94	462.03	2.8	94	461.95	2.77
95	467.04	2.71	95	466.76	2.76
96	471.7	2.64	96	471.49	2.65
97	476.32	2.3	97	475.97	2.5
98	480.73	1.93	98	480.47	2.1
99	484.94	1.48	99	484.67	1.78
100	489.58	1.24	100	489.39	1.4
101	494.05	0.99	101	493.76	1.12
102	498.62	0.75	102	498.23	0.88
103	502.76	0.61	103	502.54	0.63
104	507.08	0.22	104	506.75	0.31
105	511.13	0.14	105	510.83	0.17
106	515.8	0.16	106	515.3	0.15
107	519.79	0.32	107	519.39	0.35
108	523.83	0.62			
109	528.58	0.96	109	528.25	1.09
110	532.97	0.93	110	532.69	1.03
111	537.38	0.71	111	537.32	0.82
112	541.76	0.5	112	541.55	0.51
113	546.38	0.32			
114	550.76	0.12			
115	555.65	0.16	115	555.09	0.14
116	559.51	0	116	559.06	0.15
117	563.7	0.1			
118	567.5	0.3	118	567.07	0.31

Appendix L

Distances and elevations along SCSI-12.
Measurements are relative to the first geophone at the south end of the line.

Geophone No.	Geo. Dist. (m)	Geo. Elev. (m)	Shot Point No.	Shot Dist (m)	Shot Elev. (m)
1	0	2.72			
2	4.82	2.72	2	4.9	2.67
3	9.63	2.68	3	9.8	2.62
4	14.89	2.63	4	14.82	2.55
5	19.68	2.57	5	19.83	2.51
6	24.63	2.53	6	24.76	2.46
7	29.64	2.51	7	29.66	2.49
8	34.5	2.49	8	34.74	2.47
9	39.41	2.47	9	39.71	2.43
10	44.51	2.39	10	44.55	2.39
11	49.73	2.34	11	49.57	2.35
12	54.35	2.29	12	54.46	2.3
13	59.35	2.2	13	59.49	2.25
14	64.36	2.16	14	64.54	2.17
15	69.25	2.12	15	69.47	2.12
16	74.19	2.02	16	74.35	2.04
17	78.99	1.95	17	79.13	1.97
18	84.28	1.93	18	84.29	1.92
19	88.93	1.9	19	89.09	1.89
20	94.01	1.86	20	94.13	1.83
21	98.76	1.85	21	98.93	1.83
22	103.89	1.84	22	103.96	1.81
23	108.71	1.84	23	108.87	1.78
24	113.78	1.83	24	113.9	1.79
25	118.77	1.81	25	118.9	1.78
26	123.54	1.78	26	123.62	1.74
27	128.59	1.75	27	128.74	1.73
28	133.32	1.77	28	133.58	1.72
29	138.34	1.76	29	138.46	1.73
30	143.25	1.75	30	143.47	1.69
31	148.36	1.73	31	148.51	1.71
32	153.26	1.73	32	153.39	1.69
33	158.09	1.73	33	158.31	1.7
34	163.16	1.74	34	163.39	1.69
35	168.03	1.76	35	168.13	1.72
36	173.1	1.79	36	173.15	1.74
37	178	1.8	37	178.19	1.75
38	182.94	1.82	38	183.11	1.77
39	187.79	1.83	39	187.99	1.77
40	192.78	1.81	40	192.97	1.74
41	197.93	1.81	41	197.94	1.76
42	202.68	1.81	42	202.88	1.78
43	207.73	1.81	43	207.8	1.77
44	212.49	1.79	44	212.62	1.76
45	217.55	1.78	45	217.75	1.75
46	222.5	1.74	46	222.66	1.71
47	227.48	1.74	47	227.62	1.7
48	232.31	1.72	48	232.55	1.7
49	237.39	1.68	49	237.49	1.68
50	242.29	1.69	50	242.35	1.66
51	247.28	1.68	51	247.41	1.66
52	252.28	1.68	52	252.33	1.67
53	257.14	1.66	53	257.31	1.64
54	261.96	1.62	54	262.11	1.61
55	267.04	1.61	55	267.22	1.61
56	271.92	1.6	56	272.17	1.6
57	276.91	1.58	57	277.1	1.56
58	281.83	1.54	58	281.84	1.49
59	286.96	1.52	59	287.06	1.48
60	291.82	1.52	60	291.99	1.49
61	296.78	1.48	61	296.8	1.52
62	301.62	1.55	62	301.69	1.53
63	306.75	1.59	63	306.65	1.55
64	311.77	1.65	64	311.65	1.59
65	316.76	1.67	65	316.56	1.61
66	321.77	1.7	66	321.52	1.57
67	326.76	1.72	67	326.37	1.71
68	331.62	1.72	68	331.42	1.71
69	336.67	1.71	69	336.44	1.68
70	341.5	1.68	70	341.3	1.66
71	346.53	1.68	71	346.37	1.67
72	351.53	1.69	72	351.28	1.66
73	356.42	1.68	73	356.24	1.67
74	361.29	1.72	74	361.26	1.67
75	366.37	1.74	75	366.15	1.73
76	371.31	1.77	76	371.25	1.75
77	376.28	1.77	77	375.81	1.78

78	380.71	1.82	78	380.47	1.79
79	386.36	1.54	79	386.08	1.73
80	388.76	1.75	80	389.37	1.77
81	392.06	1.76	81	392.83	1.73
82	395.65	1.72	82	396.46	1.72
83	399.04	1.65	83	399.92	1.69
84	402.62	1.7	84	403.18	1.7
85	406.02	1.69	85	406.71	1.72
86	409.29	1.7	86	410	1.72
87	412.7	1.68	87	413.55	1.66
88	416.26	1.62	88	417.06	1.58
89	419.66	1.54	89	420.54	1.5
90	423.06	1.43	90	423.84	1.41
91	426.41	1.29	91	427.33	1.25
92	429.91	1.11	92	430.77	1.1
93	433.45	0.88	93	434.17	0.91
94	436.64	0.64	94	437.52	0.6
95	440.26	0.39	95	441.06	0.33
96	443.71	0.2	96	444.37	0.18
97	447.18	0.04	97	447.88	0

Appendix M

Distances and elevations along SCSI-13.
Measurements are relative to the first geophone at the south end of the line.

Geophone No.	Geo. Dist. (m)	Geo. Elev. (m)	Shot Point No.	Shot Dist (m)	Shot Elev. (m)
1	0.42	11.63	1	0	11.69
2	4.72	11.66	2	4.39	11.7
3	9.16	11.71	3	8.76	11.69
4	13.99	11.54	4	13.24	11.62
5	17.36	11.54			
6	20.24	11.5	6	19.45	11.52
7	23.57	11.51	7	23.04	11.52
8	28.01	11.49	8	27.62	11.52
9	32.52	11.41	9	32.2	11.46
10	37.55	11.31	10	36.92	11.44
11	41.84	11.26	11	41.18	11.38
12	45.93	11.24	12	45.37	11.35
13	49.63	11.3	13	49.09	11.36
14	53.77	11.3	14	53.12	11.43
15	57.21	11.32	15	56.63	11.35
16	61.2	11.31	16	60.6	11.38
17	64.79	11.37	17	64.2	11.42
18	68.63	11.35	18	68.11	11.4
19	72.43	11.33	19	71.83	11.36
20	76.34	11.32	20	75.74	11.35
21	80.17	11.33	21	79.58	11.38
22	84.49	11.38	22	84	11.39
23	88.66	11.37	23	88.19	11.35
24	92.6	11.37	24	92.3	11.35
25	97.04	11.28	25	96.64	11.35
26	101.35	11.17	26	101.1	11.18
27	105.62	11.03	27	105.33	10.95
28	110.25	10.75	28	110.03	10.72
29	114.64	10.46	29	114.25	10.44
30	119.41	10.02	30	119.06	10.02
31	123.79	9.6	31	123.44	9.58
32	127.86	9.22	32	127.68	9.2
33	132.56	8.9	33	132.01	8.9
34	136.66	8.75	34	136.39	8.7
35	140.99	8.53	35	140.43	8.61
36	145.16	8.43	36	144.78	8.46
37	150.01	8.27	37	149.51	8.31
38	154.19	8.24	38	153.66	8.3
39	158.73	8.27	39	158.3	8.29
40	162.49	8.34	40	162.14	8.4
41	167.18	8.53	41	166.71	8.52
42	171.41	8.54	42	171.06	8.53
43	175.96	8.41	43	175.61	8.41
44	180.64	8.38	44	180.36	8.39
45	185.08	8.46	45	184.78	8.47
46	189.99	8.57	46	189.44	8.52
47	194.55	8.42	47	194.2	8.46
48	199.16	8.44	48	198.74	8.44
49	203.63	8.48	49	203.38	8.48
50	207.85	8.7	50	207.88	8.67
51	212.42	9.3	51	212.26	9.22
52	217.18	9.69	52	216.86	9.58
53	222.06	10.01	53	221.66	9.92
54	226.62	10.34	54	226.33	10.36
55	231.42	10.68	55	231.04	10.77
56	236.1	11.03	56	235.86	11.09

57	241.09	11.39	57	240.89	11.42
58	245.7	11.9	58	245.54	11.87
59	250.54	12.28	59	250.33	12.36
60	255.15	12.72	60	255.09	12.89
61	260.3	13.43	61	259.99	13.51
62	264.82	13.8	62	264.88	13.79
63	269.79	13.74	63	269.89	13.7
64	275.09	13.44	64	274.81	13.43
65	280.27	12.29	65	280.08	12.6
66	285.53	11.63	66	285.18	11.85
67	290.28	11.14	67	289.99	11.4
68	295.29	11.01	68	295.05	11.09
69	300.18	10.92	69	299.9	11.07
70	305.13	11.04	70	305.01	11.03
71	310.01	10.9	71	309.53	10.9
72	314.82	10.44	72	314.69	10.55
73	319.74	10.47			
74	324.17	10.25	74	324.51	10.32
75	328.67	10.23	75	329.02	10.08
76	333.53	10.02	76	333.79	9.91
77	338.81	9.78	77	338.82	9.81
78	343.76	9.68	78	343.76	9.68
79	348.74	9.69	79	348.63	9.7
80	354.04	9.55	80	353.83	9.72
81	358.84	9.9	81	358.55	9.81
82	363.79	10	82	363.69	9.91
83	368.73	10.06	83	368.56	9.84
84	373.16	10.25	84	373.5	10.01
85	378.35	10.09	85	378.54	9.96
86	382.9	10.1	86	383.36	10.03
87	387.34	10.09	87	387.82	10.03
88	391.99	10.1	88	392.43	10.05
89	396.57	10.07	89	396.88	10.02
90	401.2	9.99	90	401.39	10.02
91	405.65	9.93	91	405.96	9.94
92	410.69	9.99	92	410.85	9.92
93	415.62	9.93	93	415.67	9.88
94	420.44	9.71	94	420.8	9.69
95	425.59	9.51	95	425.77	9.52
96	430.11	9.68	96	430.3	9.61
97	434.81	9.63	97	434.96	9.59
98	439.07	9.48	98	439.41	9.48
99	443.55	9.57	99	444.31	9.44
100	448	9.46	100	448.53	9.41
101	452.33	9.47	101	452.74	9.48
102	457.23	9.44	102	457.63	9.51
103	462.14	9.53	103	462.37	9.56
104	466.9	9.57	104	467.17	9.62
105	471.52	9.49	105	471.71	9.56
106	475.79	9.48	106	476.34	9.55
107	480.22	9.44	107	480.39	9.5
108	484.29	9.44			
109	488.33	9.27	109	488.84	9.27
110	492.89	9.23	110	493.3	9.24
111	497.42	9.12	111	497.58	9.18
112	501.82	9.12	112	502.19	9.15
113	506.02	9.09	113	506.45	9.08
114	510.69	9.11	114	510.8	9.04
115	515.16	9.06	115	515.2	9.01
116	519.38	8.99	116	519.81	8.99
117	524.02	8.9	117	524.15	8.96
118	528.71	8.92	118	528.97	8.93
119	533.01	8.9	119	533.29	8.94
120	537.79	8.95	120	538.26	8.86
121	542.29	8.91	121	542.51	8.87
122	546.84	8.88	122	547.14	8.91
123	551.24	8.89	123	551.69	8.86
124	555.65	8.97	124	555.87	8.9
125	559.85	8.8	125	560.2	8.85
126	564.22	8.79	126	564.71	8.81
127	568.71	8.74	127	569.08	8.81
128	573.33	8.74	128	573.66	8.75
129	577.9	8.91	129	578.15	8.74
130	582.81	8.86	130	582.96	8.74
131	587.51	8.66	131	587.75	8.67
132	592.78	8.75	132	592.85	8.68
133	597.63	8.78	133	597.73	8.66
134	602.66	8.63	134	602.77	8.64
135	607.74	8.6	135	607.75	8.53
136	612.87	8.55	136	612.81	8.51
137	617.73	8.5	137	617.64	8.51
138	622.41	8.52			

139	627.51	8.7	139	627.42	8.6
140	632.24	8.64			
141	637.36	8.27	141	637.34	8.35
142	642.34	8.28	142	642.14	8.37
143	647.21	8.24	143	647.1	8.32
144	652.16	8.25	144	652.48	8.33
145	656.31	8.23	145	657.08	8.38
146	661.17	8.36	146	661.17	8.4
147	665.87	8.35	147	665.94	8.31
148	670.68	8.34	148	670.79	8.31
149	675.83	8.32	149	675.9	8.3
150	680.97	8.17	150	680.98	8.31
151	685.61	7.89			
152	690.48	7.76	152	690.73	8.34
153	695.31	8.18	153	695.61	8.42
154	700.39	8.31	154	700.49	8.35
155	705.26	8.25	155	705.45	8.3
156	710.42	8.17	156	710.52	8.45
157	715.06	8.28	157	715.25	8.52
158	720.34	8.17	158	720.36	8.51
159	725.31	8.33	159	725.42	8.48
160	730.3	8.32	160	730.5	8.46
161	735.32	8.41	161	735.49	8.43
162	740.22	8.45	162	740.36	8.49
163	745.11	8.32	163	745.32	8.5
164	750.08	8.56	164	750.24	8.61
165	754.83	8.48	165	755.08	8.48
166	759.88	8.57	166	760.09	8.62
167	764.65	8.63	167	764.84	8.65
168	769.57	8.61	168	769.68	8.7
169	774.8	8.28	169	774.82	8.52
170	779.64	8.38	170	779.75	8.55
171	784.04	8.38	171	784.45	8.51
172	789.18	8.32	172	789.49	8.46
173	793.96	8.32	173	794.25	8.41
174	798.57	8.22	174	799.01	8.41
175	803.86	8.18	175	803.97	8.38
176	808.69	8.25	176	808.84	8.31
177	813.43	8.22	177	813.61	8.29
178	818.47	8.24	178	818.55	8.3
179	823.13	8.34	179	823.41	8.32
180	827.82	8.32	180	828.17	8.32
181	832.59	8.36	181	833.06	8.31
182	837.73	8.34	182	837.82	8.3
183	842.21	8.35	183	842.61	8.31
184	846.88	8.34	184	847.22	8.33
185	851.59	8.36	185	852.02	8.33
186	856.32	8.37	186	856.67	8.28
187	861.14	8.35	187	861.56	8.35
188	865.85	8.33	188	866.17	8.32
189	870.64	8.21	189	870.99	8.31
190	875.38	8.3	190	875.5	8.36
191	879.99	8.34	191	880.49	8.41
192	885	8.42	192	885.07	8.44
193	889.71	8.39	193	889.92	8.36
194	894.18	8.39	194	894.56	8.41
195	898.96	8.45	195	899.31	8.42
196	903.7	8.43	196	904.02	8.46
197	908.67	8.54	197	908.75	8.52
198	913.36	8.56	198	913.62	8.5
199	917.72	8.56	199	918	8.51
200	922.22	8.47	200	922.63	8.5
201	926.7	8.45	201	927.03	8.53
202	931.41	8.42	202	931.83	8.49
203	935.93	8.39	203	936.5	8.45
204	940.6	8.33	204	940.93	8.35
205	945.1	8.07	205	945.63	8.2
206	949.67	7.89	206	950.29	8.01
207	954.85	8.02	207	955.12	7.95
208	959.81	8.02			
209	964.77	8.01	209	965.2	7.89
210	969.72	7.75	210	969.87	7.75
211	974.65	7.68	211	974.8	7.62
212	979.54	7.65			
213	984.77	7.63	213	984.74	7.56
214	989.59	7.66	214	989.72	7.56
215	994.15	7.58			
216	998.84	7.51	216	999.2	7.51
217	1004.05	7.43	217	1004.06	7.41
218	1008.32	7.26	218	1008.74	7.26
219	1013.23	7.15	219	1013.55	7.16
220	1017.66	6.87	220	1018.27	6.86

221	1022.36	6.51	221	1022.75	6.55
222	1026.85	6.09	222	1027.23	6.14
223	1031.56	5.7	223	1031.72	5.76
224	1035.89	5.47	224	1036.36	5.49
225	1040.32	5.17	225	1040.83	5.17
226	1044.76	5.1	226	1045.13	4.99
227	1049.04	5.09	227	1049.53	4.73
228	1053.31	4.69	228	1053.73	4.57
229	1057.81	4.45	229	1058.13	4.41
230	1062.26	4.35	230	1062.63	4.3
231	1066.49	4.27	231	1066.83	4.26
232	1070.78	4.21	232	1071.2	4.19
233	1075.35	4.2	233	1075.67	4.18
234	1079.95	4.19	234	1080.21	4.16
235	1084.47	4.17	235	1084.92	4.15
236	1089.39	4.21	236	1089.67	4.14
237	1094.16	4.17	237	1094.33	4.12
238	1099.08	4.14	238	1099.25	4.07
239	1103.91	4.13			
240	1108.84	4.12	240	1108.93	4.09
241	1113.45	4.11	241	1113.65	4.09
242	1118.54	4.13	242	1118.67	4.12
243	1123.38	4.16	243	1123.55	4.12
244	1128.11	4.23	244	1128.36	4.17
245	1132.62	4.17			
246	1137.22	4.14	246	1137.58	4.11
247	1141.85	4.11	247	1142.12	4.07
248	1145.99	4.09	248	1146.38	4.07
249	1150.59	4.09	249	1151.08	4.05
250	1155.12	4.06	250	1155.33	4.04
251	1159.44	4.05	251	1159.82	4
252	1163.71	4	252	1164.18	3.98
253	1168.66	3.97	253	1168.9	3.96
254	1172.96	3.83	254	1173.46	3.89
255	1177.71	3.83	255	1178.01	3.86
256	1182.45	3.85	256	1182.72	3.84
257	1187.01	3.85	257	1187.4	3.85
258	1192.02	3.81	258	1192.3	3.81
259	1196.62	3.59	259	1196.91	3.76
260	1201.53	3.73	260	1201.98	3.76
261	1206.58	3.73	261	1206.78	3.73
262	1211.7	3.7	262	1211.91	3.72
263	1216.44	3.69	263	1216.64	3.7
264	1221.67	3.7	264	1221.89	3.64
265	1226.4	3.63	265	1226.66	3.62
266	1231.48	3.62			
267	1236.49	3.61	267	1236.53	3.59
268	1241.39	3.56	268	1241.45	3.56
269	1246.41	3.55	269	1246.41	3.54
270	1251.4	3.6	270	1251.45	3.56
271	1256.34	3.57	271	1256.39	3.55
272	1261.39	3.56	272	1261.43	3.55
273	1266.43	3.53	273	1266.42	3.52
274	1271.31	3.54	274	1271.38	3.52
275	1276.39	3.51	275	1276.32	3.49
276	1281.61	3.48	276	1281.36	3.48
277	1286.75	3.33	277	1286.46	3.45
278	1291.68	3.46	278	1291.44	3.45
279	1296.73	3.54	279	1296.59	3.54
280	1301.59	3.58	280	1301.45	3.58
281	1306.3	3.55	281	1306.18	3.58
282	1311.15	3.59	282	1311.05	3.58
283	1316.28	3.62	283	1315.87	3.62
284	1320.75	3.52	284	1320.5	3.53
285	1325.77	3.55	285	1325.43	3.57
286	1330.37	3.58	286	1330.05	3.53
287	1335.12	3.55	287	1334.91	3.56
288	1340.34	3.51	288	1340.05	3.53
289	1344.91	3.49	289	1344.57	3.52
290	1349.65	3.44	290	1349.31	3.48
291	1354.4	3.45			
292	1359.04	3.48	292	1358.64	3.49
293	1363.74	3.48	293	1363.32	3.48
294	1368.43	3.48	294	1368.04	3.46
295	1373.55	3.46	295	1372.75	3.49
296	1377.92	3.47	296	1377.51	3.47
297	1382.65	3.46	297	1382.51	3.46
298	1386.97	3.42	298	1386.8	3.41
299	1391.79	3.41	299	1391.59	3.4
300	1396.82	3.38	300	1396.63	3.35
301	1400.86	3.39			
302	1404.64	3.3	302	1404.47	3.29

303	1409.49	3.27	303	1409.28	3.24
304	1414.76	3.28	304	1414.61	3.28
305	1419.49	3.35	305	1419.17	3.32
306	1424.01	3.29	306	1423.8	3.29
307	1428.95	3.27	307	1428.71	3.3
308	1433.65	3.2			
309	1437.94	3.11	309	1437.75	3.23
310	1442.78	2.84	310	1442.22	3.21
311	1447.32	2.88	311	1447.23	3.08
312	1452.42	3.11	312	1452.08	3.15
313	1457.36	3.09	313	1457.07	3.16
314	1462.31	3.08	314	1462.16	3.14
315	1467.11	3.02	315	1466.73	3.13
316	1471.79	3.13	316	1471.49	3.1
317	1476.95	3.01			
318	1481.26	2.98	318	1480.89	3.02
319	1486.11	2.93	319	1485.8	3.06
320	1490.81	2.94	320	1490.57	3.07
321	1495.49	3.01			
322	1500.14	3.08	322	1499.93	3.06
323	1503.8	3.13	323	1503.49	3.14
324	1508.52	3.19	324	1508.06	3.09
325	1512.98	3.2	325	1512.63	3.14
326	1517.93	3.24	326	1517.65	3.19
327	1521.79	3.24	327	1521.62	3.19
328	1526.85	3.28	328	1526.7	3.24
329	1531.46	3.26	329	1531.25	3.24
330	1536.18	3.31	330	1535.81	3.26
331	1540.87	3.4	331	1540.58	3.17
332	1545.49	3.29	332	1545.22	3.11
333	1550.36	3.26	333	1550.04	3.08
334	1554.88	3.19	334	1554.64	2.95
335	1559.72	3.16	335	1559.25	2.92
336	1564.3	3.16	336	1564.07	2.93
337	1569.11	3.18	337	1568.7	2.94
338	1573.73	3.13	338	1573.46	2.91
339	1578.45	3.21	339	1577.97	3
340	1582.96	3.14	340	1582.49	2.93
341	1587.55	3.17	341	1587.17	2.97
342	1592.04	3.17	342	1591.56	3.01
343	1596.28	3.08	343	1595.79	2.89
344	1600.29	3.07	344	1599.8	2.88
345	1604.61	3.01	345	1604.08	2.77
346	1609.13	3.01	346	1608.47	2.77
347	1613.45	3.02	347	1612.98	2.82
348	1617.25	3.01	348	1616.72	2.78
349	1621.24	2.98	349	1620.63	2.78
350	1625.34	2.99	350	1624.63	2.73
351	1629.3	2.88	351	1628.74	2.72
352	1633.5	2.97			
353	1637.52	2.96	353	1636.92	2.68
354	1641.61	2.93	354	1641.07	2.7
355	1645.63	2.97	355	1645.03	2.71
356	1649.68	2.98	356	1649.28	2.78
357	1653.8	3.08	357	1653.4	2.93
358	1658.94	3.04			
359	1664.43	3.02	359	1663.86	3.01
360	1668.34	3.02	360	1667.88	3.05
361	1672.36	2.99	361	1671.77	3.08
362	1676.45	2.9	362	1675.96	3.1
363	1680.17	2.85	363	1679.61	3.04
364	1684.04	2.48	364	1683.58	2.97
365	1688.65	2.89	365	1688.06	2.91
366	1692.48	2.98	366	1691.94	3
367	1696.64	2.96	367	1696.28	3.01
368	1700.43	2.92	368	1699.84	3.01
369	1704.75	2.82	369	1703.97	3.04
370	1708.66	2.87	370	1707.93	3.01
371	1712.68	2.82	371	1712.16	3.03
372	1716.97	2.81	372	1716.26	2.99
373	1720.71	2.77	373	1720.2	3.02
374	1724.87	2.67	374	1724.06	2.92
375	1728.64	2.76	375	1728.22	3.01
376	1732.92	2.74	376	1732.22	2.96
377	1736.87	2.59	377	1736.42	3
378	1740.82	2.69	378	1740.4	2.91
379	1744.72	2.77	379	1744.16	2.95
380	1748.87	2.59	380	1748.38	2.85
381	1752.85	2.59	381	1752.19	2.85
382	1756.95	2.42	382	1756.28	2.77
383	1760.85	2.52	383	1760.31	2.71
384	1764.99	2.65	384	1764.51	2.82

385	1769.04	2.82	385	1768.11	2.92
386	1773.09	2.87	386	1772.43	2.88
387	1777.19	2.9	387	1776.76	2.85
388	1781.2	2.92	388	1780.37	2.88
389	1785.52	2.92	389	1785.05	2.89
390	1789.51	2.91	390	1788.99	2.88
391	1793.66	2.87	391	1793.02	2.79
392	1797.77	2.9	392	1797.08	2.84
393	1801.86	2.86	393	1801.33	2.81
394	1806.12	2.9	394	1805.67	2.86
395	1810.52	2.93	395	1809.89	2.85
396	1814.44	2.89	396	1813.94	2.84
397	1818.73	2.87	397	1818.22	2.82
398	1822.59	2.85	398	1822.04	2.8
399	1826.61	2.82	399	1826.04	2.77
400	1830.57	2.76	400	1830.05	2.7
401	1834.47	2.53	401	1833.87	2.45
402	1838.28	2.3	402	1837.85	2.24
403	1842.34	2.03	403	1841.7	1.98
404	1846.45	1.71	404	1845.79	1.69
405	1850.18	1.47	405	1849.62	1.45
406	1854.28	1.22	406	1853.58	1.2
407	1858.24	1.03	407	1857.69	1.06
408	1862.38	0.92	408	1861.82	0.93
409	1866.37	0.9	409	1865.91	0.88
410	1870.56	0.84	410	1869.99	0.82
411	1874.48	0.8	411	1873.78	0.81
412	1878.33	0.76	412	1877.64	0.75
413	1882.07	0.76	413	1881.72	0.74
414	1886.39	0.48	414	1885.99	0.63
415	1890.75	0.24	415	1890.18	0.58
416	1894.65	0.69	416	1894.14	0.72
417	1898.86	0.7	417	1898.26	0.72
418	1902.7	0.66	418	1902.19	0.68
419	1906.57	0.67	419	1906.11	0.67
420	1910.68	0.66	420	1910.22	0.66
421	1914.65	0.64	421	1914.22	0.64
422	1918.68	0.67	422	1918.24	0.64
423	1922.59	0.56	423	1922.13	0.58
424	1926.82	0.51	424	1926.33	0.54
425	1930.82	0.25	425	1930.32	0.48
426	1934.76	0.51			
427	1938.6	0.55	427	1938.12	0.54
428	1942.56	0.57	428	1942.24	0.54
429	1946.63	0.56	429	1946.23	0.54
430	1950.67	0.54	430	1950.03	0.6
431	1954.73	0.6	431	1954.23	0.59
432	1958.65	0.51	432	1958.26	0.57
433	1962.29	0.64	433	1962.06	0.58
434	1966.53	0.57	434	1966.07	0.52
435	1970.66	0.59	435	1970.35	0.5
436	1974.89	0.53	436	1974.32	0.47
437	1978.6	0.47	437	1978.18	0.45
438	1982.8	0.42	438	1982.47	0.43
439	1986.77	0.45	439	1986.32	0.44
440	1990.52	0.5	440	1990.18	0.46
441	1995.25	0.43	441	1994.35	0.41
442	1998.84	0.44	442	1998.45	0.36
443	2003	0.39	443	2002.54	0.36
444	2007.17	0.38	444	2006.71	0.32
445	2011.05	0.38	445	2010.77	0.33
446	2015.06	0.35			
447	2019.18	0.26	447	2018.74	0.33
448	2022.98	0	448	2022.76	0.17
449	2027.98	0			
450	2032.98	0			
451	2037.98	0			
452	2042.98	0			

Appendix N

Distances and elevations along SCSI-14.
Measurements are relative to the first geophone at the south end of the line.

Geophone No.	Geo. Dist. (m)	Geo. Elev. (m)	Shot Point No.	Shot Dist (m)	Shot Elev. (m)
1	0.16	1.2	1	0	1.43
2	4.9	1.36	2	4.96	1.46
3	9.73	1.3	3	9.79	1.35
4	14.92	1.01	4	14.77	1.35
5	19.67	1.07	5	19.69	1.41
6	24.64	0.98	6	24.78	1.33
7	29.73	1.03	7	29.97	1.38
8	34.54	1.32	8	34.73	1.32

9	39.6	1.09	9	39.8	1.31
10	44.3	1.18	10	44.57	1.31
11	49.75	1.1	11	49.71	1.34
12	54.94	1.03	12	54.66	1.29
13	59.8	1.08	13	59.62	1.35
14	64.77	1.05	14	64.64	1.23
15	69.44	0.89	15	69.51	1.12
16	74.59	0.7	16	74.64	1.01
17	79.74	0.93	17	79.6	1.1
18	84.55	0.93	18	84.54	1.11
19	89.64	1.02	19	89.77	1.17
20	94.82	1.01	20	94.59	1.21
21	99.61	1.11	21	99.8	1.11
22	104.38	1.03	22	104.44	1.28
23	109.48	1.15	23	109.42	1.31
24	114.46	1.18	24	114.6	1.38
25	119.47	1.2	25	119.53	1.43
26	124.48	1.2	26	124.47	1.45
27	129.46	1.03	27	129.5	1.45
28	134.57	1.15	28	134.52	1.35
29	139.39	1.15	29	139.42	1.34
30	144.59	0.92	30	144.67	1.32
31	149.41	0.92	31	149.48	1.18
32	154.45	0.82	32	154.43	1.28
33	159.48	1.12	33	159.44	1.32
34	164.38	1.07	34	164.49	1.33
35	169.26	1.17	35	169.33	1.38
36	174.28	1.16	36	174.35	1.42
37	179.35	1.28	37	179.16	1.43
38	183.66	1.44			
39	189.53	1.34	39	189.21	1.39
40	194.46	1.35	40	194.26	1.36
41	199.26	1.18	41	199.28	1.3
42	204.27	1.11	42	204.3	1.29
43	209.17	1.06	43	209.28	1.3
44	214	1.3	44	214.19	1.3
45	219.19	1.31	45	219.37	1.31
46	224.36	1.3			
47	229.22	1.19	47	229.24	1.29
48	234.17	1.11	48	234.16	1.28
49	239.08	1.26	49	239.15	1.28
50	244.13	1.1	50	243.98	1.29
51	249.18	0.97	51	249.25	1.19
52	253.84	0.86	52	253.85	1.14
53	259.13	0.79	53	259.35	1.02
54	264.13	0.71	54	264.07	1.01
55	269.12	0.83	55	269.29	1.03
56	274.23	0.71	56	274.14	1.03
57	279.1	0.63	57	278.97	1.09
58	284.39	0.89	58	284.07	1.13
59	289.42	0.73	59	289.24	1.09
60	294.08	0.92	60	294.06	1.18
61	298.98	0.92	61	299.03	1.18
62	304.02	1.09	62	303.96	1.2
63	309.04	1.1	63	309.04	1.17
64	313.95	1.09	64	313.93	1.19
65	319.23	1.12	65	318.94	1.18
66	324.03	1.21	66	323.92	1.2
67	329.05	1.15	67	328.85	1.2
68	334.04	1.19	68	334.02	1.26
69	338.92	1.24	69	338.86	1.25
70	343.9	1.27	70	343.92	1.28
71	348.99	1.24	71	348.84	1.24
72	353.77	1.07	72	353.85	1.25
73	358.77	1.02	73	358.84	1.26
74	363.95	0.97	74	363.86	1.18
75	369.11	0.56	75	368.96	1
76	374.03	0.86	76	374.08	0.94
77	378.91	0.82	77	378.86	0.94
78	383.88	0.6	78	383.88	0.82
79	388.81	0.72	79	388.74	0.93
80	393.82	0.83	80	393.88	1.08
81	398.93	1.01	81	398.8	1.19
82	404.06	1.13	82	403.83	1.23
83	408.9	1.16	83	408.94	1.19
84	413.76	1.13	84	413.7	1.2
85	418.56	1.16	85	418.75	1.16
86	423.45	1.12	86	423.64	1.12
87	428.59	1.22	87	428.78	1.22
88	434.02	1.08	88	433.69	1.13
89	438.8	1.04	89	438.8	1.13
90	443.58	0.77	90	443.7	1.06

91	448.67	0.62	91	448.75	0.98
92	453.8	0.4	92	453.58	0.87
93	458.74	0.41	93	458.69	0.76
94	463.71	0.46	94	463.87	0.81
95	468.82	0.47	95	468.79	0.87
96	474.03	0.59	96	473.9	0.95
97	478.74	0.75	97	478.73	1.11
98	483.57	0.93	98	483.52	1.12
99	488.76	1.01	99	488.66	1.09
100	493.54	1.05	100	493.65	1.03
101	498.53	0.97	101	498.61	1.05
102	503.45	1.07	102	503.63	1.07
103	508.29	1.09	103	508.47	1.09
104	513.55	0.95	104	513.51	1.06
105	518.43	1.04	105	518.59	1.06
106	523.35	1	106	523.51	0.97
107	528.48	0.73	107	528.45	0.84
108	533.48	0.69	108	533.58	0.8
109	538.52	0.39	109	538.55	0.65
110	543.39	0.35	110	543.48	0.7
111	548.4	0.31	111	548.33	0.72
112	553.45	0.53	112	553.58	0.82
113	558.58	0.44	113	558.5	0.89
114	563.66	0.41	114	563.53	0.92
115	568.62	0.73	115	568.5	0.94
116	573.31	0.81	116	573.37	0.95
117	578.63	0.71	117	578.49	1.01
118	583.46	0.74	118	583.5	0.99
119	588.39	0.63	119	588.54	0.88
120	593.46	0.59	120	593.29	0.95
121	598.44	0.56	121	598.35	0.92
122	603.24	0.73	122	603.25	0.92
123	608.31	0.73	123	608.28	0.89
124	613.4	0.69	124	613.48	0.99
125	618.08	0.8	125	618.24	1.08
126	622.98	1.04	126	623	1.13
127	627.86	0.84	127	628.04	1.12
128	633.15	0.95	128	633.04	1.09
129	637.64	0.92	129	637.97	1.19
130	642.73	1	130	643.05	1.19
131	647.96	0.93	131	648	1.15
132	652.75	1.04	132	652.87	1.16
133	657.96	0.91	133	657.87	1.08
134	662.7	0.9	134	662.76	1.03
135	667.73	0.71	135	667.88	0.94
136	672.57	0.74	136	672.64	0.87
137	677.81	0.91	137	677.2	0.86
138	682.25	0.74	138	682.39	0.31
139	686.9	0.66	139	687.28	0.79
140	691.8	0.6	140	692.13	0.69
141	697.11	0.55	141	697.03	0.58
142	701.64	0.54	142	701.77	0.56
143	706.71	0.59	143	706.76	0.54
144	711.24	0.54	144	711.5	0.55
145	716.06	0.44	145	716.53	0.59
146	721.01	0.45	146	721.22	0.55
147	725.89	0.39	147	726.11	0.5
148	730.79	0.27	148	730.96	0.39
149	735.85	0.24	149	735.93	0.33
150	740.5	0.1	150	740.72	0.44
151	745.51	0.33	151	745.74	0.44
152	750.26	0.46	152	750.38	0.53
153	755	0.33	153	755.19	0.5
154	759.97	0.13	154	760.24	0.34
155	764.95	0.28	155	765.13	0.4
156	769.97	0.39	156	769.97	0.47
157	774.54	0.06	157	774.7	0.4
158	779.56	0.35			
159	783.87	0	159	784.44	0.33
160	789.13	0.36	160	789.11	0.49
161	794.11	0.56	161	794.03	0.54

Appendix 0

UTM Coordinates of the Beginning and Ending of the Seismic Profiles

Profile	UTM Coordinate–Northing (Start)	UTM Coordinate Easting (Start)	Elevation –m (start)	UTM Coordinate Northing (End)	UTM Coordinate–Easting (End)	Elevation–m (End)
SCSI–1						
SCSI–2	4118389.92	589669.16	140.42	4118874.07	589785.11	129.43
SCSI–3	4118864.73	589781.45	129.59	4119425.33	589788.68	120.29
SCSI–4	4119415.88	589784.81	120.59	4119603.22	589930.78	118.98

SCSI-5	4119606.06	589928.35	118.77	4120105.00	590576.81	105.33
SCSI-6	4120133.00	590592.52	106.68	4120287.28	590776.10	104.04
SCSI-7	4120276.13	590577.23	107.03	4120669.40	590952.54	101.76
SCSI-8	4120645.38	590914.74	100.08	4120930.39	591098.94	101.32
SCSI-9	4121124.20	591034.74	97.72	4122485.32	591750.65	91.79
SCSI-10	4122449.00	591728.00	94.48	4122647.18	591956.33	96.88
SCSI-11	4122775.75	591793.68	87.13	4123359.97	591863.33	82.39
SCSI-12	4123361.59	591876.04	83.08	4123744.30	592100.93	80.40
SCSI-13	4123773.35	592052.05	80.51	4125491.68	593154.68	68.88
SCSI-14	4125757.89	593263.33	60.02	4126518.98	593490.04	59.38